EXPERIMENTAL LASER ATTENUATION IN A SNOW ENVIRONMENT

John T. Miller
ARO, Inc., a Sverdrup Corporation Company

VON KÁRMÁN GAS DYNAMICS FACILITY
ARNOLD ENGINEERING DEVELOPMENT CENTER
AIR FORCE SYSTEMS COMMAND
ARNOLD AIR FORCE STATION, TENNESSEE 37389

March 1978

Final Report for Period January 24 — September 4, 1977

Approved for public release; distribution unlimited.

Prepared for

ARNOLD ENGINEERING DEVELOPMENT CENTER/DOTR
ARNOLD AIR FORCE STATION, TENNESSEE 37389

NOTICES
When U. S. Government drawings, specifications, or other data are used for any purpose other than a definitely related Government procurement operation, the Government thereby incurs no responsibility nor any obligation whatsoever, and the fact that the Government may have formulated, furnished, or in any way supplied the said drawings, specifications, or other data, is not to be regarded by implication or otherwise, or in any manner licensing the holder or any other person or corporation, or conveying any rights or permission to manufacture, use, or sell any patented invention that may in any way be related thereto.
Qualified users may obtain copies of this report from the Defense Documentation Center.
References to named commerical products in this report are not to be considered in any sense as an indorsement of the product by the United States Air Force or the Government.

This report has been reviewed by the Information Office (OI) and is releasable to the National Technical Information Service (NTIS). At NTIS, it will be available to the general public, including foreign nations.

APPROVAL STATEMENT

This report has been reviewed and approved.

Stephen L. Lamkin

STEPHEN L. LAMKIN, Captain, USAF
Project Manager, Research Division
Directorate of Test Engineering

Approved for publication:

FOR THE COMMANDER

Marion L. Laster

MARION L. LASTER
Director of Test Engineering
Deputy for Operations

REPORT DOCUMENTATION PAGE		READ INSTRUCTIONS BEFORE COMPLETING FORM
1 REPORT NUMBER AEDC-TR-77-99	2 GOVT ACCESSION NO.	3. RECIPIENT'S CATALOG NUMBER
4 TITLE (and Subtitle) EXPERIMENTAL LASER ATTENUATION IN A SNOW ENVIRONMENT		5 TYPE OF REPORT & PERIOD COVERED Final Report - January 24 to September 4, 1977 6. PERFORMING ORG. REPORT NUMBER
7. AUTHOR(s) John T. Miller - ARO, Inc.		8. CONTRACT OR GRANT NUMBER(s)
9 PERFORMING ORGANIZATION NAME AND ADDRESS Arnold Engineering Development Center/DOT Air Force Systems Command Arnold Air Force Station, Tennessee 37389		10. PROGRAM ELEMENT, PROJECT, TASK AREA & WORK UNIT NUMBERS Program Element 65807F
11 CONTROLLING OFFICE NAME AND ADDRESS Arnold Engineering Development Center/DOS Arnold Air Force Station Tennessee 37389		12. REPORT DATE March 1978 13. NUMBER OF PAGES 84
14 MONITORING AGENCY NAME & ADDRESS(if different from Controlling Office)		15. SECURITY CLASS. (of this report) UNCLASSIFIED 15a. DECLASSIFICATION/DOWNGRADING SCHEDULE N/A

16 DISTRIBUTION STATEMENT (of this Report)

Approved for public release; distribution unlimited.

17 DISTRIBUTION STATEMENT (of the abstract entered in Block 20, if different from Report)

18 SUPPLEMENTARY NOTES

Available in DDC

19 KEY WORDS (Continue on reverse side if necessary and identify by block number)

lasers
attenuation
snowfields
predictions
mathematical analysis
experimental data

20 ABSTRACT (Continue on reverse side if necessary and identify by block number)

Laser transmission through a snowfield has been measured in a laboratory experiment. Simultaneous measurements of the attenuation of a 0.6328- and a 10.6-μ wavelength laser beam by a common snowfield are reported. The results are favorably compared with a prediction of an analytic model which treats the snowflakes as spheres. The analytic model is then restructured and applied to predict the attenuation which would be obtained in a natural snowfield.

DD FORM 1 JAN 73 1473 EDITION OF 1 NOV 65 IS OBSOLETE

PREFACE

The work reported herein was conducted by the Arnold Engineering Development Center (AEDC), Air Force Systems Command (AFSC), at the request of the Air Force Weapons Laboratory (AFWL), under Program Element 65807F. The results were obtained by ARO, Inc., AEDC Division (a Sverdrup Corporation Company), operating contractor for the AEDC, AFSC, Arnold Air Force Station, Tennessee, under ARO Project No. V34S-COA. The manuscript was submitted for publication on September 30, 1977.

CONTENTS

ILLUSTRATIONS

Page

TABLES

APPENDIXES

1.0 INTRODUCTION

In view of the increasing role of lasers for current and potential military applications, information on the propagation characteristics of a laser beam through various environments is essential. Although a wide variety of phenomenon affects the propagation of laser beams, only the combined influence of absorption and scattering have been measured in the current experiments. The power levels were sufficiently low that no thermal blooming or plasma generation was encountered. The test environment was limited to snow crystals falling through air, and measurements were made at wavelengths of both 10.6 and 0.6328 μ for direct comparisons.

Experimental measurements of laser propagation through hard-to-define mediums such as snow are especially valuable, in view of the analytic difficulties encountered in modeling a snow environment. The experimental measurements can provide check points for analytical models and improve the estimation of the field performance of laser devices.

2.0 EXPERIMENTAL DATA

2.1 EXPERIMENTAL FACILITY

The experimental arrangement is shown in Fig. 1. The equipment was installed in a 60-ft-long, 8-ft-diam, steel tank which can be closed and evacuated to any desired pressure between an atmosphere and a few mm Hg. For the present tests, the pressure was atmospheric.

Both a CO_2 laser HeNe laser were used concurrently in the experiment, so that simultaneous attenuation measurements could be made. The lasers were installed at one end of the tank, with the CO_2 beam slightly above the HeNe laser beam. At the other end of the tank, the detectors were installed with the CO_2 detector below the HeNe detector. This arrangement made the two laser beams essentially coincident through the intervening snowfield, so that attenuation measurements for the two beams are directly comparable.

The CO_2 laser was a continuous three-watt device. The initial beam was expanded to a 1.7-in. diameter, using a germanium lens, and then focused onto the detector at the far end of the tank. This focusing was accomplished with a 6-in.-diam, 48-in. focal length spherical concave mirror. The beam size at the detector was approximately 1/4 in. in diameter. The measured power delivered to the detector was 0.75 watt.

The first part of the test was conducted using a detector manufactured by Molectron Corporation to measure the CO_2 beam power. This detector required the use of a chopper to modulate the laser beam, and additional electronics to electronically remove the chopping perturbations from the output signal.

During the latter part of the test, a detector manufactured by the Santa Barbara Research Center was used which did not require the use of a chopper and the associated electronics. This detector required liquid-nitrogen cooling. The lasers and detectors used are listed in Table 1.

The HeNe laser used was a 15-mw continuous device. The beam was expanded to 1.5 in. in diameter and then focused onto the detector at the far end of the tank. The expanding and focusing were accomplished using a commercial beam expander which attached directly to the laser.

At the snowfield, both beams were approximately 1 in. diameter and coincident.

The snowfield generator used is 28 in. long, 12 in. high, and is mounted 24 in. directly above the laser beams, aligned along the beams. This produces a snowfall which is about 3 in. wide and 28 in. long, which falls through the coincident laser beams. The snowfield generator and operation are described in Ref. 1.

Figure 2 is a sketch relating the snowfield, laser beam, and field camera viewing direction. A still camera is positioned to view the snowfield from a direction perpendicular to the laser beam as indicated in the sketch. Illumination is provided by strobe lights to give a stop-action picture of the snowfield for posttest analysis.

2.2 TEST PROCEDURE

Starting with the lasers aligned and operating, the snow generator plate is cooled to operating temperature (-90°F) and maintained at this temperature. The plates are then cleared by knocking off the accumulated frost.

The snowfall density is controlled by varying the snow growth time. For the present tests, it was found that measurable laser attenuation could be obtained using snow growth times in excess of two minutes, with a ten-minute growth time completely attenuating the signal to the detectors.

Once the desired growth time has lapsed, the snow generator is impacted with a solenoid plunger to initiate the snowfall. After a time delay of 0.5 sec, transient recorders are activated to record the detector outputs. Typically, the snowfall begins to arrive at

the laser beam at about 0.7 sec, with the last of the snowfall passing through the beam at about 1.1 sec. At 0.9 sec, strobe lights are flashed to illuminate the snowfield for the field camera picture.

After each test the contents of the transient recorders are displayed on oscilloscope screens and recorded photographically. The laser beams are then blocked to establish the complete attenuation levels, and these levels are also displayed on the respective oscilloscope screens and recorded on the same photographs. A typical test result is shown in Fig. 3. Note that the position of the centerline of the laser beam at 0.9 sec is indicated in the snowfield picture. The snowflakes along the centerline produced the laser beam attenuation recorded at 0.9 sec. Prior attenuation resulted from the interaction with the snowflakes which had previously crossed the indicated laser beam centerline, while subsequent attenuation is caused by the snowflakes recorded above the laser beam centerline in the snowfield picture. Similar test results for all test data are presented in Appendix A.

The test log (Table 2) lists the pertinent parameters for the tests.

2.3 SNOWFIELD CHARACTERIZATION

The posttest characterization of the snowfield is accomplished from analysis of the single field camera picture obtained on each run. The location of the laser beam centerline is established in the snowfield picture. The field is subdivided into 3- by 3-in. areas, with the first strip centered along the laser beam centerline as indicated in Fig. 2. Subsequent strips of squares are located at intervals of 3 in. above and below the centerline.

Each 3- by 3-in. area is examined using a Quantimet® 720 image analyzing computer which counts the number of particles in a preselected size range and gives the total area of particles in that size range contained with the 3- by 3-in. area. Twenty-two different size ranges are considered. This information is recorded on paper tape for eventual computer processing.

The 3-in. size represents the lateral depth of the snowfield. Therefore, a side view of a 3- by 3-in. area contains all the flakes included in a 3- by 3- by 3-in. cell. The population information for each 3-in. cell in the snowfield is recorded and available for processing. A sample of the available snowflake size distribution data is given in Table 3 for a particular cell on a particular run. These raw data are available for each cell in each snowfield.

These snowfield data are computer processed, starting with the uprange cell through which the laser beams enter the snowfall. The total area of snowflakes within each size

range is divided by the number of flakes in that size range to find an average snowflake area. This area is assumed to be circular, and the resulting diameter is then found. This diameter is used for subsequent calculations.

Snowflake number density is assumed to be uniformly distributed within a cell, but may differ from cell to cell. The assumption of uniform distribution within a cell is necessary to infer the number of flakes that populate the 1-in.-diam cylindrical volume of the laser beams within that cell at a particular time.

The snowflakes along the laser beam centerline in the field camera picture produce the measured attenuation at 0.9 sec. The cell contents are also analyzed for cells located in intervals of 3 in. above and below the centerline. It is assumed that the snowfall velocity is such that 0.08 sec give a fall of 3 in. Therefore, sampling the cells 3 in. above the centerline gives the snowfield distribution at 0.92 sec, while the cells centered 3 in. below the centerline give the distribution at 0.82 sec. This correspondence between the snowflake distribution at some elevation at time equal 0.9 sec and the distribution on the laser beam centerline at another time assumes a uniform falling velocity for all size snowflakes. Since large flakes fall faster than smaller flakes, this correspondence becomes increasingly inexact with increasing distance from the centerline at 0.9 sec.

2.4 ATTENUATION DATA REDUCTION

The laser beam attenuation is measured directly from the output of the detectors. The no-snow case is taken to give complete signal transmission, while the complete attenuation detector signal level is determined by completely blocking the laser beam. The detector output is a linear function of the laser beam transmission.

The individual effect of large flakes can be seen in the early portions of the data traces, for both laser wavelengths. Also, the CO_2 detector gave a noisy signal, so that some smoothing is required to extract the attenuation data. The data prints shown for comparison with the calculated attenuation values were read from the traces at selected time intervals. The attenuation data are tabulated in Table 4, which gives the ratio of the attenuated signal to the no-snow signal levels, as a function of time.

3.0 ANALYSIS

3.1 INTRODUCTION

This analysis is intended to aid in the interpretation of the present laboratory experiments. The analysis is, therefore, specifically directed toward this limited objective.

The analysis has been divided into three parts, the first of which consists of evaluating the effect of a single scattering particle. The second part models the effect of multiple scattering particles, and in the third part, the results are applied to the experimental snowfields to give laser beam attenuation predictions for the present tests.

3.2 ATTENUATION BY SINGLE PARTICLE

The experimental arrangement assumed has been shown in Fig. 1, and the pertinent dimensions are given in the sketch (Fig. 4). The laser beam is assumed to be of uniform intensity, collimated, and be at least as large as the detector diameter. The detector diameter is assumed to be larger with respect to the scattering particle. The particle, in turn, is assumed to be much larger than the laser wavelength. Finally, the distance from the particle to the detector (ℓ) is assumed to be large with respect to any other dimensions.

The particle is assumed to be a sphere, and under the present set of assumptions, Fraunhofer differentiation theory can be employed (Ref. 2). Figure 5 depicts the radiation intensity pattern, which is anticipated on the detector. First, all the incident radiation in an area of twice the geometrical cross section of the particle is scattered. Therefore, only scattered radiation appears within this area on the detector surface. Outside this area, both the incident and scattered radiation are present and are assumed to be additive.

The power to the detector is given by

$$P = I_o \left[\int_o^{A_d} (I_s/I_o)\, dA + \int_{A_s}^{A_L} dA \right]$$

$$= I_o \left[A_L - A_s + \int_o^{A_d} (I_s/I_o)\, dA \right] \tag{1}$$

Let

$$A_e = - \int_o^{A_d} (I_s/I_o)\, dA + A_s$$

$$dA = 2\pi r dr \qquad r = \ell \tan\theta \qquad dr = \frac{\ell}{\cos^2\theta}\, d\theta \qquad \theta_{max} = \tan^{-1}\left(\frac{D_d}{2\ell}\right)$$

Then,

$$A_e = -2\pi \left[\ell^2 \int_0^{\tan^{-1}\left(\frac{D_d}{2\ell}\right)} \left(\frac{I_s}{I_o}\right)\left(\frac{\tan\theta}{\cos^2\theta}\right) d\theta - D_p^2/4 \right] \tag{2}$$

A_e is the effective area of extinction. The power to the detector is then given by

$$P = I_o A_L \left(1 - \frac{A_e}{A_L}\right)$$

This is equivalent to assuming the initial intensity (I_o) acts on the fraction of detector area ($1 - A_e/A_L$), while no radiation is received by the fraction of the detector area given by A_e/A_L.

The equation expressing Fraunhofer diffraction intensity distribution (Ref. 3) is

$$\frac{I_s}{I_o} = \frac{1}{k^2} X^4 \left[\frac{J_1 (X \sin\theta)}{X \sin\theta}\right]^2 \tag{3}$$

where

$$X = \pi D_p/\lambda$$

$$k^2 = (2\pi\ell/\lambda)^2$$

and J_1 is the first-order Bessel function.

The ratio of the detector signal expected with a single scattering particle to that expected without scattering is

$$\frac{P}{P_o} = \left(1 - \frac{A_e}{A_L}\right) \tag{4}$$

where

$$A_e = -\frac{\pi D_p^2}{2} \left\{ X^2 \int_0^{\theta_{max}} \left[\frac{J_1 (X \sin\theta)}{X \sin\theta}\right]^2 \frac{\tan\theta}{\cos^2\theta} \, d\theta - 1 \right\} \tag{5}$$

Equation (5) has been evaluated for both 0.6328 and 10.6 μ radiation, using ℓ = 28 ft and D_d = 0.5 in. The results shown in Fig. 6 compare these calculations and the results with no scattering in the direction of the detector. For the shorter wavelength radiation, scattering in the direction of the detector makes an appreciable contribution to A_e.

The results in Fig. 6 can be approximated by

$$A_{e_{0.6328}} = \exp\left\{-19.124707 + 1.8015599\ \ell n\ D_p + 0.00539783\ (\ell n\ D_p)^2\right\} \quad (6)$$

$$A_{e_{10.6}} = \exp\left\{-21.2492 + 2.491378\ \ell n\ D_p - 0.04095798\ (\ell n\ D_p)^2\right\} \quad (7)$$

with A_e in in.^{2} and D_p in microns, and where $\ell n\ D_p$ is the natural log of the particle diameter.

Figure 7 shows the signal attenuation due to a single scattering particle. The contribution of the forward scattering component is frequency dependent, and the results for 0.6328 and 10.6 μ are compared. The attenuation is shown to increase with both particle size and wavelength. This comparison is specifically for ℓ = 28 ft, D_d = 0.5 in., and D_L = 2 in.

3.3 ATTENUATION BY MULTIPLE PARTICLES

The experimental configuration is such that the laser beam is attenuated by a cloud of particles. This configuration has been depicted in Fig. 2. The field has a limited width (W) and in practice is viewed from a direction perpendicular to the path of the laser beam by a field camera. The field camera is used for posttest evaluation of the attenuation environment.

The field is subdivided into cubes of dimension W for analysis, as shown in Fig. 8. The side view gives the number of particles in the various size ranges contained within the cell. The number of particles in the i^{th} size range in the laser view is

$$N_{L,i} = N_{SV,i} \cdot \frac{\pi D_L^2}{4W^2} \quad (8)$$

The particles within a particular cell are assumed not to interact. Therefore, the scattering from various particles in a common cell is taken to be additive. The radiation which is transmitted through a cell is

$$P = I_o \left(\frac{\pi D_L^2}{4} - \sum_{i=1}^{M} N_{L,i}\, A_{e_i}\right) \quad (9)$$

where A_{e_i} is the extinction area of a single i^{th} sized particle; $N_{L,i}$ is the number of particles in the i^{th} size range as seen by the laser beam; and M is the number of size increments considered within the cell.

The extinction area is given by Eq. (6) or Eq. (7), and the $N_{SV,i}$ values are found from analysis of the field camera pictures. The radiation incident on the first cell is assumed

to be I_o acting on area A_L. After attenuation by the first cell, the radiation incident on the second cell is assumed to be I_o incident on A_L $(1 - A_1/A_L)$ with no radiation incident on area A_1. A_1 is defined as

$$A_j = \sum_{i=1}^{M} N_{L,i} A_{e_i} \Bigg|_{\text{cell } j} \tag{10}$$

with j = 1.

The radiation incident on subsequent cells is reduced by a factor of $(1 - A_j/A_{L_{th}})$ for each cell which is traversed. The radiation incident on the K^{th} cell is, therefore, I_o on an area $A_{I_o,K}$ with no radiation on $(A_L - A_{I_o,K})$. $A_{I_o,K}$ is given by

$$A_{I_o,K} = A_L \prod_{j=1}^{K-1} \left(1 - \frac{A_j}{A_L}\right) \tag{11}$$

This model is depicted in Fig. 9. In summary, no interactions are considered between particles in a common cell, but interactions are allowed between cells. By using this model, the signal after attenuation by K cells relative to the no attenuation signal is

$$\frac{P}{P_o} = \prod_{j=1}^{K} \left(1 - \frac{A_j}{A_L}\right) \tag{12}$$

3.4 LASER ATTENUATION PREDICTIONS

The well established analysis for scattering by a sphere has been applied in an approximate manner to the case of multiple scattering particles. The scattering performance of real particles with non-spherical shapes is assumed to be approximated by the performance of ideal spherical shapes.

The spherical shapes are described in terms of the diameter. The scattering performance of other shapes may be adequately correlated by some effective diameter which is related to the particle dimension. In the absence of other data, the mean particle diameter is taken to be the effective spherical diameter. The mean particle diameter is the square root of the particle area in the field camera picture.

The calculation procedure has been applied to each snowfield in the present tests, for various times during the snowfall for comparison with the measured attenuation.

The individual contribution of each size particle in the cell is calculated according to Eq. (6) or (7), weighted by the number of particles of that size range, using Eqs. (8) and (10), and the final result is obtained from Eq. (12). A sample comparison is

shown in Fig. 10 for the snowflake population encountered on runs 9 and 10. Comparisons are shown in Appendix B for all other tests.

Agreement between predicted and measured attenuation would imply that the random shaped snowflakes scatter radiation with the same efficiency as spheres with the same diameter based on matching areas. The experimental results indicate that the scattering efficiency of a snowflake may be slightly larger than for a sphere with the same cross-sectional area.

Since the intervening snowflake population is best defined at 0.9 sec, the comparisons between theory appropriate to spherical particles and the experimental attenuation have been made at 0.9 sec. The results are shown as Figs. 11 and 12, which are, respectively, appropriate to the 0.6328- and 10.6-μ wavelengths. The agreement between the calculated and measured attenuation is probably within the experimental data scatter. The best quadratic fit is also shown in the figures, but it is not apparent that this representation of the data is more justified than taking the calculated attenuation to represent the data.

3.5 LASER ATTENUATION PREDICTION FOR NATURAL SNOWFALL

The calculation model developed has been supported by the experimental data. It would be of interest to calculate the attenuation of a laser beam through a natural environment.

If the ranges are long so that the angle subtended by the target is small, some simplifications can be made in the calculations. For instance, if the range is 2,000 ft and the laser beam at the target is 1 in. in diameter, then the angle subtended by the target is small, and

$$\theta_{max} = \mathrm{Tan}^{-1}\left[\left(\frac{0.5}{12}\right)2000\right] = 1.19 \times 10^{-3} \text{ deg} \tag{13}$$

This small angle allows the intensity function (I_s/I_o) to be approximated by the value at $\theta_{max} \rightarrow 0$, i.e.,

$$\frac{I_s}{I_o} = \lim_{\theta \to o} \frac{X^4}{k^2}\left[\frac{J_1(X \sin\theta)}{X \sin\theta}\right]^2 = \frac{X^4}{4k^2} \tag{14}$$

The extinction area for a single particle is given in Eq. (2), which using Eq. (14) becomes

$$A_e = \pi\frac{D_p^2}{2} - \left(\frac{2\pi}{4}\right)\left(\frac{X^4}{k^2}\right)\int_o^{\theta_{max}} \frac{\tan\theta}{\cos^2\theta}\, d\theta \tag{15}$$

where

$$\frac{2\pi\ell^2 X^1}{4k^2} = \left(\frac{\pi D_p^2}{8}\right)\left(\frac{\pi D_p}{\lambda}\right)^2 \tag{16}$$

and

$$\int_0^{\theta_{max}} \frac{\tan\theta}{\cos^2\theta}\, d\theta = \frac{1}{2}\tan^2\theta_{max} \tag{17}$$

The extinction area for a single particle is, therefore, given by

$$A_e = \frac{\pi D_p^2}{2}\left[1 - \frac{1}{8}\left(\frac{\pi D_p}{\lambda}\right)^2 \tan^2\theta_{max}\right] \tag{18}$$

This expression is limited to small values of θ_{max} and replaces Eqs. (2), (3), and (5) with this restriction.

The next step is to extend this result for scattering from a single particle to the case of multiple particles. This is done using Eq. (9), which assumes no interaction between particles in a common cell,

$$P = I_o\left(\frac{\pi D_2^2}{4} - \sum_{i=1}^{M} N_{L,i}\, A_{e_i}\right) \tag{19}$$

The total extinction area of a cell is given by Eq. (10),

$$A_j = \sum_{i=1}^{M} N_{L,i}\, A_{e_i}\Big|_{cell\ j} \tag{20}$$

where the summation is performed over the number of snowflakes in the j^{th} cell in the i^{th} size range within the laser beam. Interaction between cells is given by Eq. (12),

$$\frac{P}{P_o} = \prod_{j=1}^{K}\left(1 - \frac{A_j}{A_{1_j}}\right) \tag{21}$$

Substitution of Eq. (20) into Eq. (21) gives:

$$\frac{P}{P_o} = \prod_{j=1}^{K} \left(1 - \frac{1}{A_L} \sum_{i=1}^{M} N_{L,i} A_{e_i} \right) \tag{22}$$

where A_L is the cross-sectional area of the laser beam in the j^{th} cell and K is the number of cells traversed by the laser beam.

The number of flakes in a given size range within the laser beam in a particular cell ($N_{L,i}$) is related to the unit number density of flakes in space (N_i) and the cell dimensions by

$$N_{L,i} = N_i \cdot A_L \cdot L_c \cdot \Delta D_{p,i} \tag{23}$$

where L_c is the extent of the cell in the direction of the laser beam and ΔD_{p_i} is the particle size range increment for the i^{th} size range. The upper product limit (K) in Eq. (22) is determined by the total extent of the snowfield,

$$K = L_T / L_c \tag{24}$$

Equation (23) becomes, with these substitutions,

$$\frac{P}{P_o} = \prod_{j=1}^{L_T/L_c} \left[1 - L_c \sum_{i=1}^{M} \Delta D_{p,i} N_i A_{e_i} \right] \tag{25}$$

If all cells are assumed to have a similar snowflake size distribution, then Eq. (25) can be replaced by

$$\frac{P}{P_o} = \left[1 - L_c \sum_{i=1}^{M} \Delta D_{p,1} N_i A_{e_i} \right]^{L_T/L_c} \tag{26}$$

The appropriate cell length (L_c) is not known, but a 3-in. length has been used for the analysis of the present experimental data. If the cell length approaches zero, Eq. (26) becomes

$$\lim_{L_c \to 0} \left[1 - L_c \sum_{i=1}^{M} \Delta D_{p,i} N_i A_{e_i} \right]^{L_T/L_c} = \exp \left(-L_T \sum_{i=1}^{M} \Delta D_{p,i} N_i A_{e_i} \right) \tag{27}$$

The final equation for the attenuation of a laser beam due to a natural snowfall is, therefore,

$$\frac{P}{P_o} = \exp\left(-S \sum_{i=1}^{M} \Delta D_{p,i} N_i A_{e_i}\right) \tag{28}$$

where P/P_o is the ratio of the laser power exiting the snowfall to the laser power incident on the snowfall, S is the distance into the snowfall, $\Delta D_{p,i}$ is the particle size range increment, N_i is the total number of particles in the i^{th} size range within a unit volume per unit size range, and A_{e_j} is the extinction area due to the presence of a single particle in the i^{th} size range. The analysis is restricted to large distances from the snowfield to target resulting in small angles (θ_{max}) subtended by the target. The quantity (A_{e_i}) is obtained from Eq. (18).

Information on the number density of snowflakes in a natural snowfall and an equation which expresses the number density as a function of liquid water content and particle dimension was obtained from AFSC/SAMSO:

$$N_i = 0.323 \ (\alpha/D_o)^4 \ \frac{m}{\rho} \ \exp(-\alpha D_i/D_o) \tag{29}$$

where N_i is the number of particles per unit volume per unit size range increment of melted diameter, and D_o is an "equivalent melted value" which is a function of the liquid water content (m) of the cloud.

$$D_o = 0.83 \ m^{0.286} \tag{30}$$

for small snow, and

$$D_o = 1.17 \ m^{0.226} \tag{31}$$

for large snow.

The term D_o is in millimeters with m in g/m^3, ρ is the density of water, taken to be 1 g/cm^3, and α is a constant 3.67. The equivalent melted diameter (D_i) is related to the unmelted dimension by

$$\begin{aligned} D_i &= 0.4 \ D_p^{0.782} && D_p < 0.5 \text{ MM} \\ D_i &= 0.37 \ D_p^{0.670} && D_p .> 0.5 \text{ MM} \end{aligned} \tag{32}$$

for small snowflakes, and

$$D_i = 0.4\ D_p^{0.782} \qquad D_p < 1\ MM$$
$$D_i = 0.4\ D_p^{0.875} \qquad D_p > 1\ MM \tag{33}$$

for large flakes.

Figure 13 shows the numerical evaluation of Eq. (28) for the case of $\theta_{max} = 1.19 \times 10^{-3}$ deg. The correlation of flake type (large or small) versus liquid water content (m) has been taken from a representative storm as given in Ref. 4. From Fig. 13, the attenuation due to 1,000 ft of a cloud of large snowflakes with a liquid water content of 0.2 g/m^3 is

$$\frac{P}{P_o} = \exp\ (-1000 \times 0.00177) = 0.17$$

Thus, the attenuation of a CO_2 laser beam by a snowfall appears to be a significant problem.

From the present study, it can be concluded that the attenuation of a low power density laser beam by a snowfall can be analyzed using geometric optics. For laser beams with power densities sufficiently large to effect the snowflakes, the laser attenuation may be appreciably different.

4.0 RESULTS AND CONCLUSIONS

The simultaneous attenuations of a CO_2 and a visible HeNe laser beam by a common snowfield have been measured in a laboratory experiment. The snowfields encountered have been characterized by counting the number of flakes in various size ranges.

In conjunction with the experiment, a calculation model has been developed to predict the attenuation due to individual flakes. This model assumes that the flake behaves as a sphere with the same cross-sectional area. The particle intercepts the radiation from an area of twice the particle geometric area, but some fraction of this radiation is scattered in the direction of the target.

The experimental laboratory results support the calculation model, which predicts a wavelength dependence on the quantity of radiation scattered toward the target, but no such dependence on the radiation intercepted by the particle. Therefore, as the distance from the particle to the target is increased, such that the angle subtended by the target as viewed from the scattering particle becomes small, the wavelength dependence also decreases. This result can be anticipated from Eq. (18) as $\theta_{max} \rightarrow 0$.

The present results have been extended to the case of the attenuation of a laser beam by a natural snowfall, by use of Eqs. (18) through (33). The result given in Fig. 13 is valid for both a 0.6328- or a 10.6-μ wavelength, since for an angle of θ_{max} = 1.19 x 10^{-3} deg or smaller, the difference at a liquid water content of 0.25 g/m^3 is less than 0.82 percent.

The laser testing capability developed for the present test can be readily expanded to different particulate fields, such as dust, cloud, or rain. The technology demonstrated for a high density snowfall of limited extent may also be applied in Range G to produce a longer expanse of low-density particulate environment for laser propagation testing, which more nearly duplicates that found in nature.

REFERENCES

1. Callens, E. Eugene, Jr., Blanks, James R., and Carver, Dwayne B. "Development of a Snow Erosion Test Capability for the Hyperballistic Range." Journal of Spacecraft and Rockets, Vol. 14, No. 3, March 1977, pp 183-188.

2. Dave, J. V. "Scattering of Visible Light by Large Water Spheres." Applied Optics, Vol. 8, No. 1, January 1969, pp. 155-164.

3. Van de Hulst, H. C. Light Scattering by Small Particles. John Wiley and Sons, Inc., New York, 1957, pp. 14, 107-108.

4. Plank, Vernon G. "Hydrometer Parameters Determined from the Radar Data of the SAMS Rain Erosion Program." AFCRL-TR-74-0249, June 4, 1974.

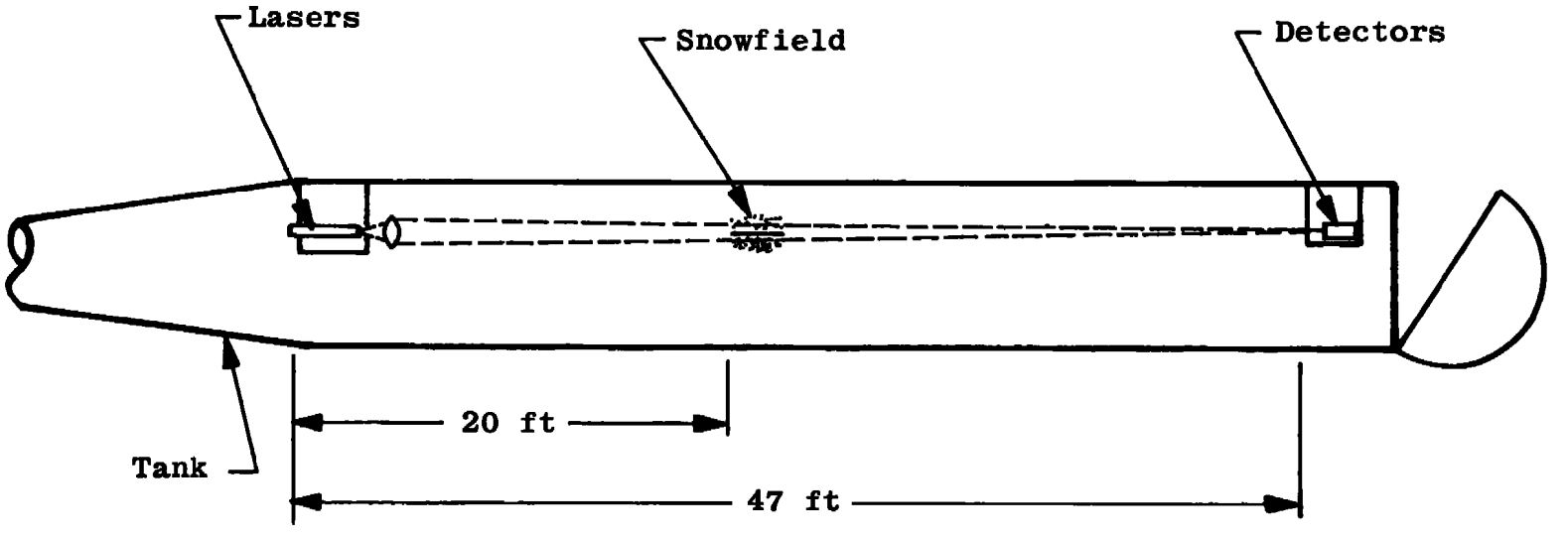

Test Schematic (View from Above)

Figure 1. Experimental arrangement.

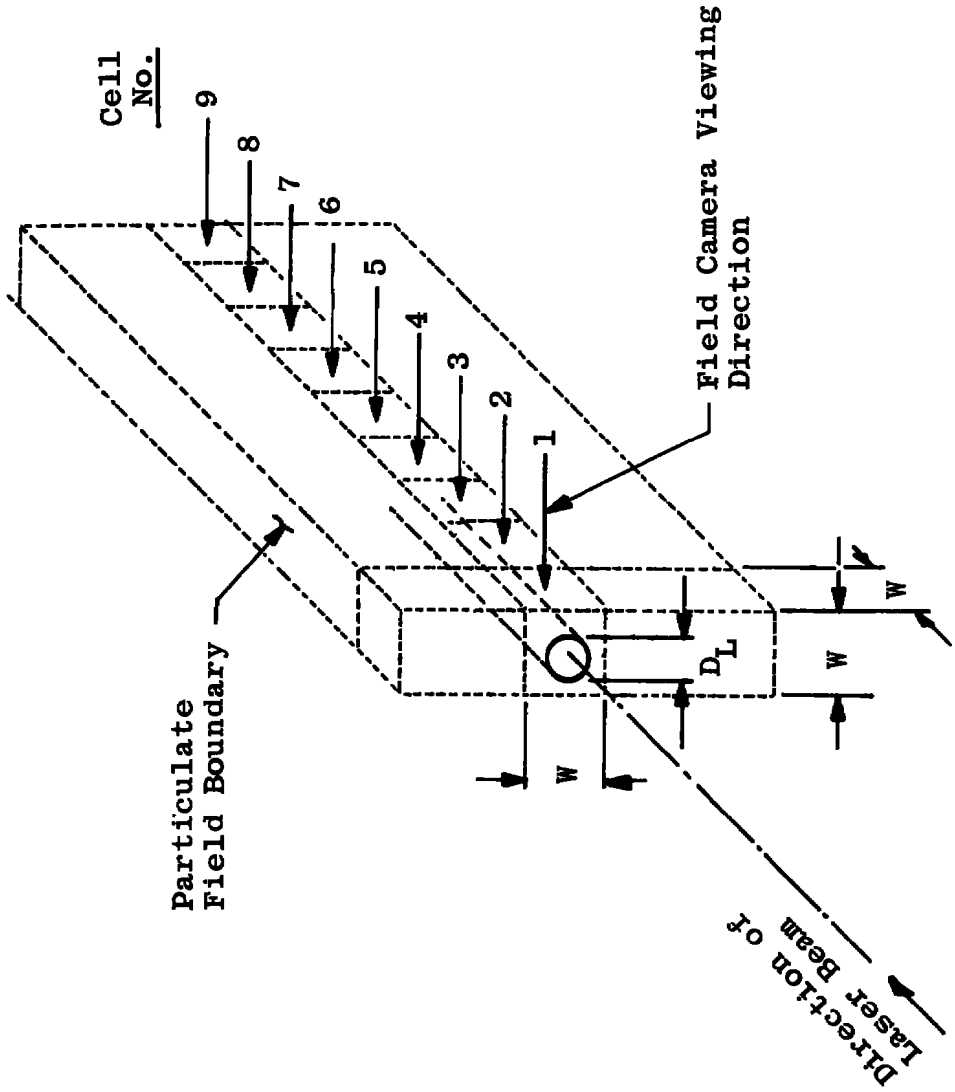

Figure 2. Sketch of attenuation field geometry.

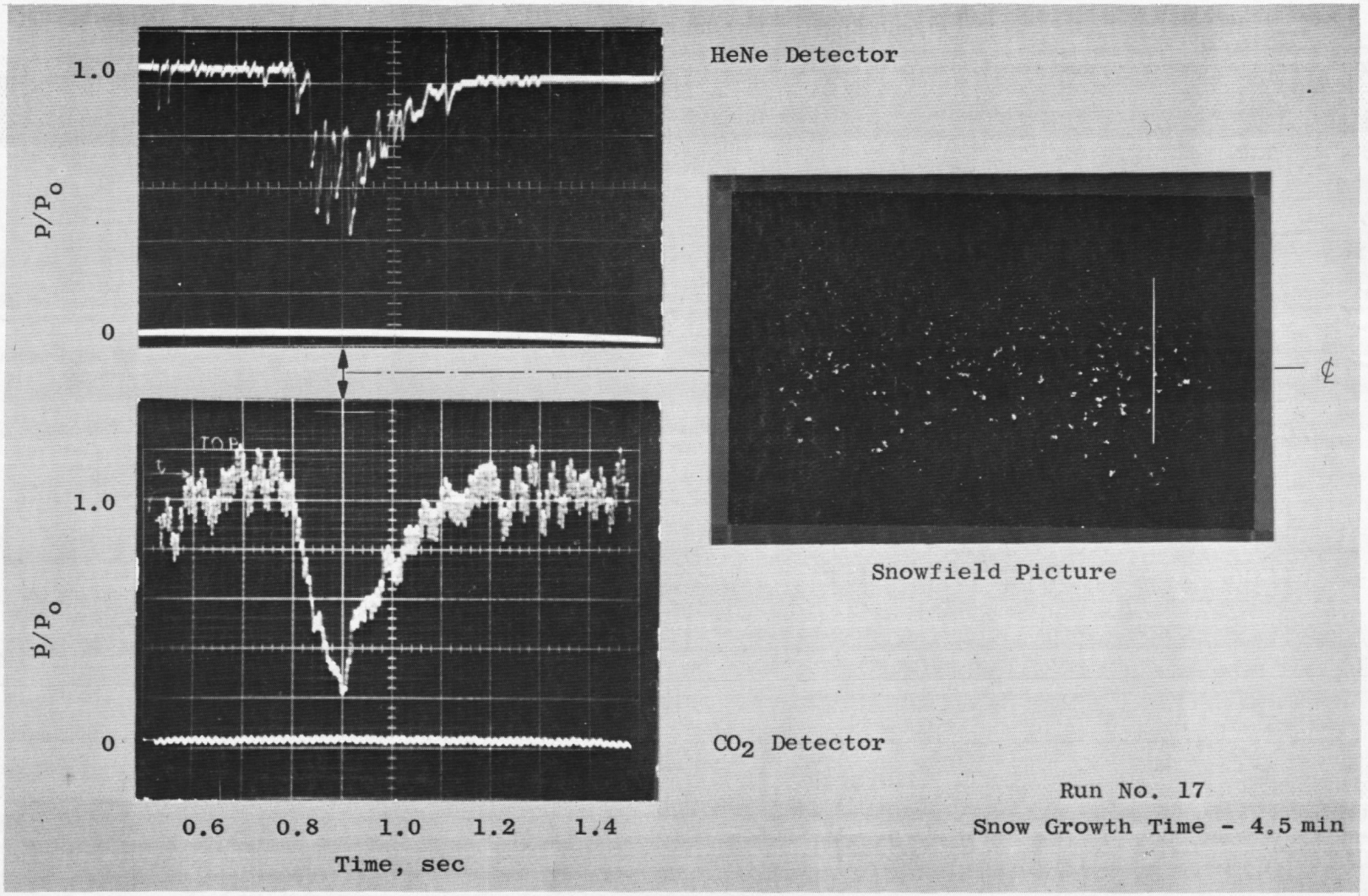

Figure 3. Typical test data.

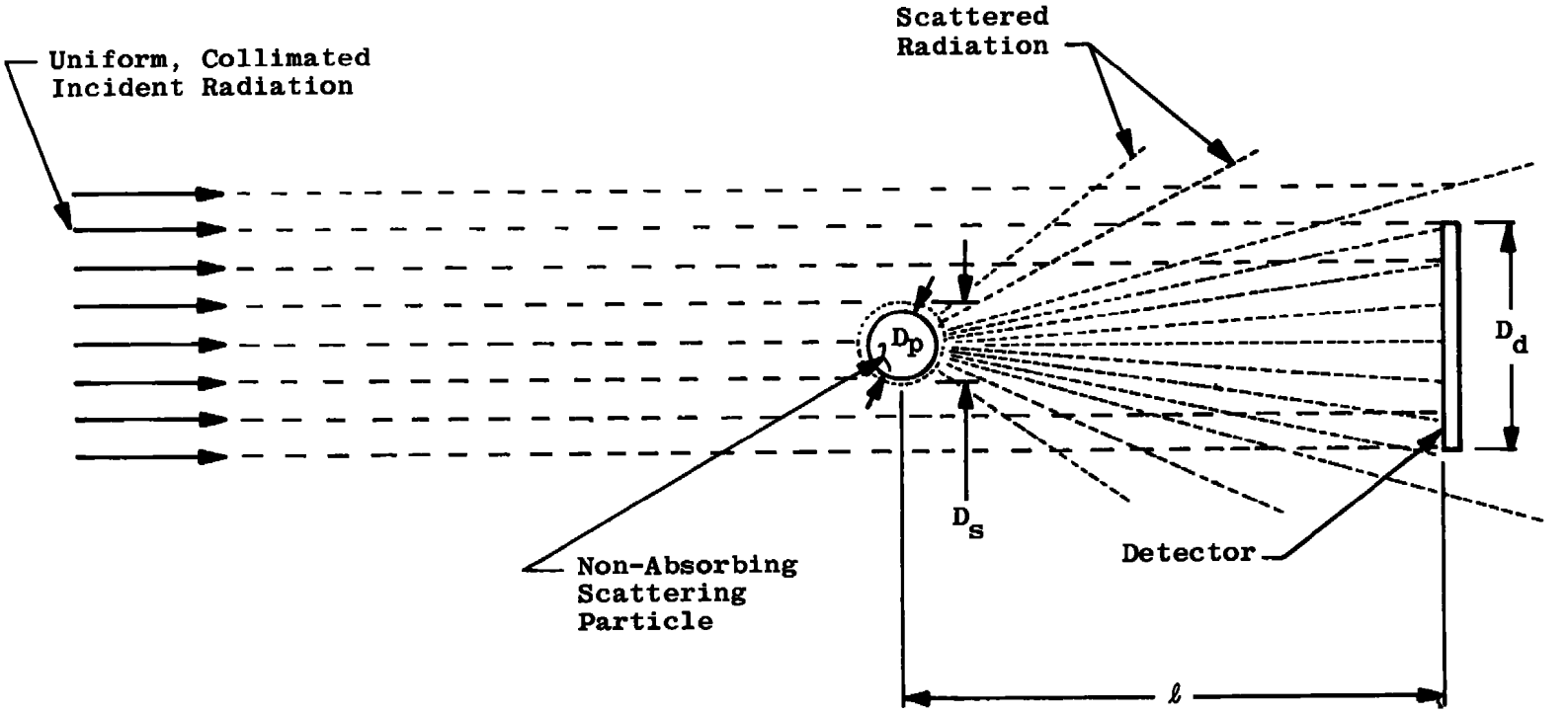

Figure 4. Scattering by single particle.

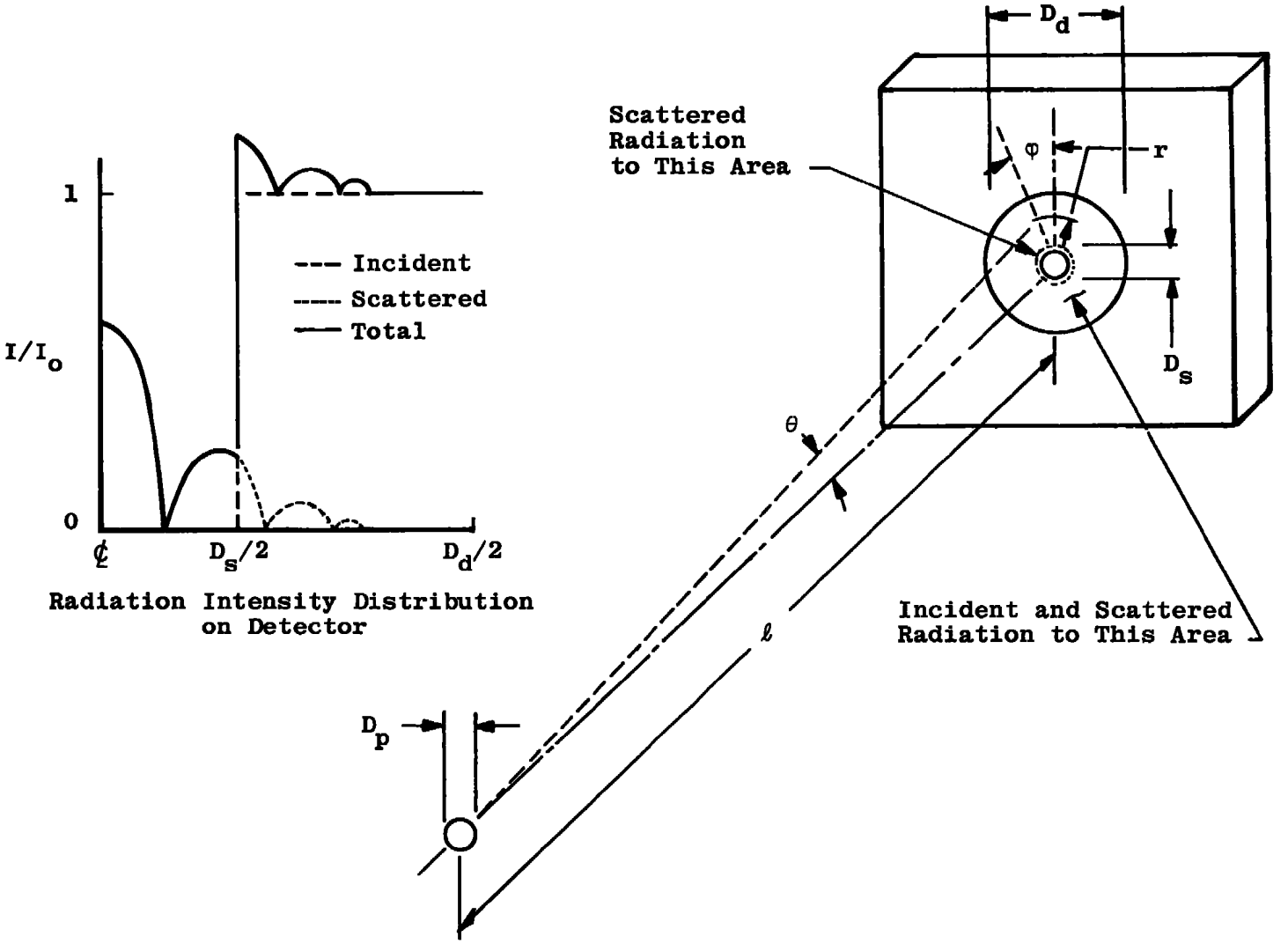

Figure 5. Radiation intensity distribution on detector.

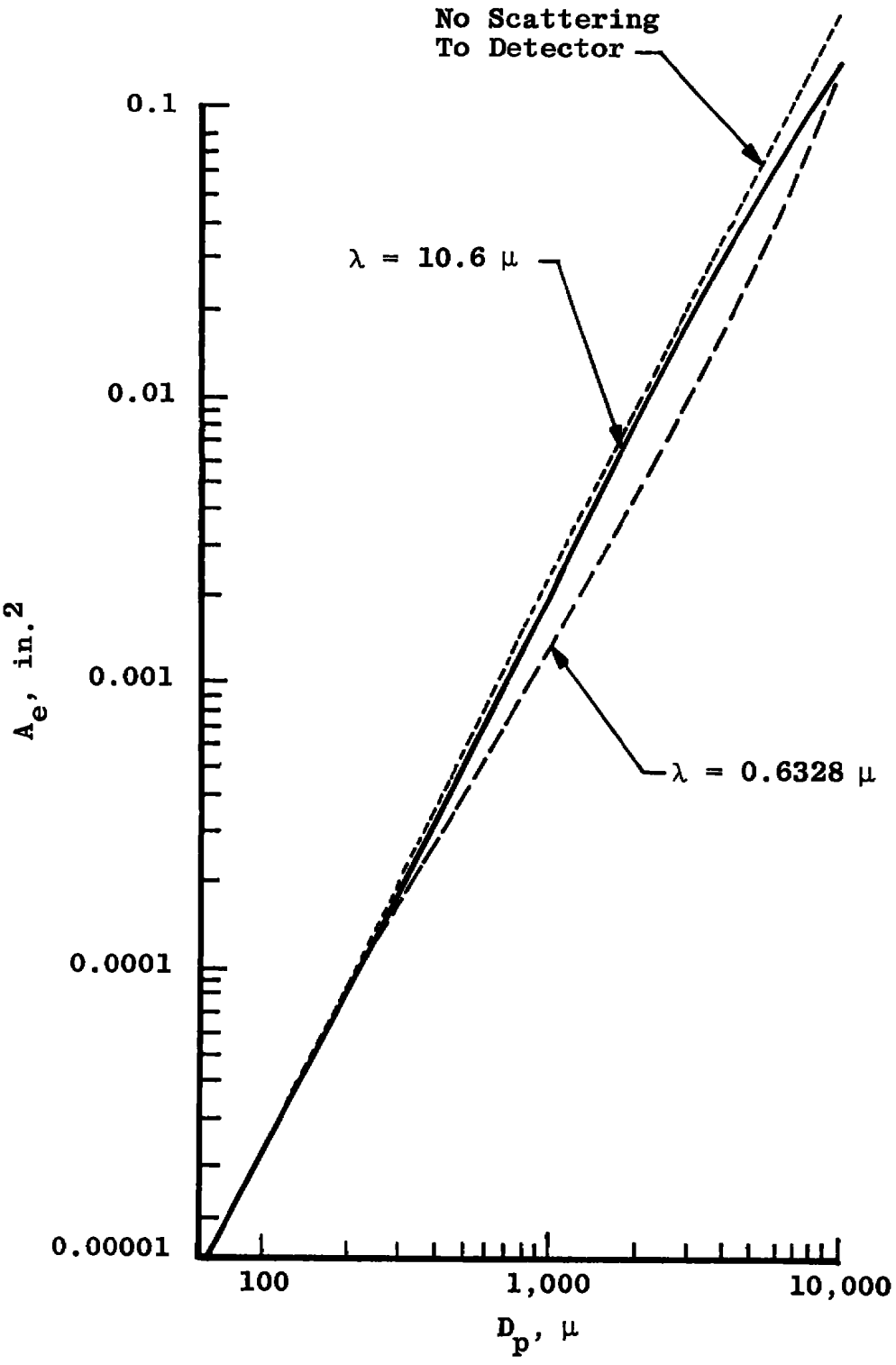

Figure 6. Effective extinction area of single particle.

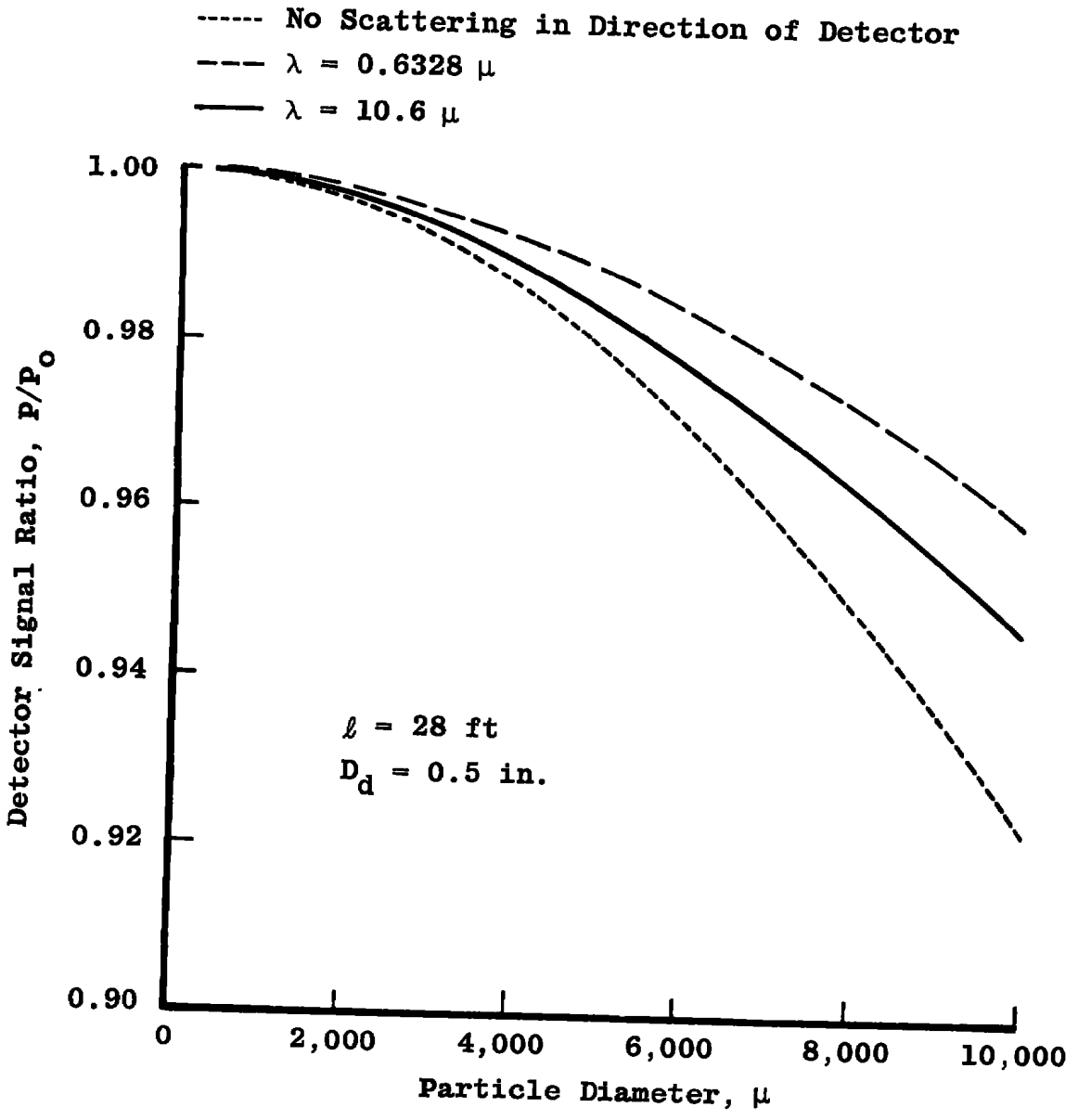

Figure 7. Signal attenuation ratio for single particle.

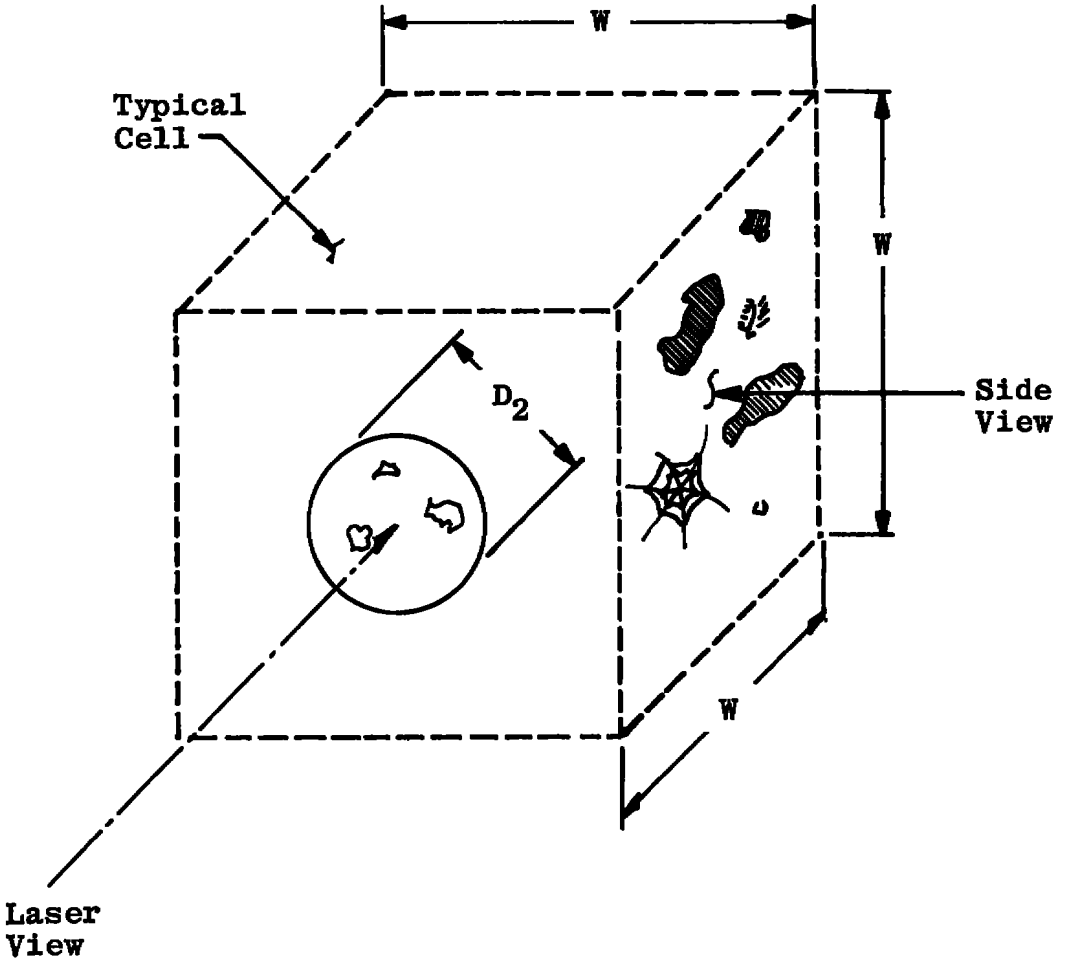

Figure 8. Typical cell for analysis of environment.

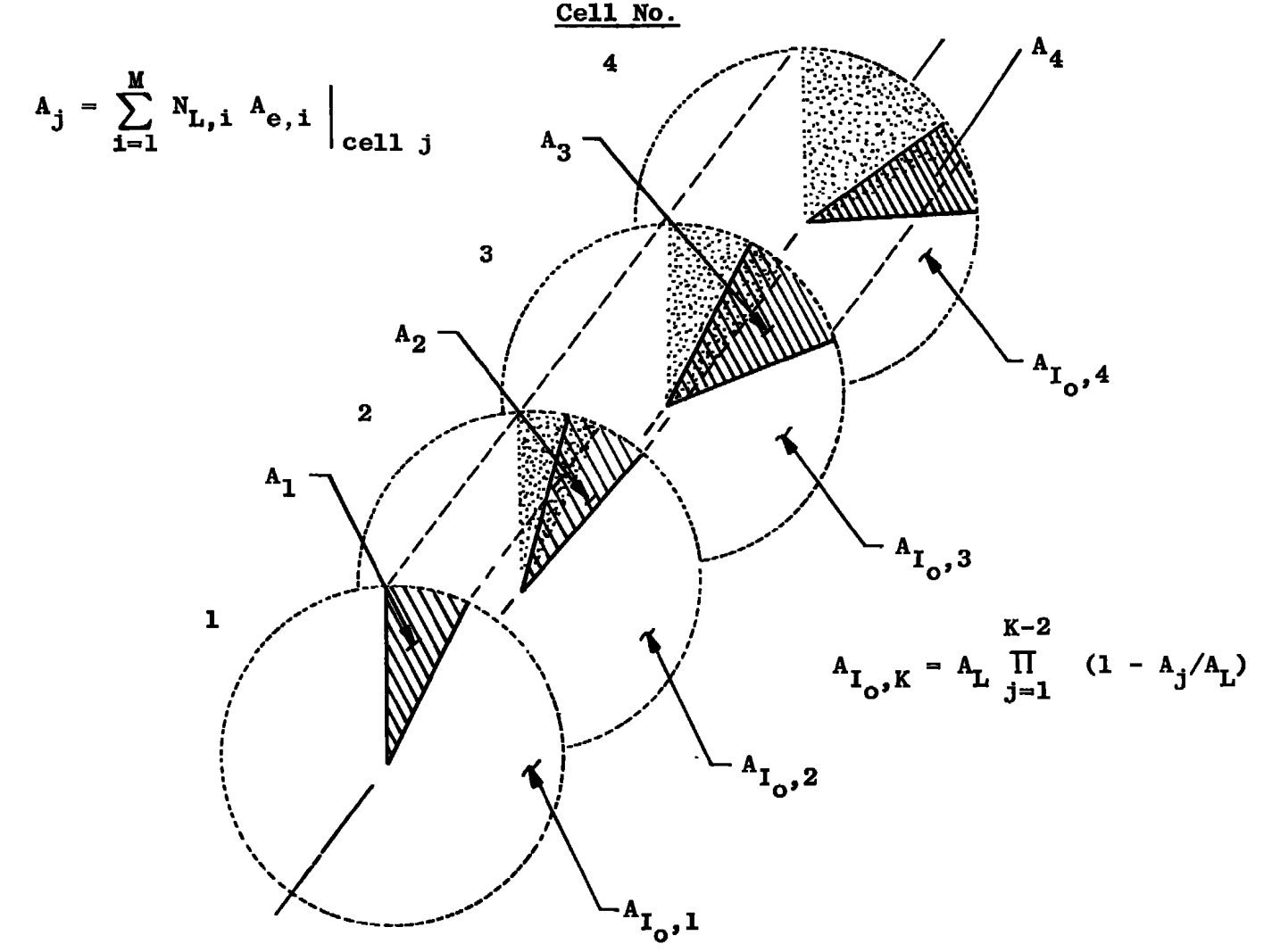

Figure 9. Cell attenuation interaction model.

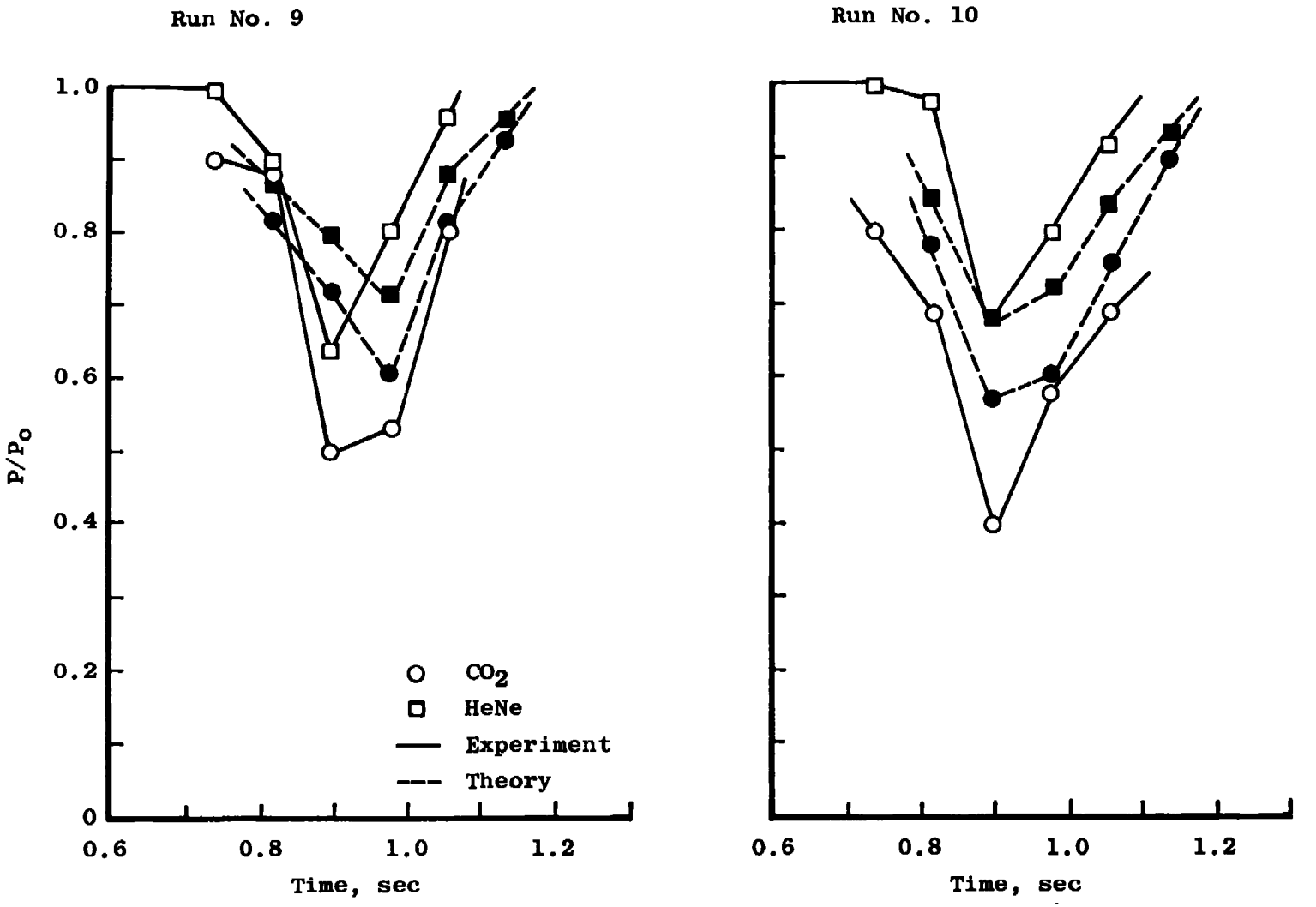

Figure 10. Comparison of experimental and predicted results - runs 9 and 10.

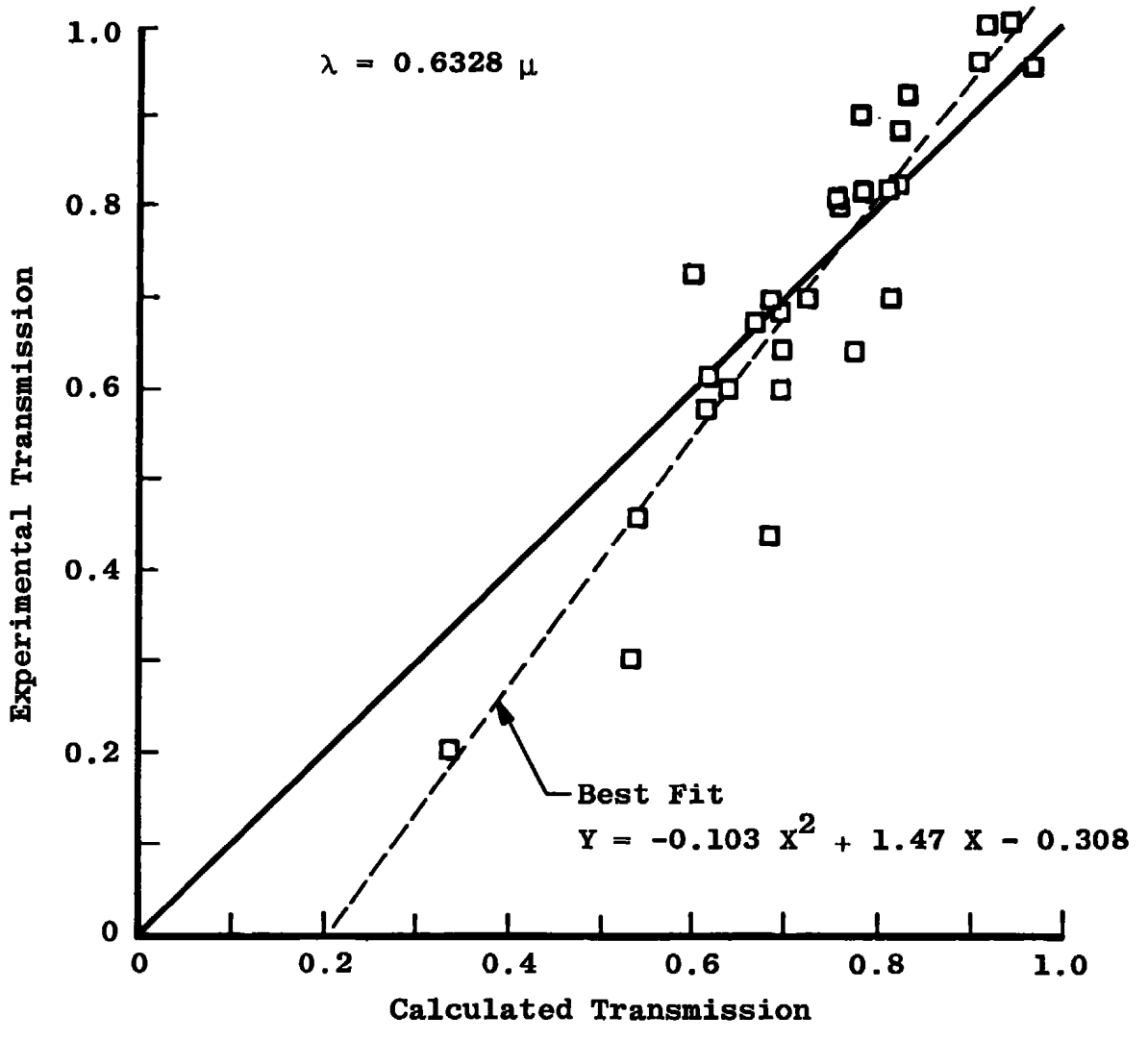

Figure 11. Comparison of calculated and experimental transmission of HeNe laser through snowfield - 0.9 sec.

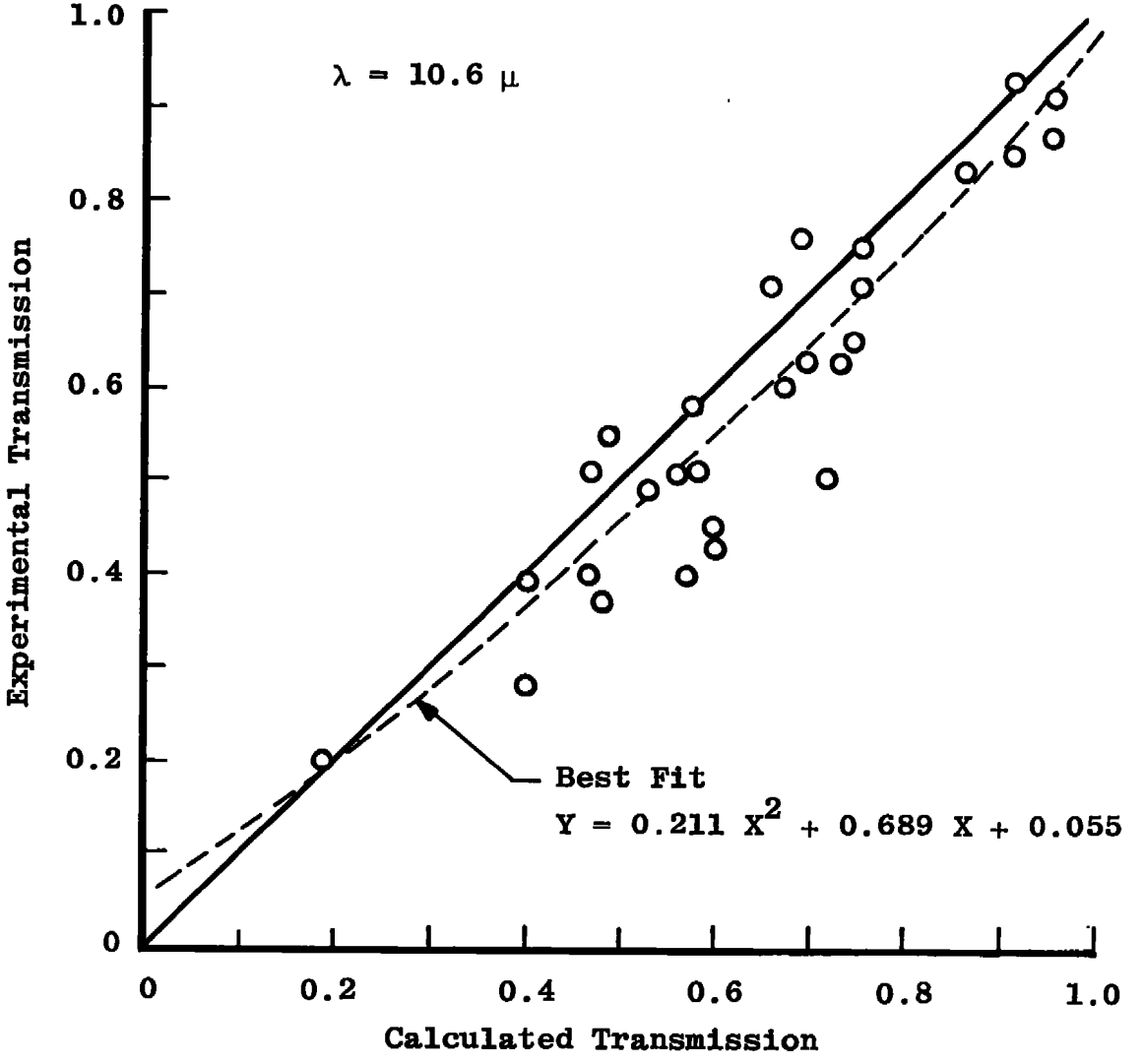

Figure 12. Comparison of calculated and experimental transmission of CO_2 laser through snowfield - 0.9 sec.

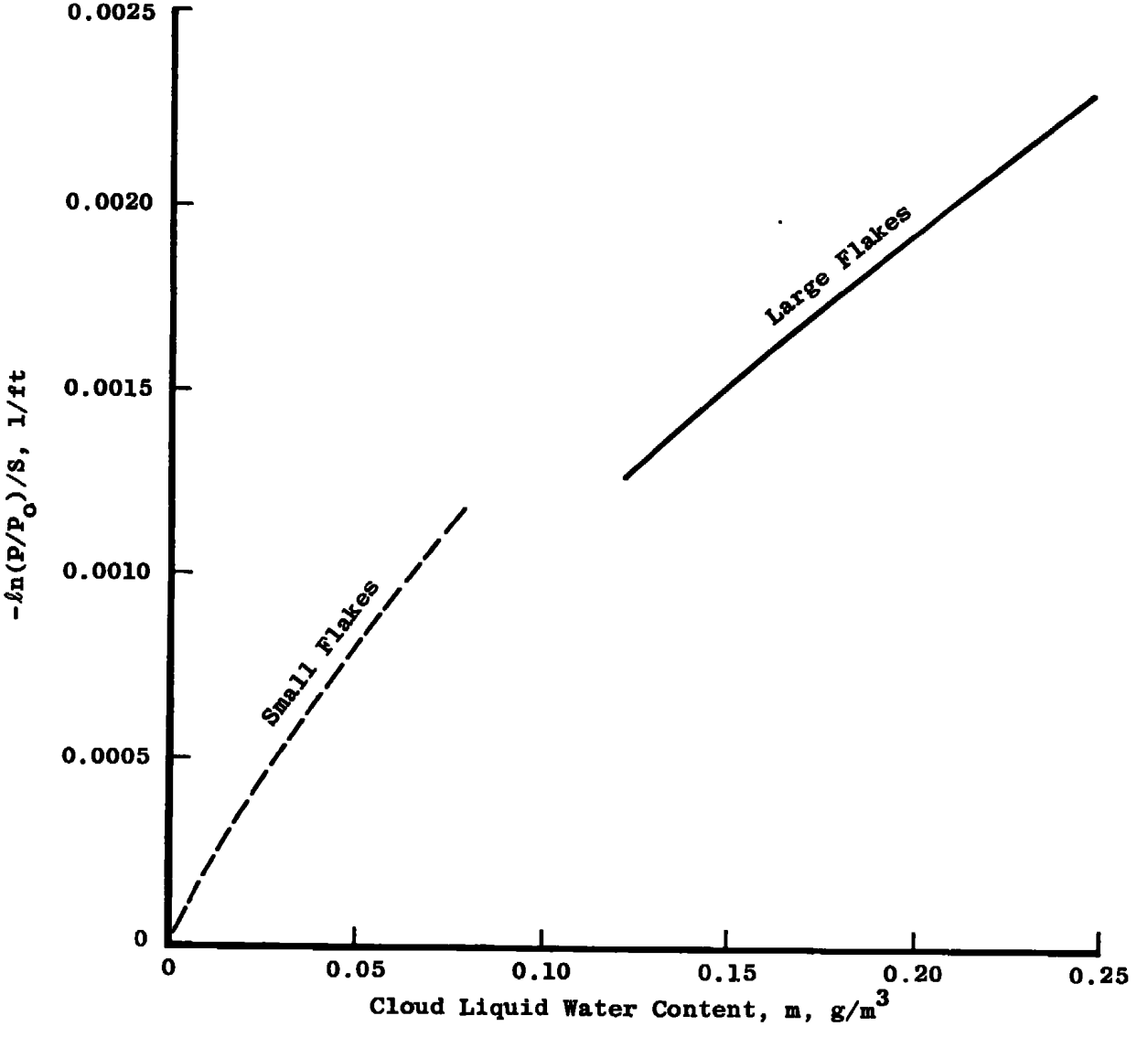

Figure 13. Attenuation prediction for natural snowfall.

Table 1. Equipment Description

HeNe Laser	Spectra Physics Model No. 124 Power Output - 15 mw continuous Beam Diameter - 1.5 mm Beam Divergence - 1 milliradian
HeNe Laser Detector	Metrologic Radiometer Model No. 60-530 Sensor Head - Silicón photosensor with radiometric filter Sensor Active Area - 0.385 cm^2 Frequency Response - 1 to 10 kHz Ranges - 0.3 microwatts to 30 milliwatts
CO_2 Laser	Sylvania Corporation 941P Power Output - 3 w continuous Beam Diameter - 4.5 mm Beam Divergence - 4 milliradians, total angle
CO_2 Laser Detector	Molectron Corporation PE3-00 Sensor Element - permanently poled pyroelectric crystal Sensor Active Area - 1 x 1.2 mm Rise time - 5 μsec Santa Barbara Research Center F256-2 Sensor Element - Photoconductive Mercury - Cadmium - Telluride Sensor Active Area - 1 x 1 mm Time Constant - < 10 μsec

Table 2. Test Log

Test No.	Date	Snow Growth Time, min	Dew Point °F	Remarks
5	6/22/77	8	66.8	No data traces
6		12		Noisy traces
7		5		Noise on HeNe trace
8		4		
9		3		
10		3		Zero on CO_2 trace
11		4.5		No traces recorded
12		4		
13		4		No field camera picture
14		4		
15		5		
16		5		
17		4.5		
18		6		
19		6		
24	6/28/77	4	63.3	No pictures
25		3.2		
26		4.5		
27		5		
28		4.3		
29		3.5		
30		3.8		
31		3		
32		18		
33		6.5		
34		4		
35		5		
36		6	60.8	
37		6		
38		6.5		
39	6/28/77	7	60.8	
40		7.5	60.8	
41		8	62.7	
42		10		
43		9		

Table 3. Sample Snowflake Size Distribution Data

Run No. = 19 Time = 0.9 sec

CELL 1		CELL 2		CELL 3	
Area (Picture Points)	Number of Flakes	Area (Picture Points)	Number of Flakes	Area (Picture Points)	Number of Flakes
0.1150D 02	2	0.1086D 02	7	0.9200D 01	5
0.2167D 02	3	0.2900D 02	2	0.2500D 02	1
0.2900D 02	2	0.3000D 02	2	0.3067D 02	3
0.4025D 02	4	0.4700D 02	1	0.4733D 02	3
0.6200D 02	1	0.6000D 02	2	0.0	2
0.7300D 02	1	0.6900D 02	2	0.7550D 02	2
0.9400D 02	0	0.8400D 02	1	0.9100D 02	1
0.2680D 03	1	0.0	1	0.2460D 03	1
0.2310D 03	1	0.1843D 03	4	0.2943D 03	3
0.3767D 03	6	0.4444D 03	5	0.3983D 03	4
0.6600D 03	1	0.6405D 03	2	0.5750D 03	1
0.8973D 03	3	0.7965D 03	2	0.9420D 03	1
0.1303D 04	4	0.1406D 04	3	0.1246D 04	4
0.1709D 04	2	0.1957D 04	1	0.2098D 04	3
0.2611D 04	2	0.2732D 04	1	0.0	0
0.4072D 04	2	0.0	0	0.3808D 04	1
0.0	0	0.0	0	0.0	0
0.0	0	0.7477D 04	1	0.0	0

210 picture points = 1 inch

Table 4. Attenuation Data

Run No.	CO_2 Time-sec 0.74	0.82	0.9	0.98	1.06	HeNe Time-sec 0.74	0.82	0.9	0.98	1.06
7	1.0	0.75	0.4	0.5	0.75	-	-	-	-	-
8	1.0	0.83	0.43	0.5	0.78	1.0	0.86	0.64	0.62	0.82
9	0.90	0.88	0.5	0.53	0.80	1.0	0.90	0.64	0.80	0.96
10	0.80	0.69	0.40	0.58	0.69	1.0	0.98	0.68	0.80	0.92
12	0.91	0.69	0.63	0.77	0.86	1.0	1.0	0.70	0.78	0.92
14	1.0	0.70	0.58	0.73	0.85	1.0	0.84	0.60	0.80	0.92
15	0.97	0.92	0.51	0.74	0.84	1.0	0.98	0.44	0.64	0.86
16	0.98	0.61	0.49	0.73	0.93	1.0	0.84	0.60	0.82	0.88
17	1.0	0.60	0.36	0.53	0.85	1.0	0.89	0.58	0.75	0.87
18	0.81	0.32	0.30	0.78	-.86	0.88	0.46	0.54	0.74	0.88
19	0.95	0.56	0.32	0.56	0.95	1.0	0.64	0.56	0.70	0.82

Table 4. Concluded

Run No.	CO_2 Time-sec							HeNe Time-sec						
	0.66	0.74	0.82	0.90	0.98	1.06	1.14	0.66	0.74	0.82	0.90	0.98	1.06	1.14
25	1.0	1.0	0.95	0.93	0.84	0.88	0.95	1.0	1.0	1.0	0.98	0.82	0.82	1.14
26	0.98	0.91	0.87	0.71	0.69	0.76	0.91	1.0	1.0	0.94	0.87	0.71	0.82	0.90
27	1.0	0.93	0.89	0.71	0.64	0.75	1.0	1.0	1.0	1.0	0.81	0.71	0.81	0.85
28	1.0	1.0	0.98	0.83	0.70	0.80	1.0	1.0	1.0	1.0	0.95	0.78	0.88	1.0
29	1.0	1.0	1.0	0.91	0.84	0.84	0.91	1.0	1.0	1.0	0.95	0.88	0.88	0.91
30	1.0	0.91	0.91	0.87	0.73	0.73	0.80	1.0	1.0	1.0	1.0	0.83	0.79	0.83
32	0.98	0.82	0.23	0.20	0.31	0.53	0.71	1.0	0.91	0.47	0.20	0.37	0.63	0.82
33	0.98	0.96	0.73	0.51	0.62	0.77	0.83	1.0	1.0	0.97	0.70	0.67	0.82	0.90
34	0.97	0.97	0.92	0.85	0.71	0.80	0.84	1.0	1.0	1.0	1.0	0.79	0.89	0.97
35	0.93	0.91	0.82	0.65	0.61	0.75	0.90	1.0	1.0	1.0	0.82	0.70	0.82	0.93
36	0.94	0.92	0.88	0.76	0.63	0.75	0.83	1.0	1.0	1.0	0.90	0.72	0.81	0.92
37	1.0	1.0	0.96	0.75	0.71	0.82	0.92	1.0	1.0	1.0	0.82	0.70	0.82	0.97
38	0.81	0.83	0.82	0.60	0.60	0.67	0.72	1.0	1.0	1.0	0.80	0.80	0.77	0.93
39	1.0	1.0	0.93	0.63	0.54	0.65	0.80	1.0	1.0	1.0	0.82	0.63	0.74	0.89
40	0.80	0.79	0.68	0.51	0.53	0.71	0.72	1.0	1.0	1.0	0.73	0.68	0.80	0.91
41	0.92	0.92	0.87	0.55	0.57	0.77	0.90	1.0	1.0	1.0	0.61	0.60	0.72	0.87
42	1.0	1.0	0.58	0.28	0.54	0.70	0.78	1.0	1.0	0.78	0.30	0.56	0.73	0.85
43	1.0	1.0	0.82	0.45	0.59	0.70	0.80	1.0	1.0	1.0	0.68	0.60	0.80	0.91

APPENDIX A
TEST DATA

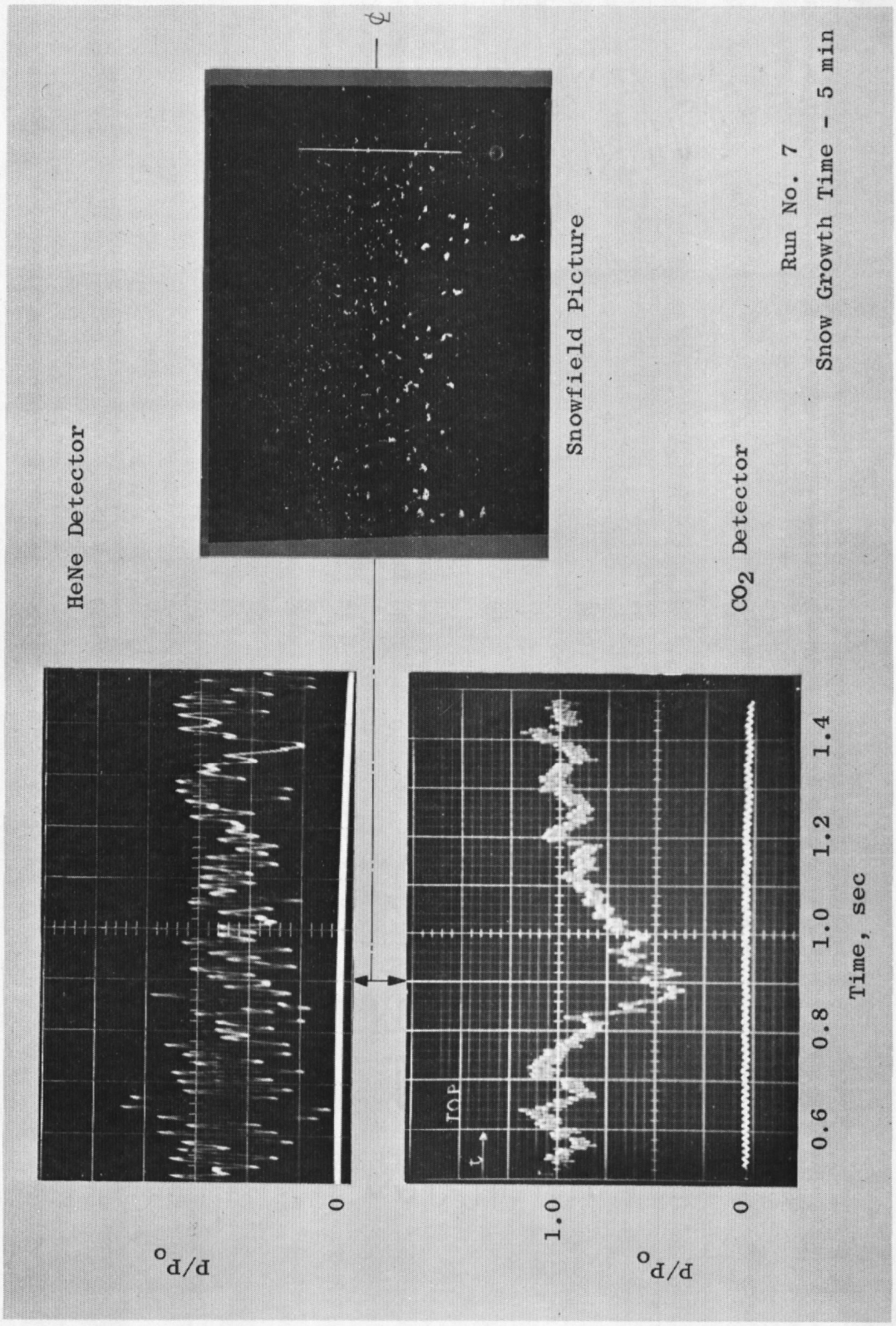
HeNe Detector
Snowfield Picture
CO_2 Detector
Run No. 7
Snow Growth Time - 5 min
P/P$_o$
1.0
0
0.6
0.8
1.0
1.2
1.4
Time, sec

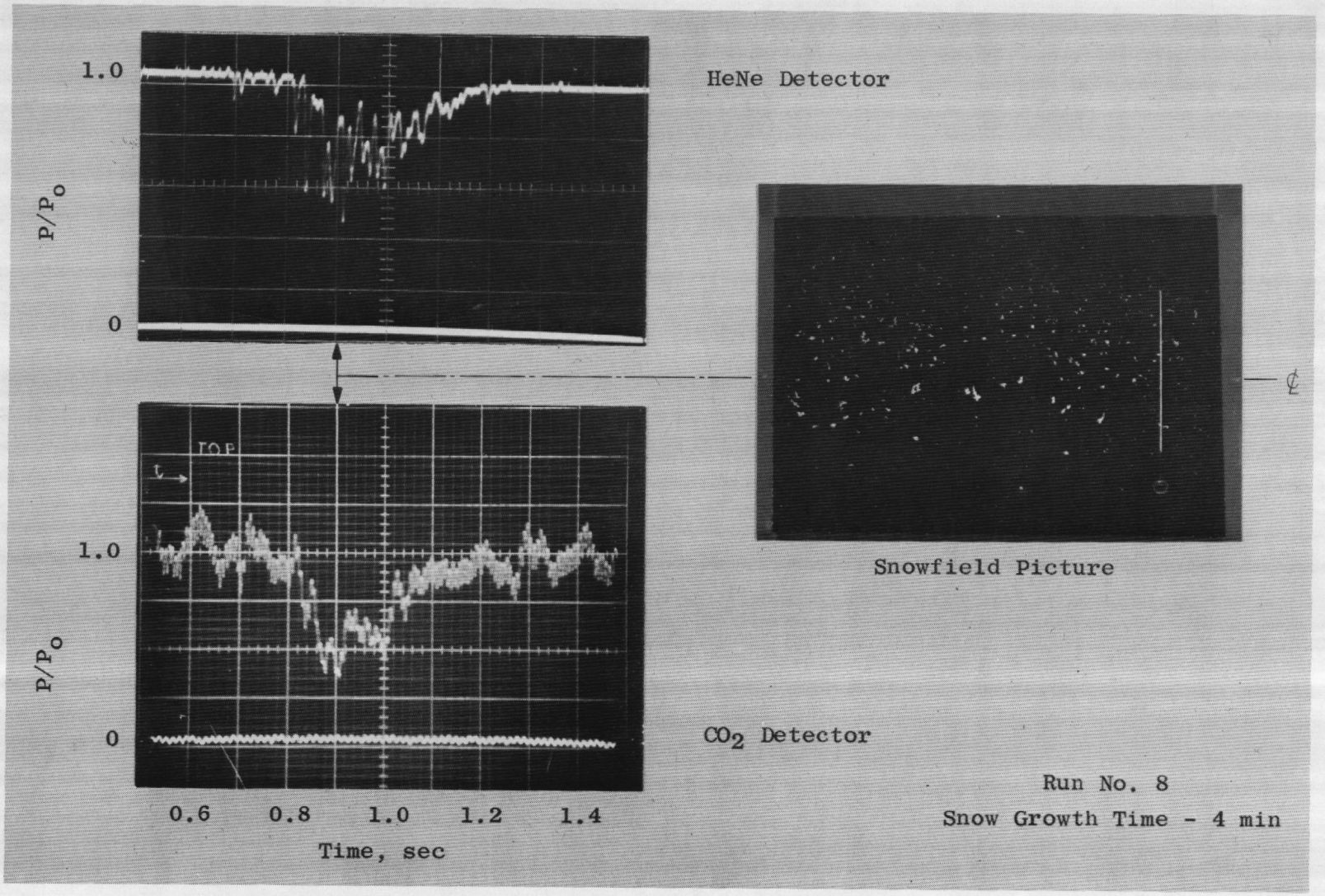
1.0
P/P$_o$
0
HeNe Detector
Snowfield Picture
℄
EOP
t_r
1.0
P/P$_o$
0
CO_2 Detector
0.6
0.8
1.0
1.2
1.4
Time, sec
Run No. 8
Snow Growth Time - 4 min

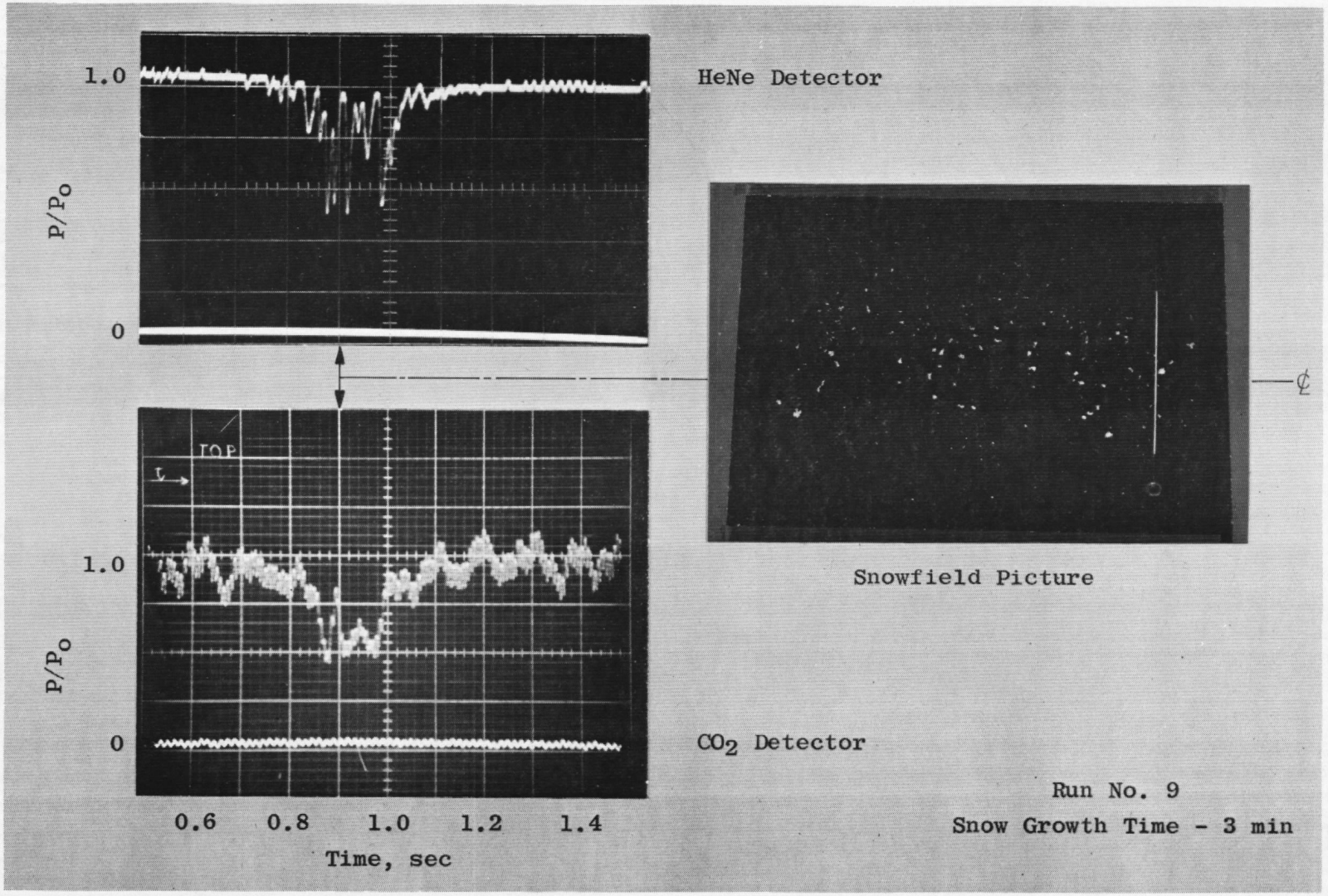
1.0
P/Po
0
HeNe Detector
Snowfield Picture
℄
1.0
P/Po
0
CO_2 Detector
0.6
0.8
1.0
1.2
1.4
Time, sec
Run No. 9
Snow Growth Time - 3 min

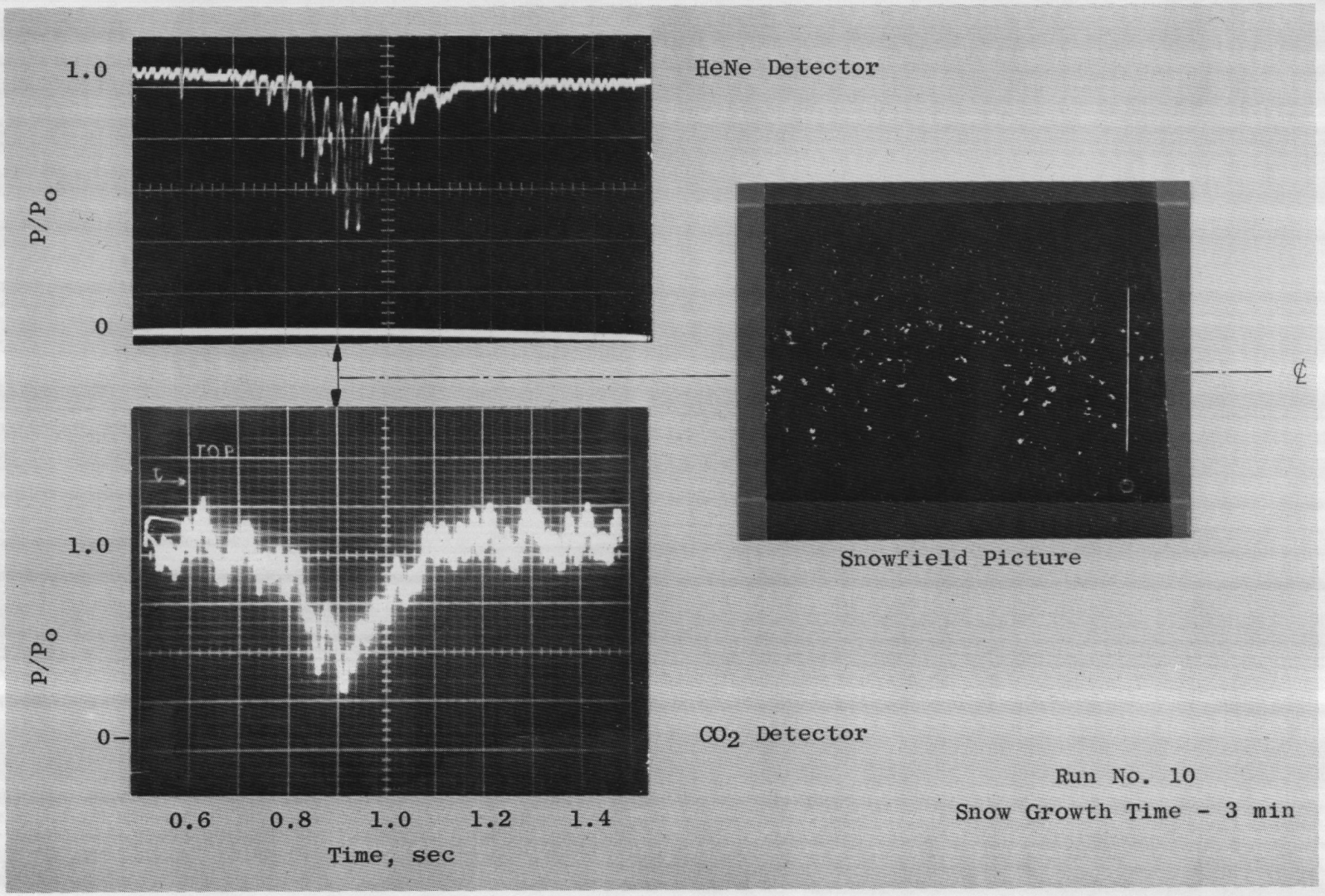
1.0
P/P$_o$
0
HeNe Detector
TOP
1.0
P/P$_o$
0
CO_2 Detector
0.6
0.8
1.0
1.2
1.4
Time, sec
Snowfield Picture
℄
Run No. 10
Snow Growth Time - 3 min

1.0
P/P$_o$
0
HeNe Detector
TOP
t
1.0
P/P$_o$
0
CO_2 Detector
0.6
0.8
1.0
1.2
1.4
Time, sec
Snowfield Picture
℄
Run No. 12
Snow Growth Time - 4 min

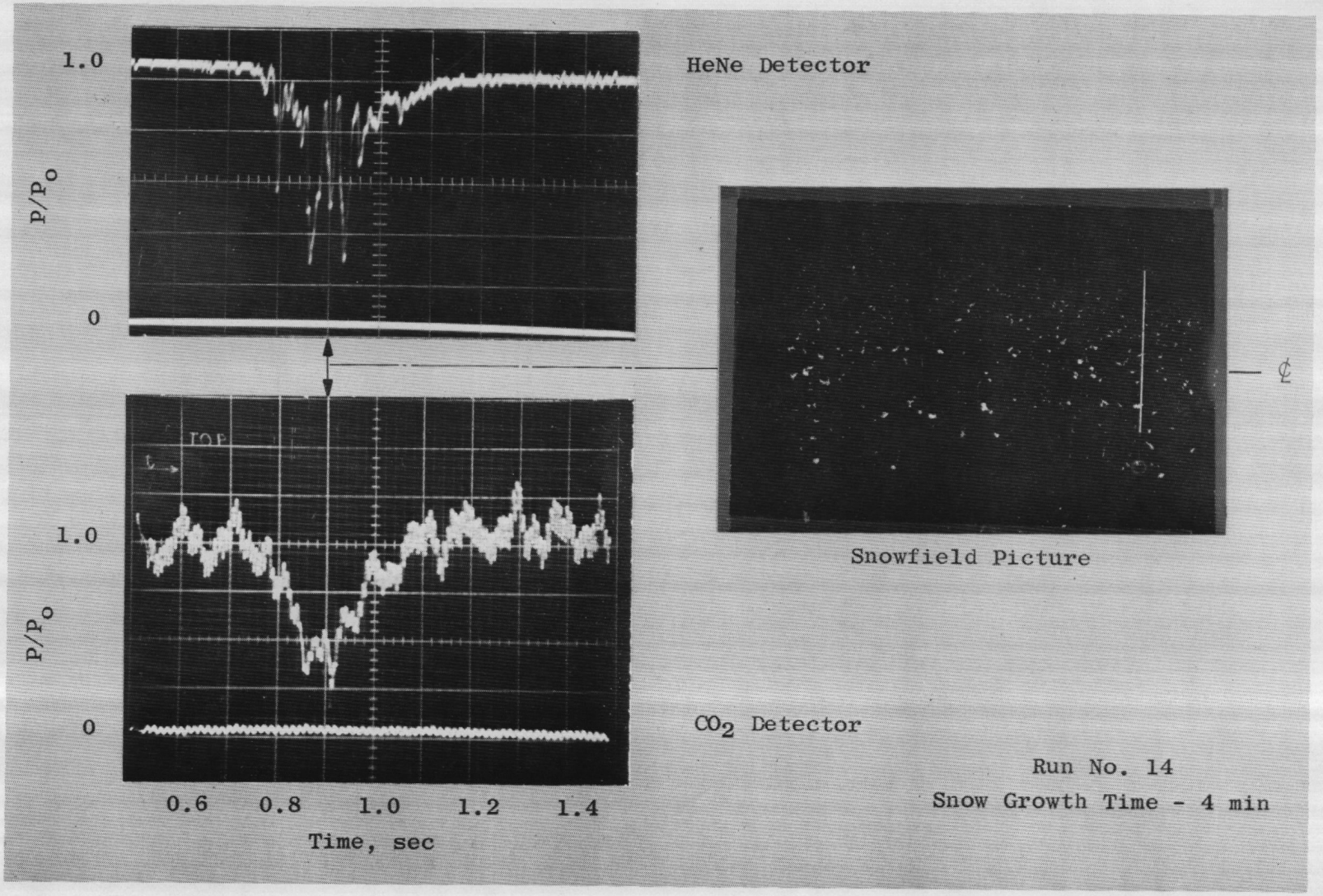
1.0
P/P$_o$
0
HeNe Detector
Snowfield Picture
℄
TOP
1.0
P/P$_o$
0
CO_2 Detector
0.6
0.8
1.0
1.2
1.4
Time, sec
Run No. 14
Snow Growth Time - 4 min

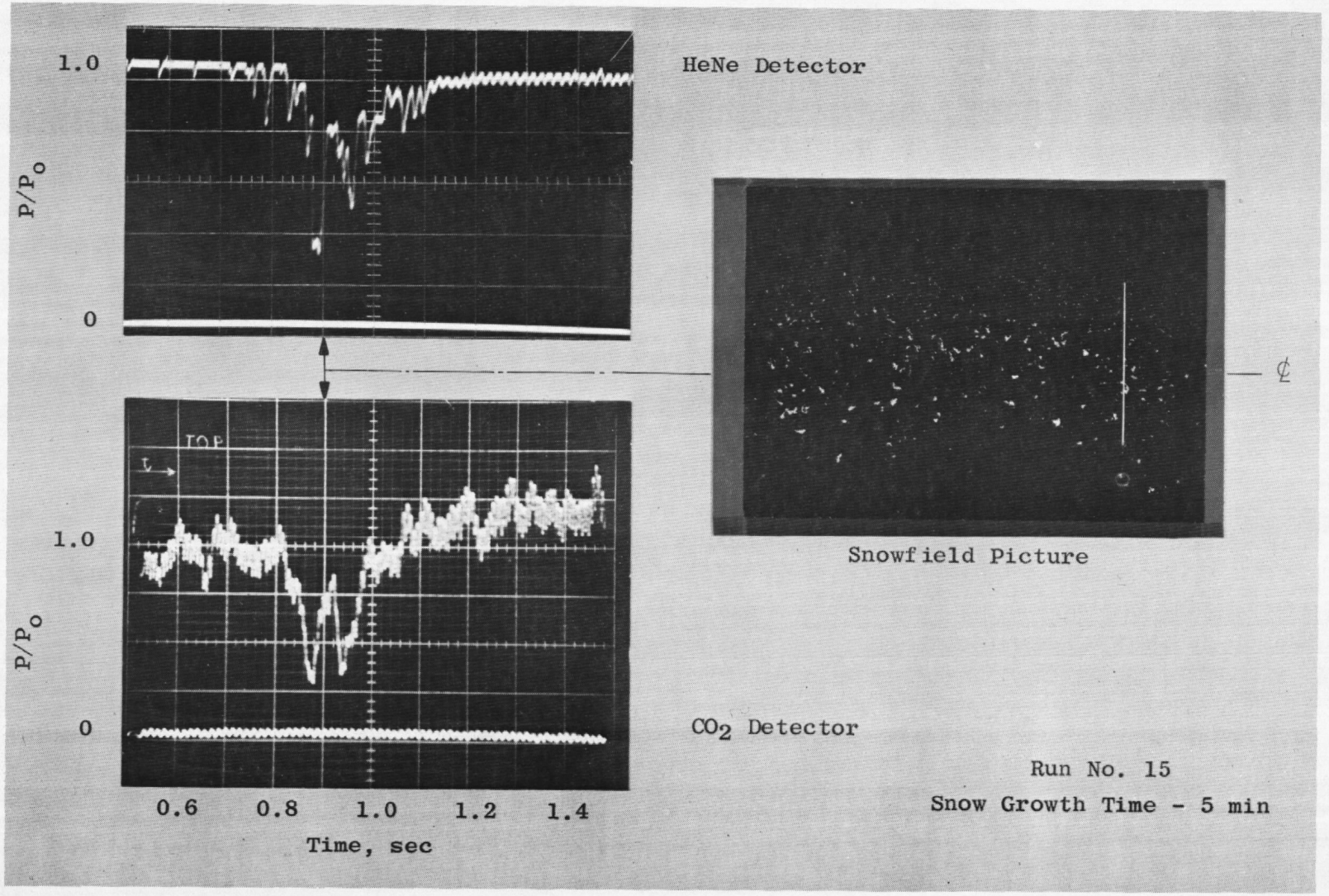
1.0
P/P$_o$
0
HeNe Detector
℄
Snowfield Picture
TOP
1.0
P/P$_o$
0
CO$_2$ Detector
0.6
0.8
1.0
1.2
1.4
Time, sec
Run No. 15
Snow Growth Time - 5 min

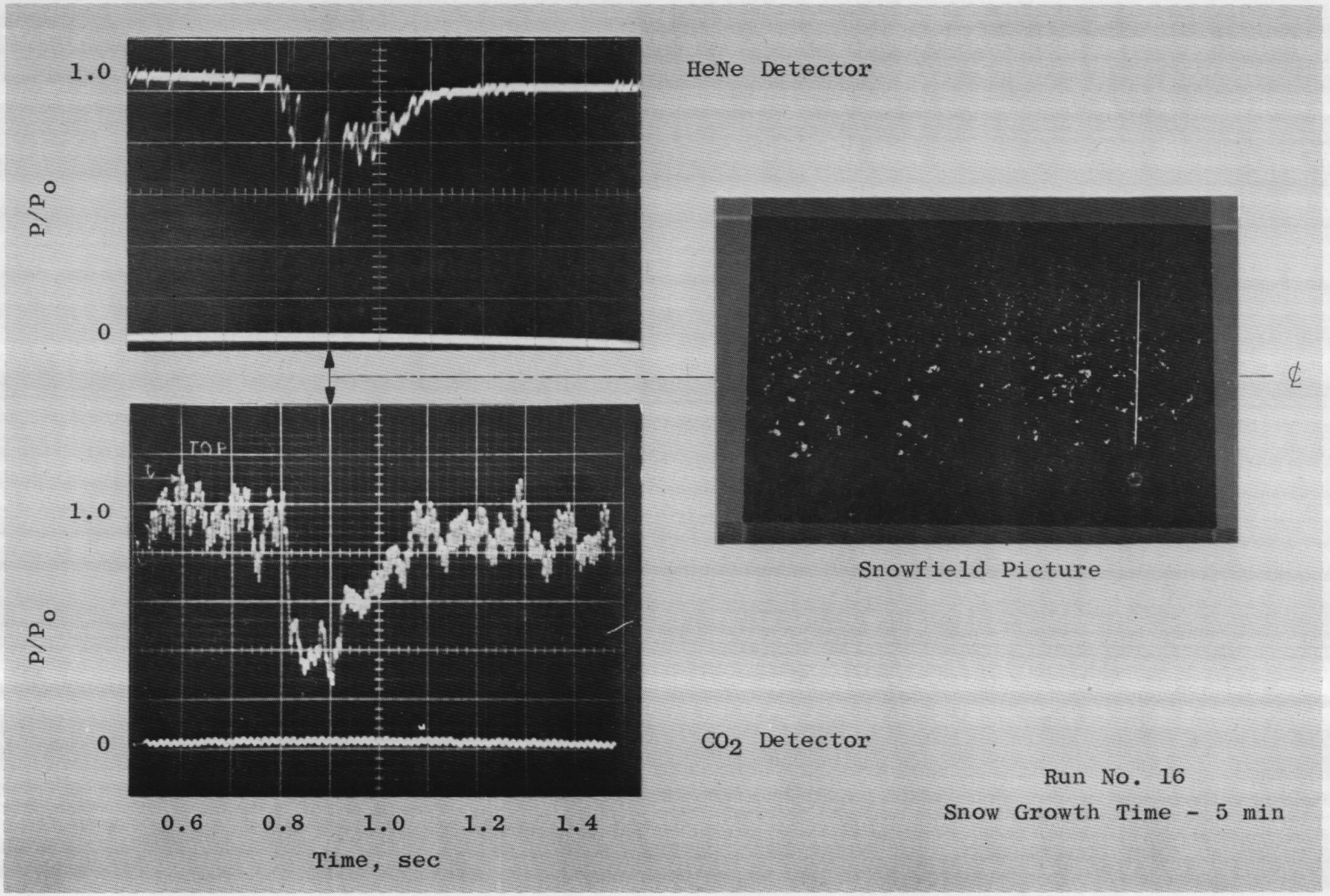
1.0
P/P$_o$
0
HeNe Detector
℄
Snowfield Picture
TOP
1.0
P/P$_o$
0
CO_2 Detector
Run No. 16
Snow Growth Time - 5 min
0.6
0.8
1.0
1.2
1.4
Time, sec

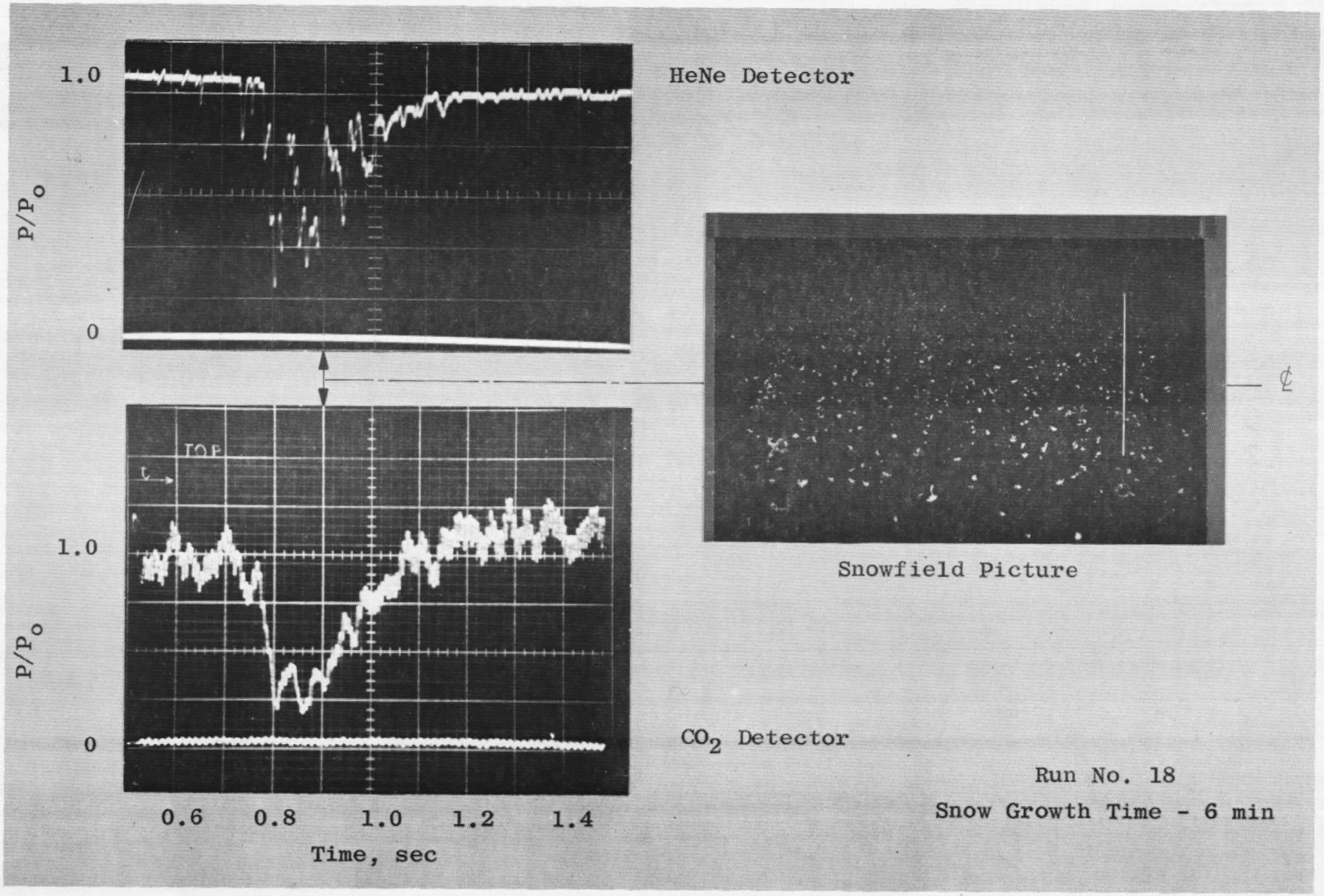
1.0
P/P$_o$
0
HeNe Detector
TOP
1.0
P/P$_o$
0
CO$_2$ Detector
0.6
0.8
1.0
1.2
1.4
Time, sec
Snowfield Picture
℄
Run No. 18
Snow Growth Time - 6 min

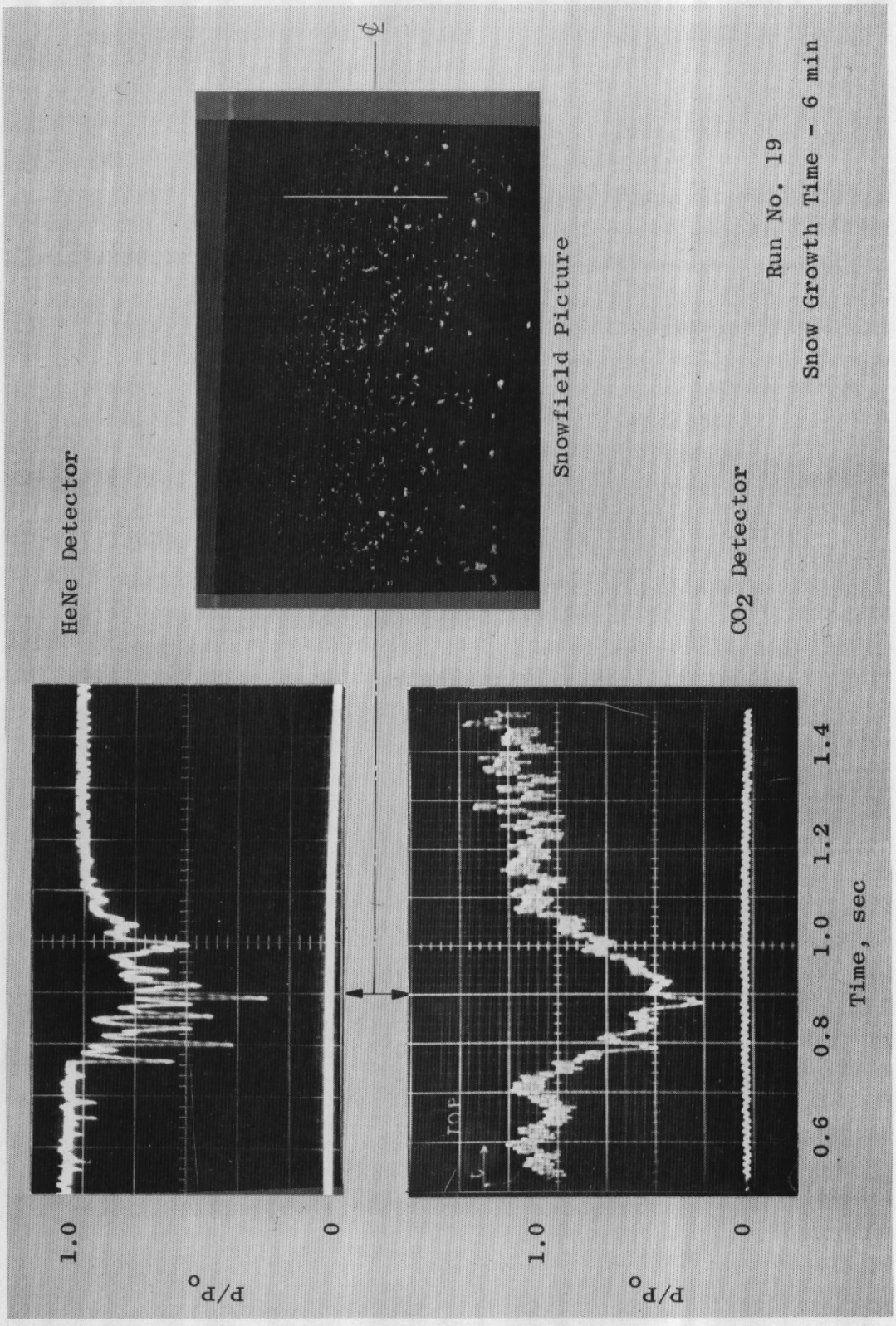
HeNe Detector
Snowfield Picture
CO_2 Detector
Run No. 19
Snow Growth Time - 6 min
1.0
0
P/P$_o$
1.0
0
P/P$_o$
0.6
0.8
1.0
1.2
1.4
Time, sec

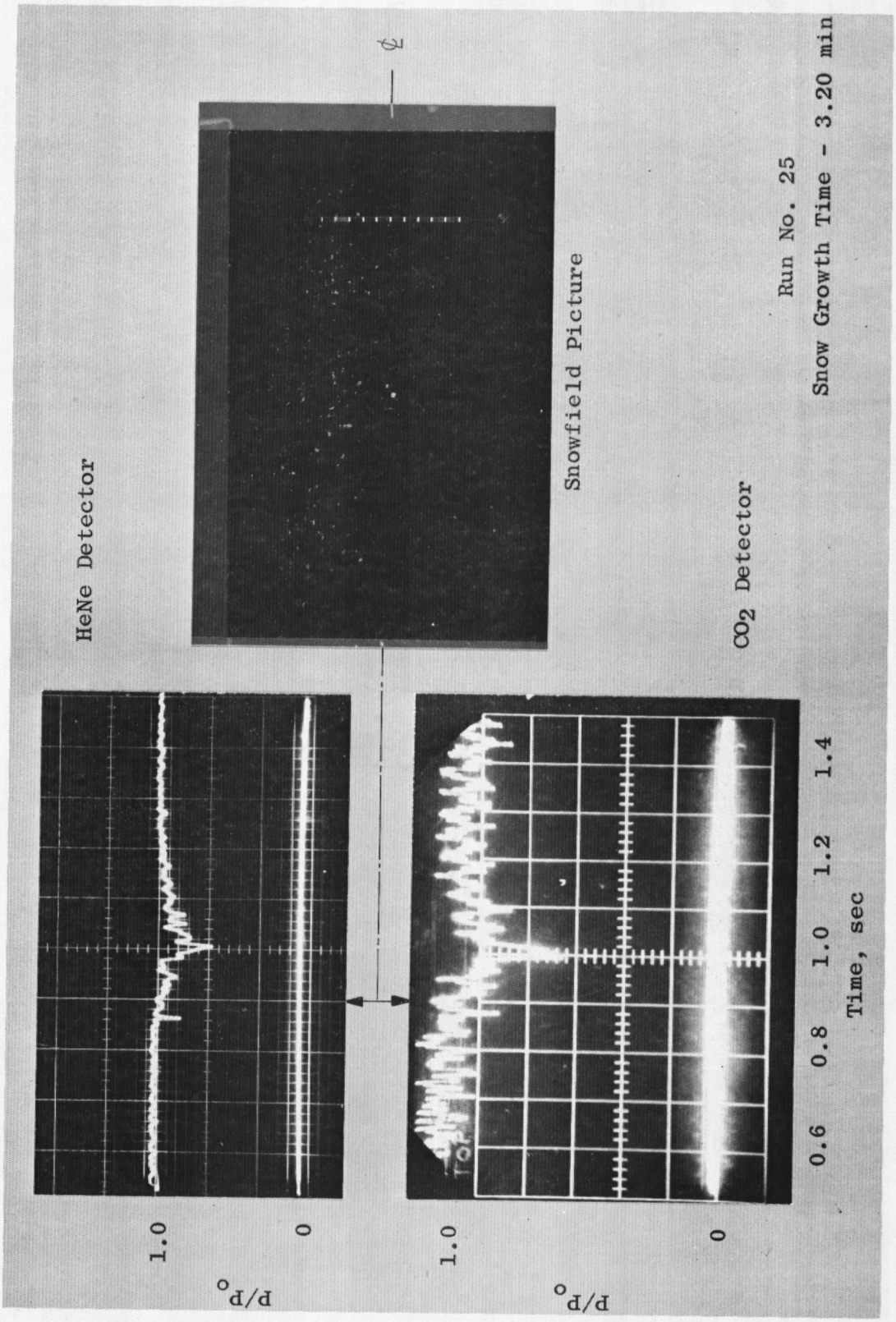
HeNe Detector
Snowfield Picture
CO_2 Detector
Run No. 25
Snow Growth Time - 3.20 min
1.0
0
P/P_o
1.0
0
P/P_o
0.6
0.8
1.0
1.2
1.4
Time, sec

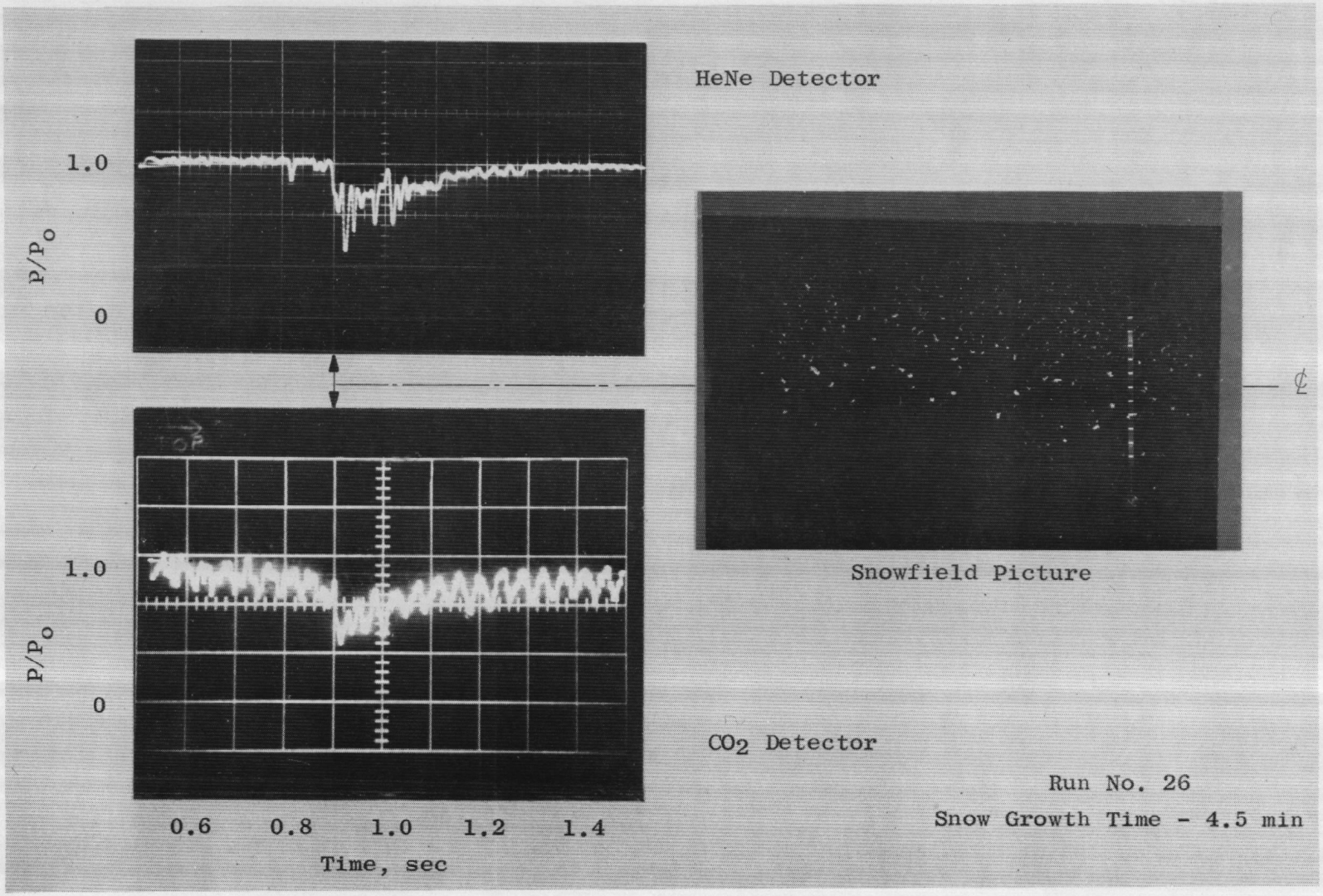
HeNe Detector
1.0
P/P$_o$
0
1.0
P/P$_o$
0
Snowfield Picture
CO_2 Detector
Run No. 26
Snow Growth Time - 4.5 min
0.6
0.8
1.0
1.2
1.4
Time, sec

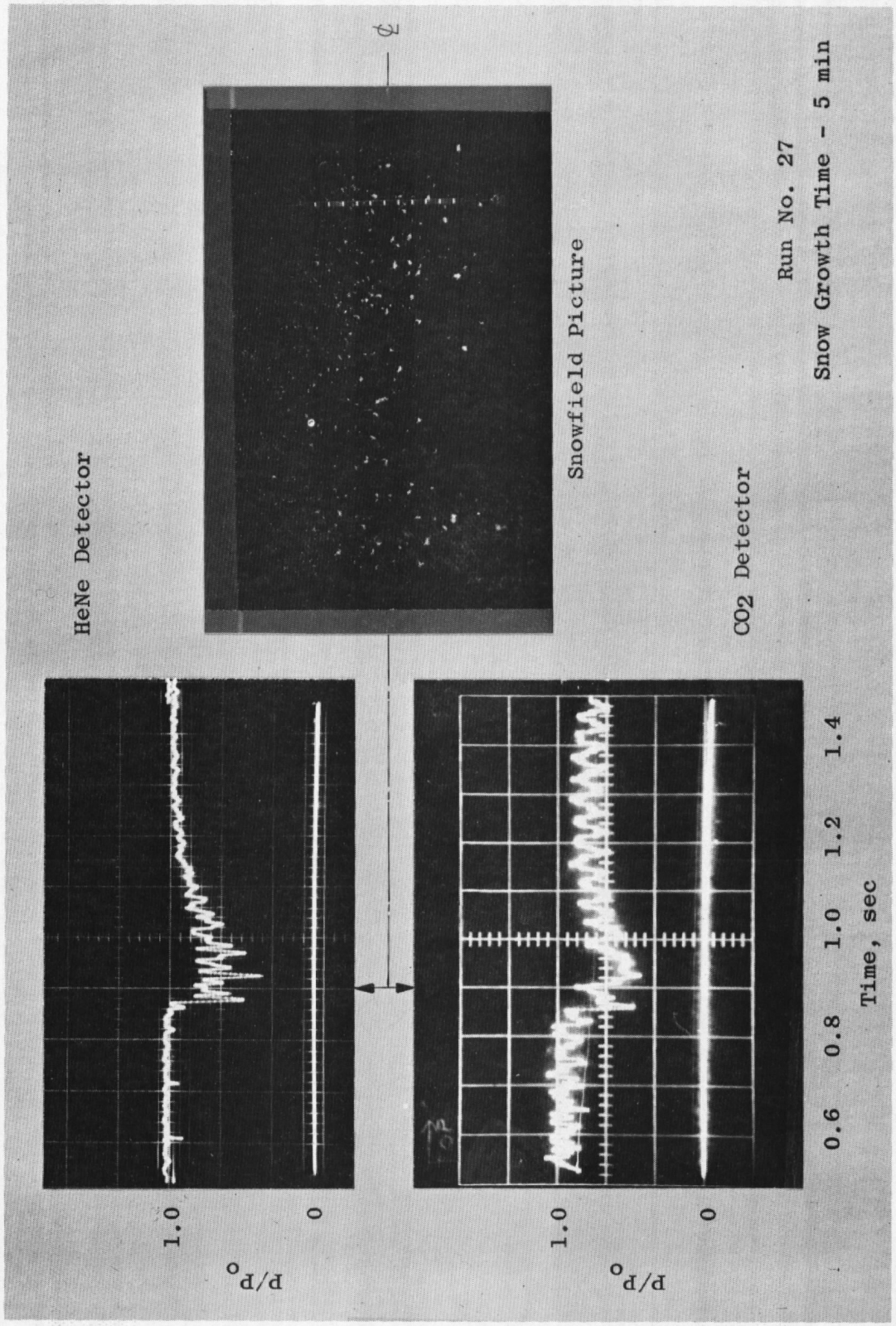
HeNe Detector
Snowfield Picture
CO2 Detector
Run No. 27
Snow Growth Time - 5 min
P/Po
1.0
0
0.6
0.8
1.0
1.2
1.4
Time, sec

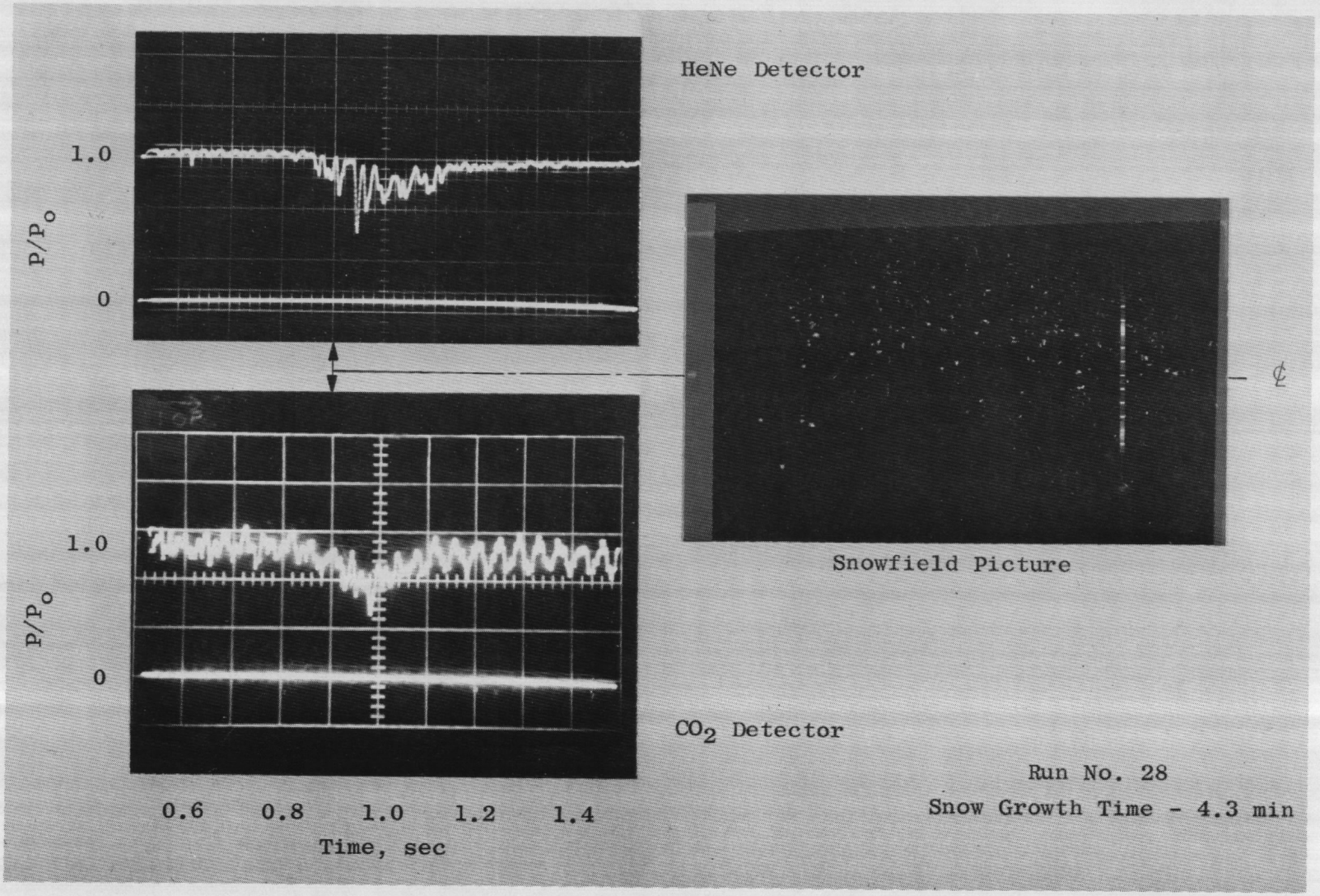
HeNe Detector
1.0
P/P$_o$
0
Snowfield Picture
℄
1.0
P/P$_o$
0
CO$_2$ Detector
Run No. 28
Snow Growth Time - 4.3 min
0.6
0.8
1.0
1.2
1.4
Time, sec

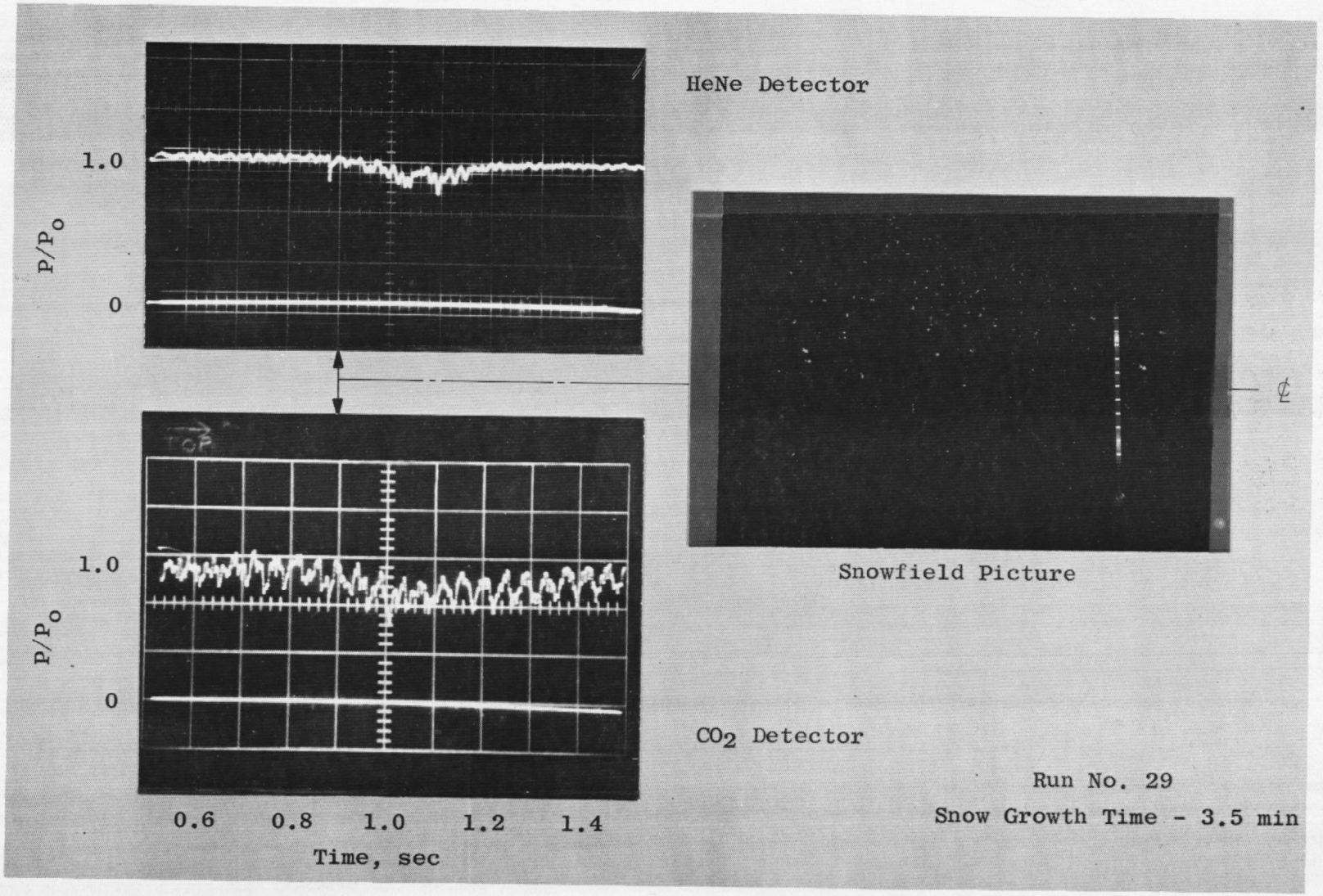
HeNe Detector
1.0
P/P$_o$
0
Snowfield Picture
℄
TOF
1.0
P/P$_o$
0
CO_2 Detector
Run No. 29
Snow Growth Time - 3.5 min
0.6
0.8
1.0
1.2
1.4
Time, sec

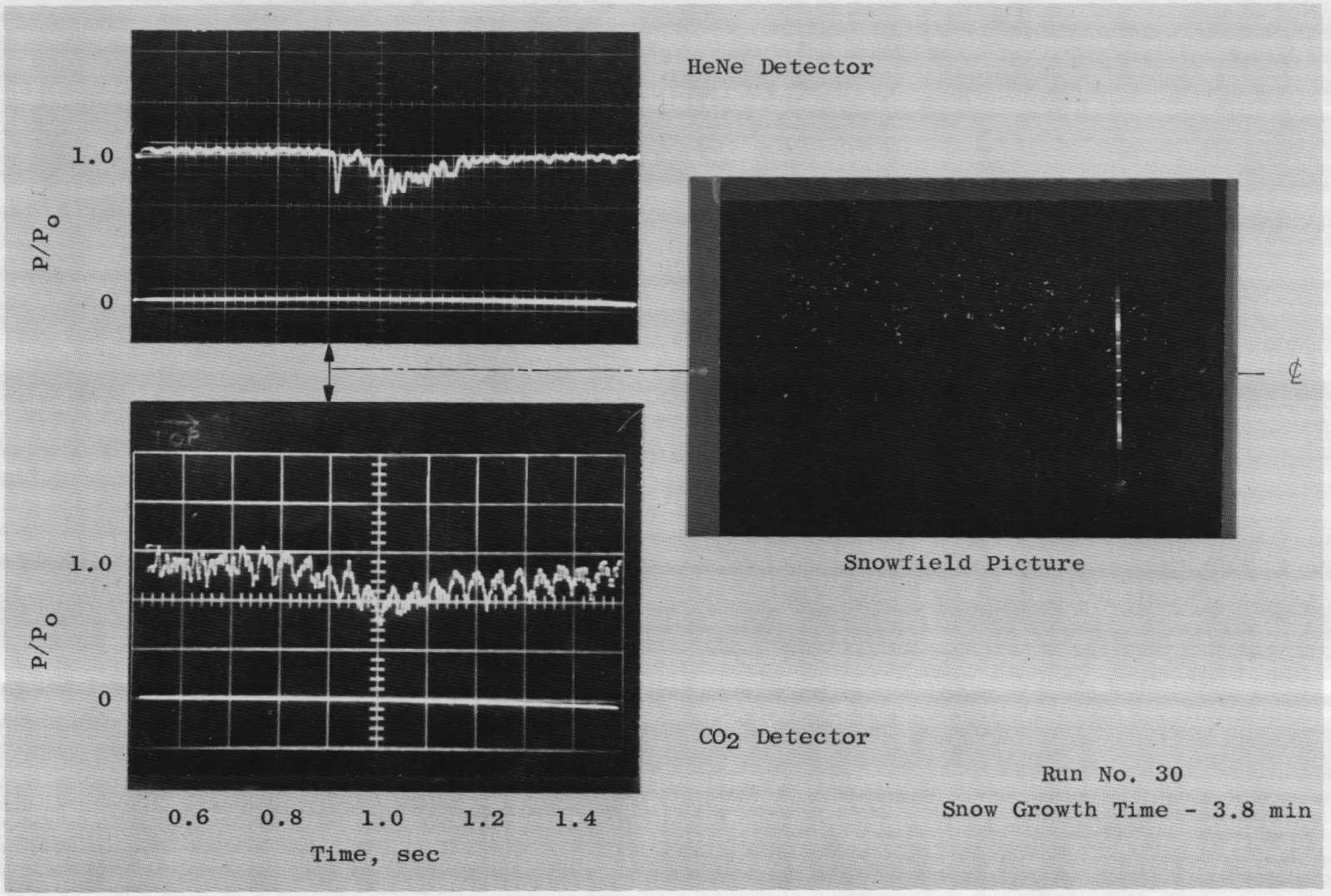
HeNe Detector
1.0
P/P$_o$
0
Snowfield Picture
℄
1.0
P/P$_o$
0
CO_2 Detector
Run No. 30
Snow Growth Time - 3.8 min
0.6
0.8
1.0
1.2
1.4
Time, sec

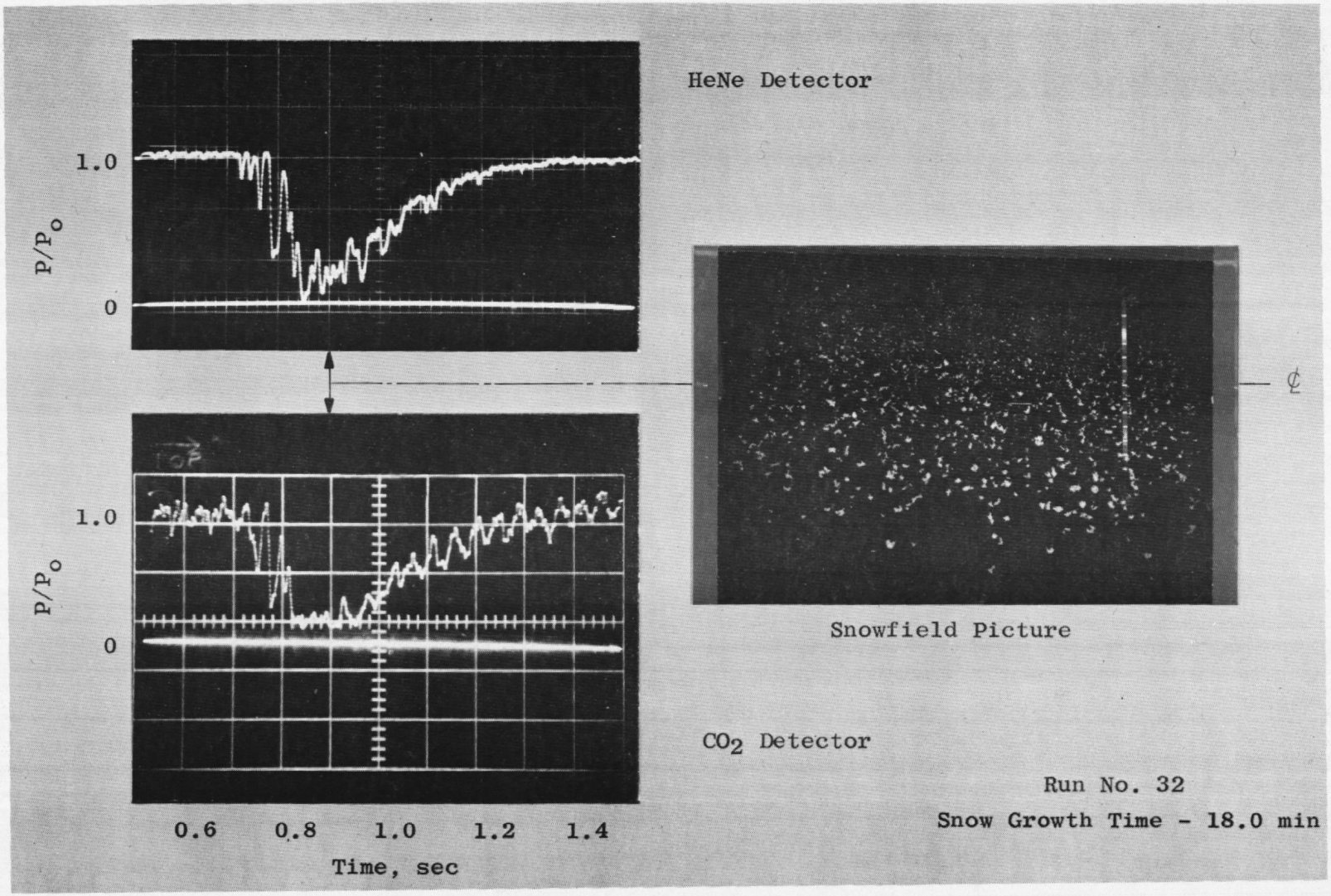
HeNe Detector
1.0
P/P$_o$
0
1.0
P/P$_o$
0
0.6
0.8
1.0
1.2
1.4
Time, sec
Snowfield Picture
CO_2 Detector
Run No. 32
Snow Growth Time - 18.0 min

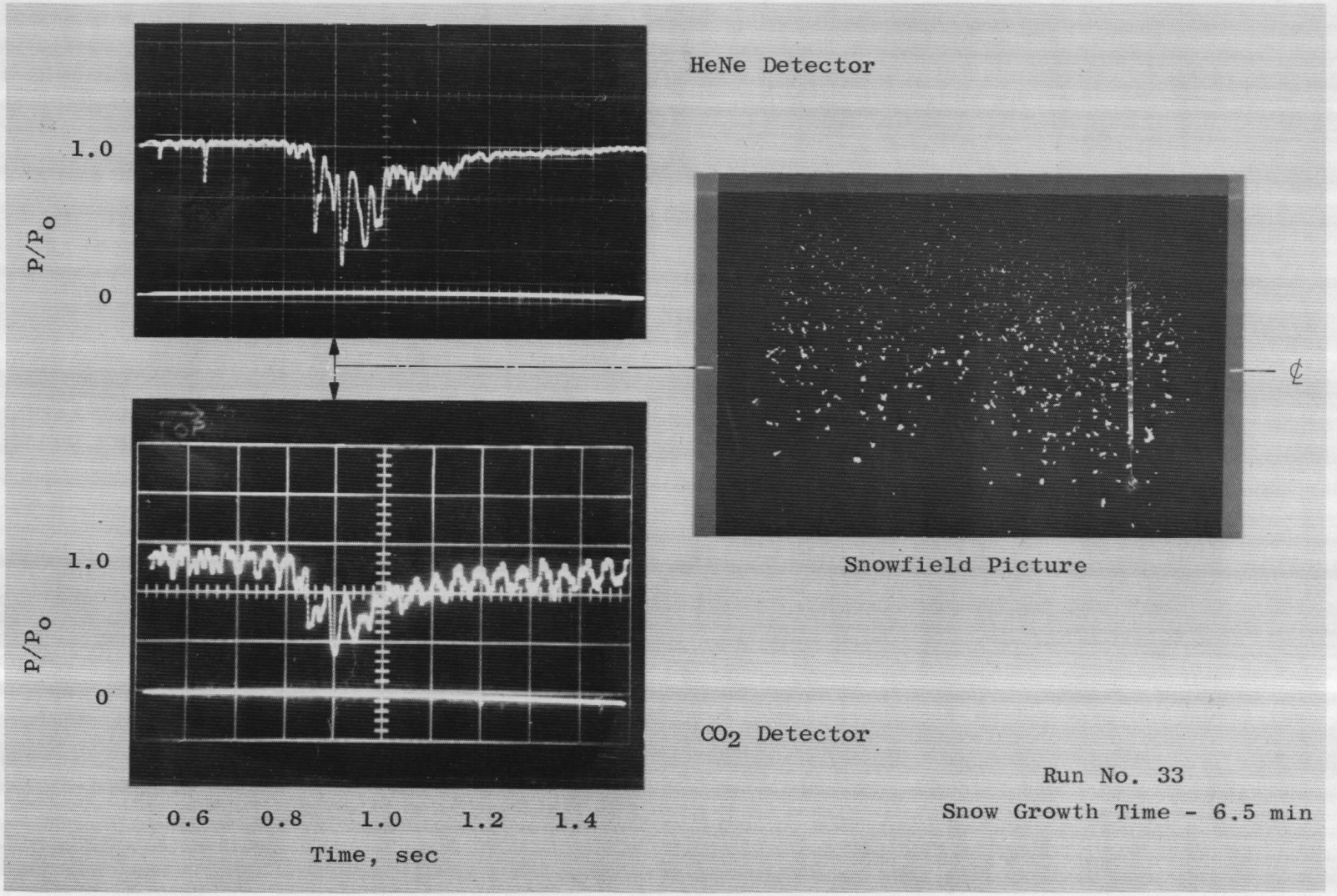
HeNe Detector
1.0
P/P$_o$
0
Snowfield Picture
℄
1.0
P/P$_o$
0
CO_2 Detector
Run No. 33
Snow Growth Time - 6.5 min
0.6
0.8
1.0
1.2
1.4
Time, sec

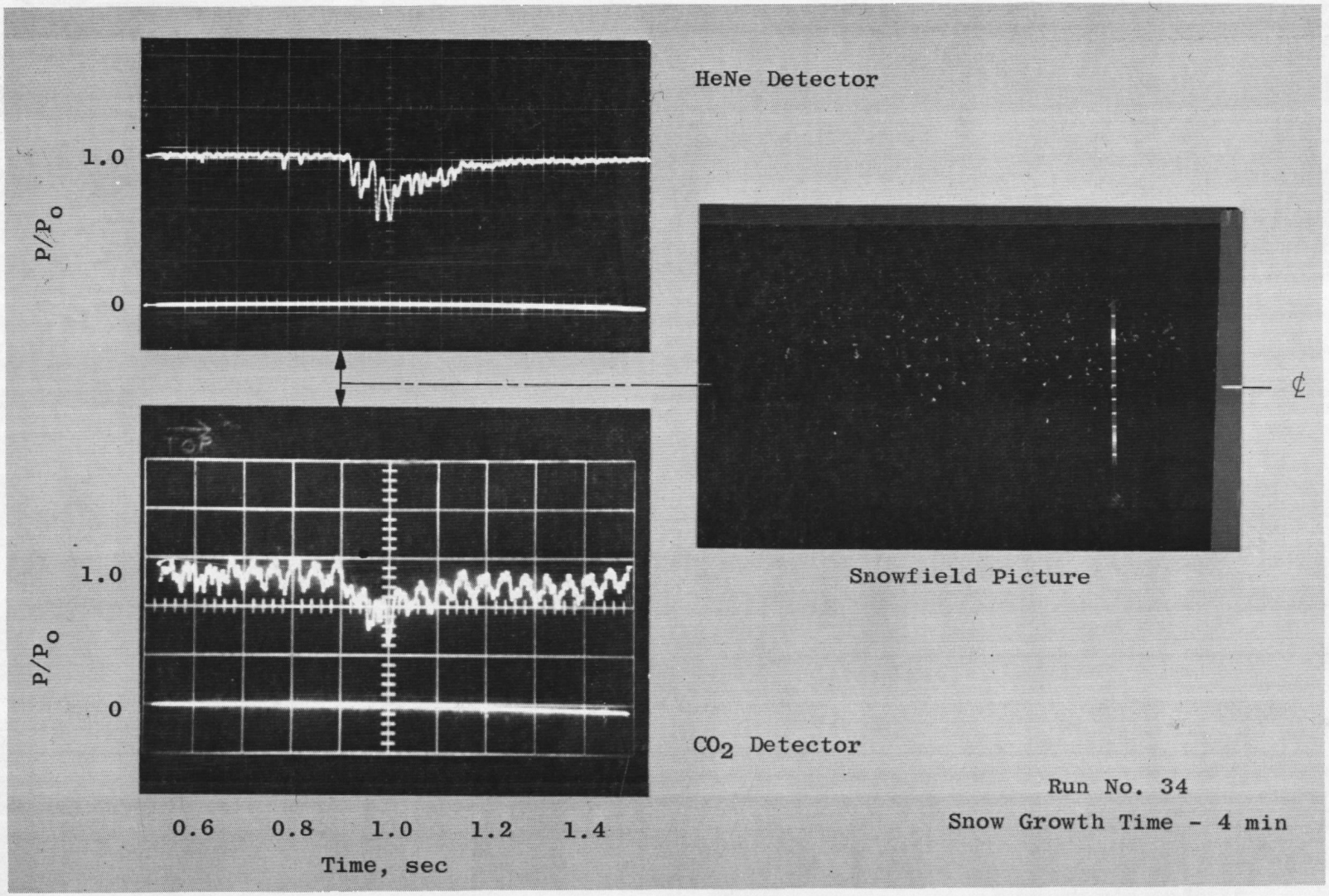
HeNe Detector
1.0
P/P$_o$
0
TOP
1.0
P/P$_o$
0
0.6
0.8
1.0
1.2
1.4
Time, sec
℄
Snowfield Picture
CO$_2$ Detector
Run No. 34
Snow Growth Time - 4 min

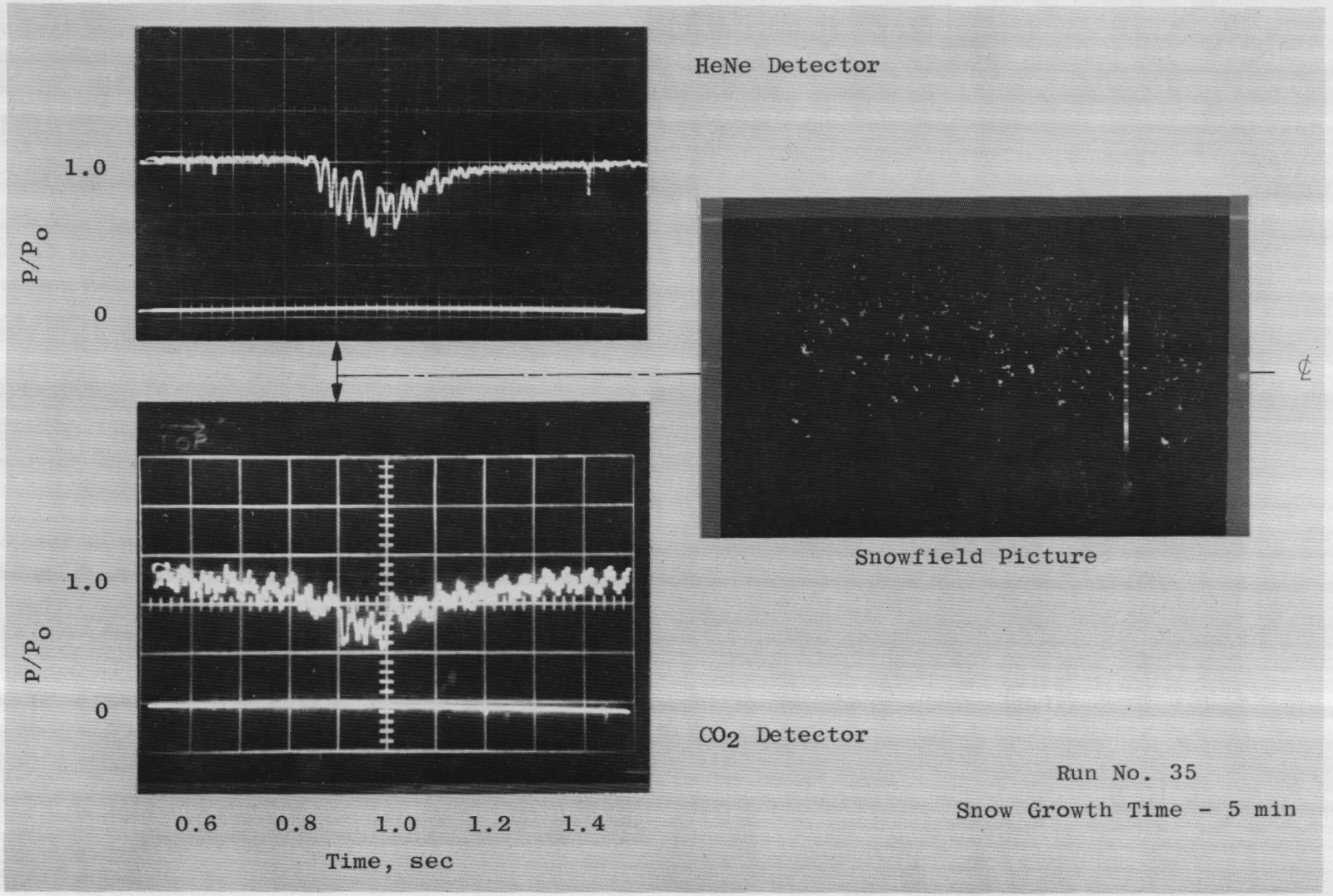
HeNe Detector
1.0
P/P$_o$
0
Snowfield Picture
℄
1.0
P/P$_o$
0
CO_2 Detector
Run No. 35
Snow Growth Time - 5 min
0.6
0.8
1.0
1.2
1.4
Time, sec

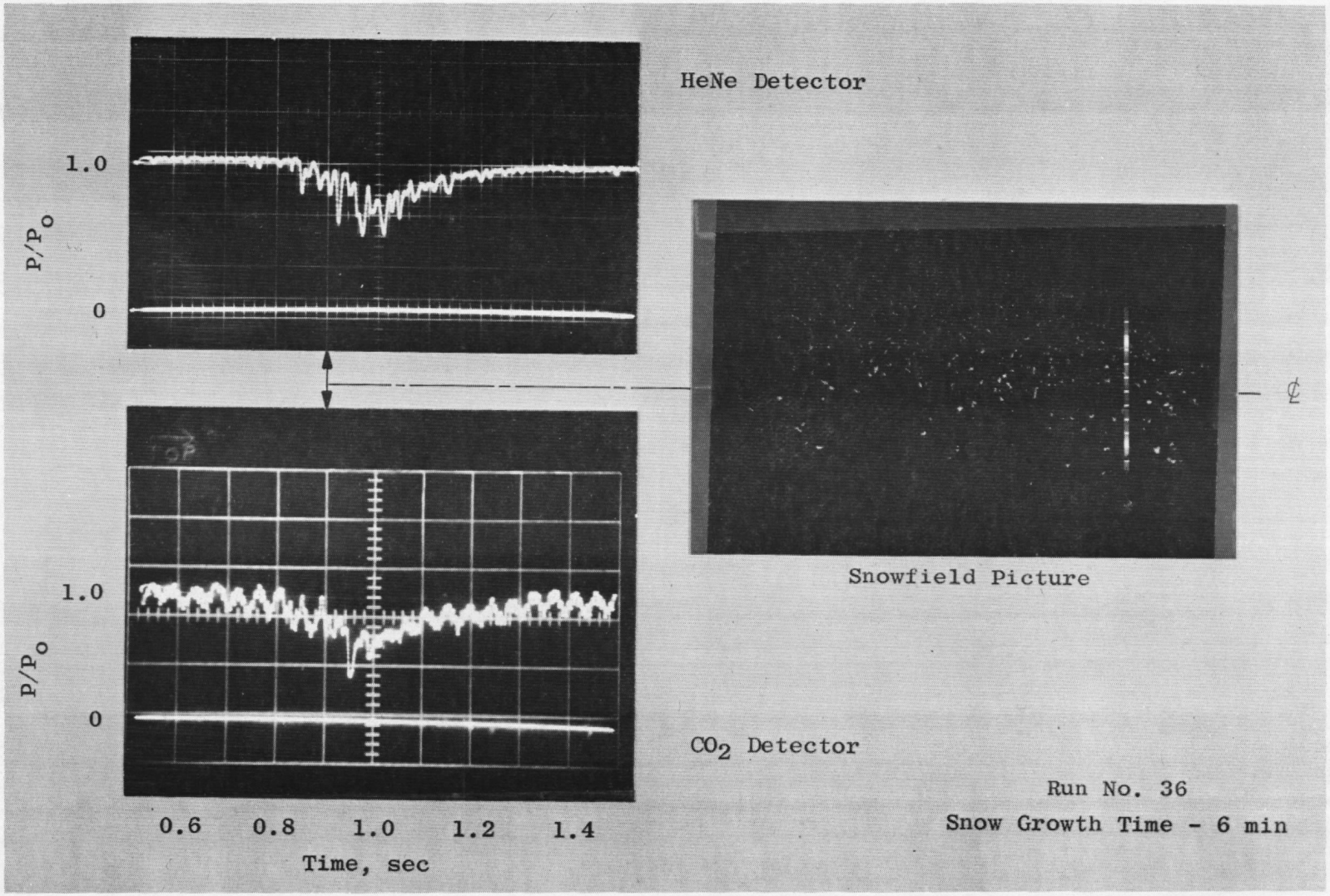
HeNe Detector
1.0
P/P$_o$
0
Snowfield Picture
1.0
P/P$_o$
0
CO_2 Detector
0.6
0.8
1.0
1.2
1.4
Time, sec
Run No. 36
Snow Growth Time - 6 min

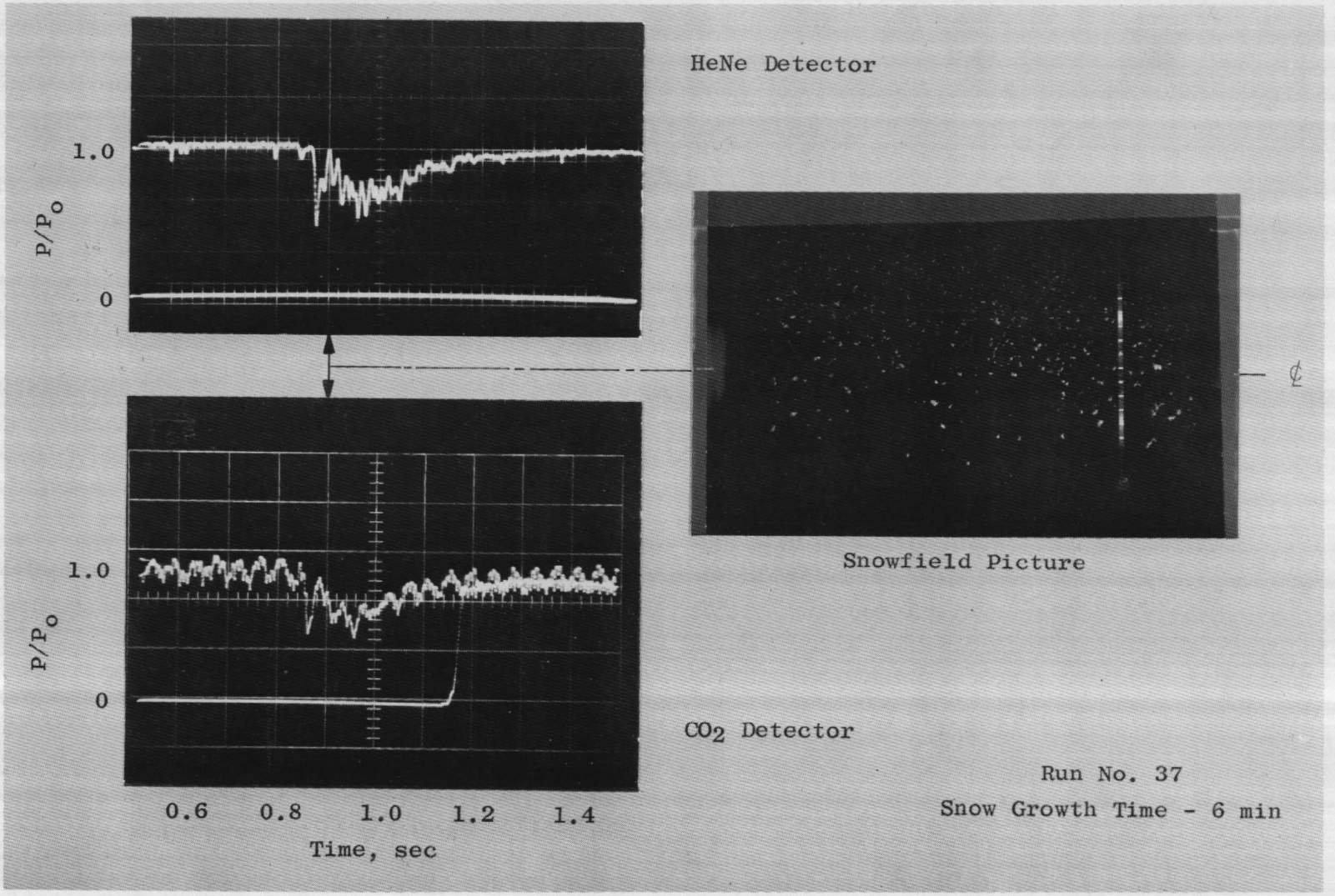
HeNe Detector
1.0
P/P$_o$
0
Snowfield Picture
1.0
P/P$_o$
0
CO_2 Detector
0.6
0.8
1.0
1.2
1.4
Time, sec
Run No. 37
Snow Growth Time - 6 min

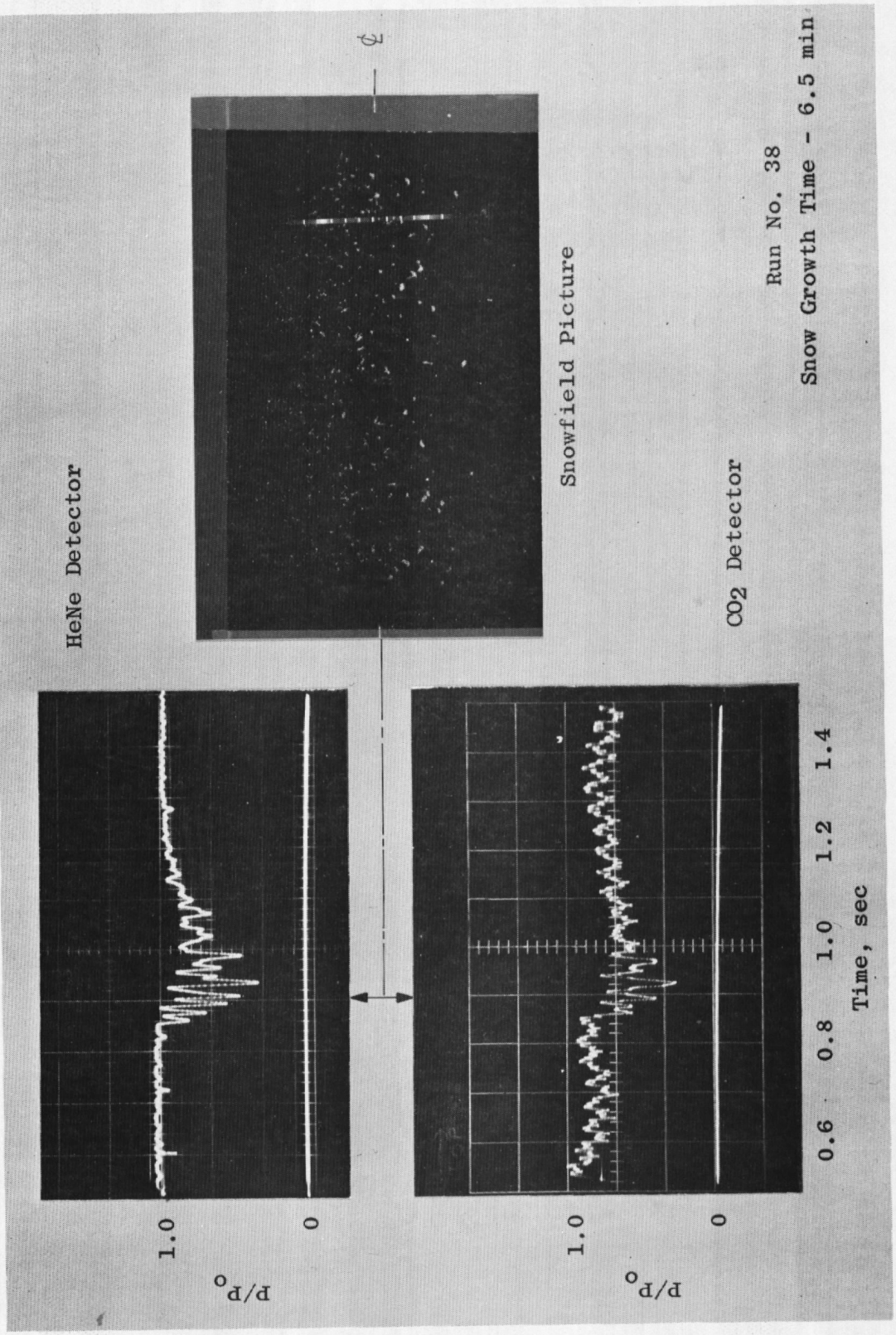
HeNe Detector
Snowfield Picture
CO_2 Detector
Run No. 38
Snow Growth Time - 6.5 min
1.0
0
P/P_o
0.6
0.8
1.0
1.2
1.4
Time, sec

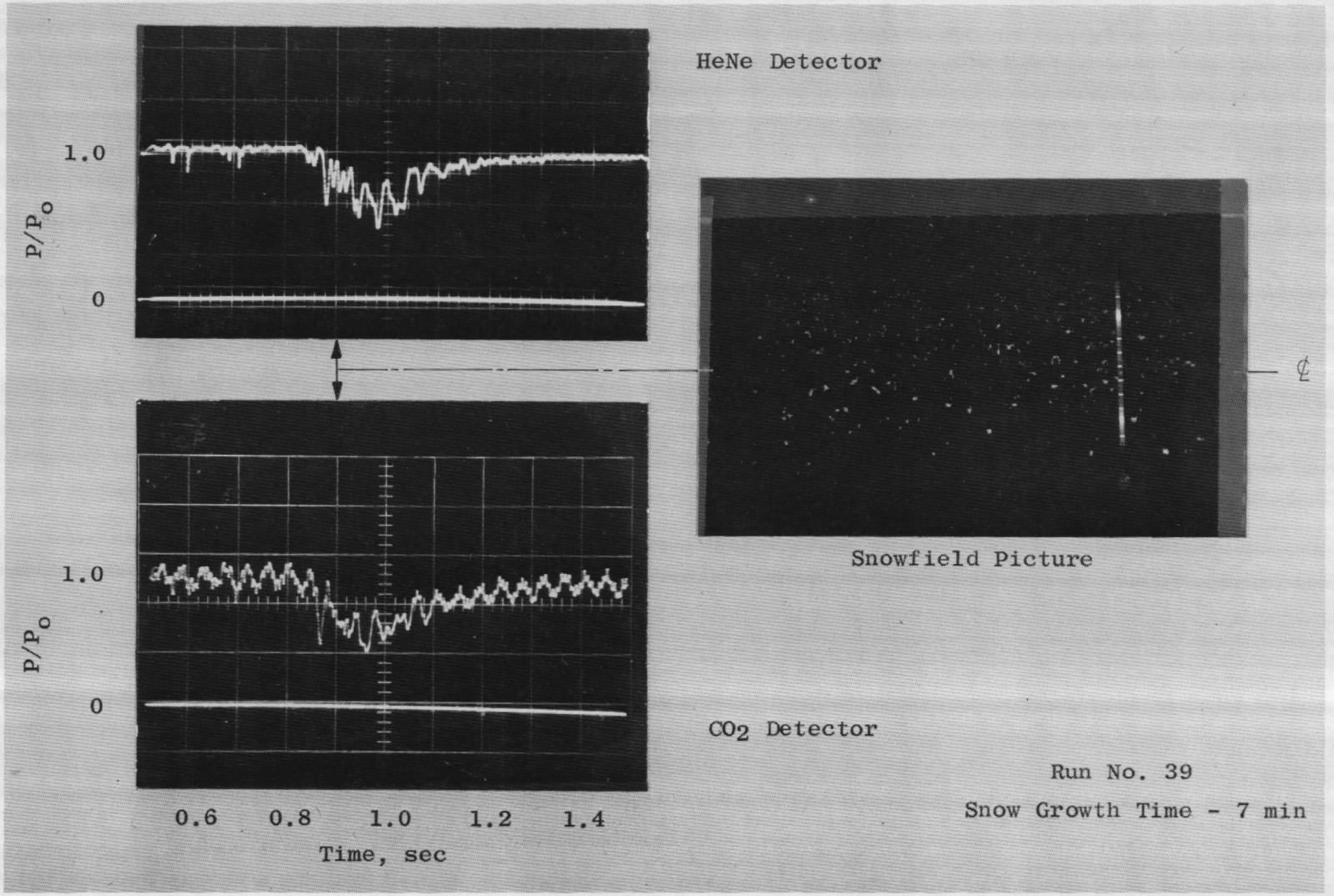
HeNe Detector
1.0
P/P$_o$
0
Snowfield Picture
℄
1.0
P/P$_o$
0
CO$_2$ Detector
Run No. 39
Snow Growth Time - 7 min
0.6
0.8
1.0
1.2
1.4
Time, sec

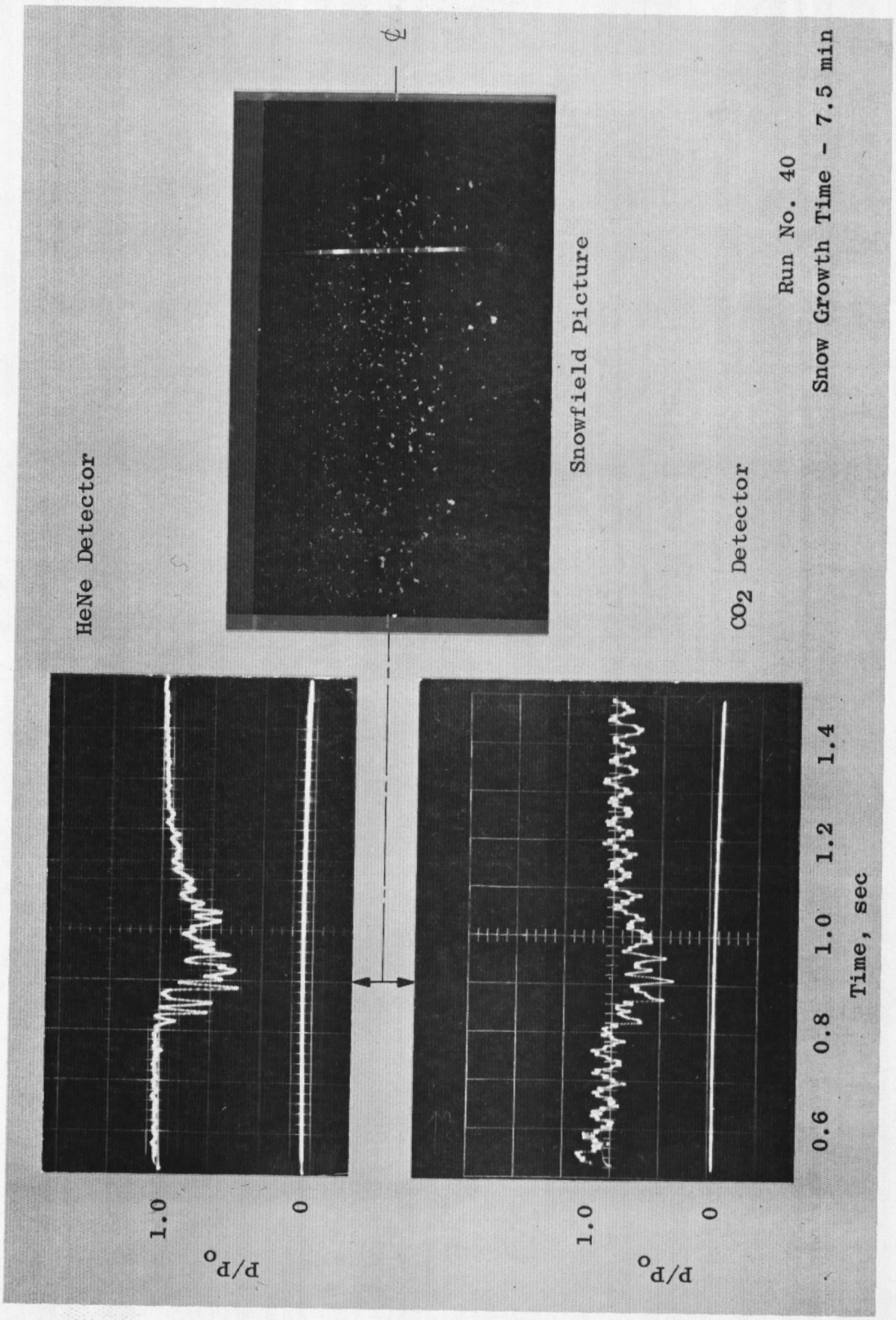
HeNe Detector
Snowfield Picture
CO_2 Detector
Run No. 40
Snow Growth Time - 7.5 min
1.0
0
P/P_o
0.6
0.8
1.0
1.2
1.4
Time, sec

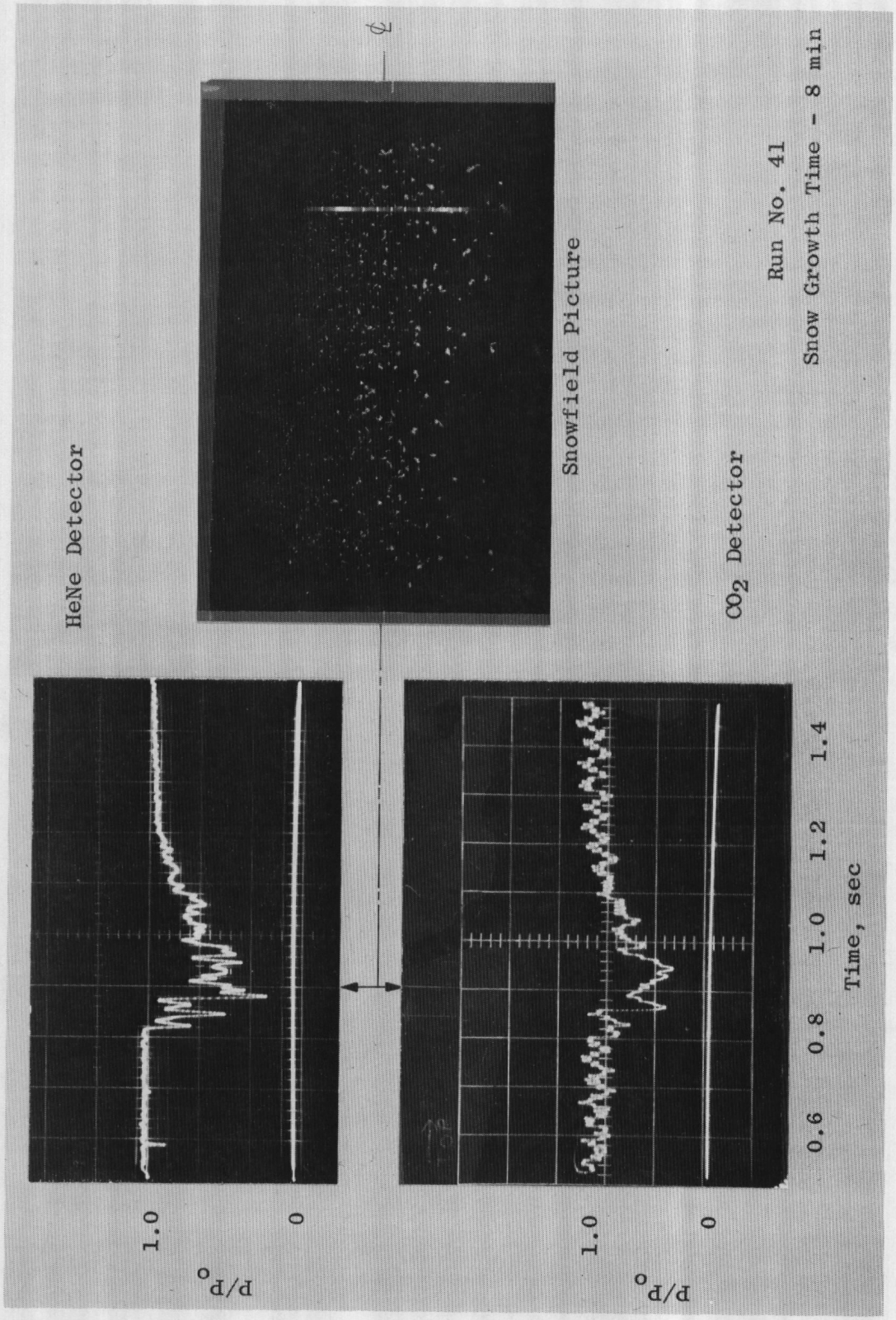
HeNe Detector
Snowfield Picture
CO_2 Detector
Run No. 41
Snow Growth Time - 8 min
1.0
0
P/P_o
1.0
0
P/P_o
0.6
0.8
1.0
1.2
1.4
Time, sec

HeNe Detector
1.0
P/Po
0
Snowfield Picture
℄
1.0
P/Po
0
CO2 Detector
Run No. 42
Snow Growth Time - 10 min
0.6
0.8
1.0
1.2
1.4
Time, sec

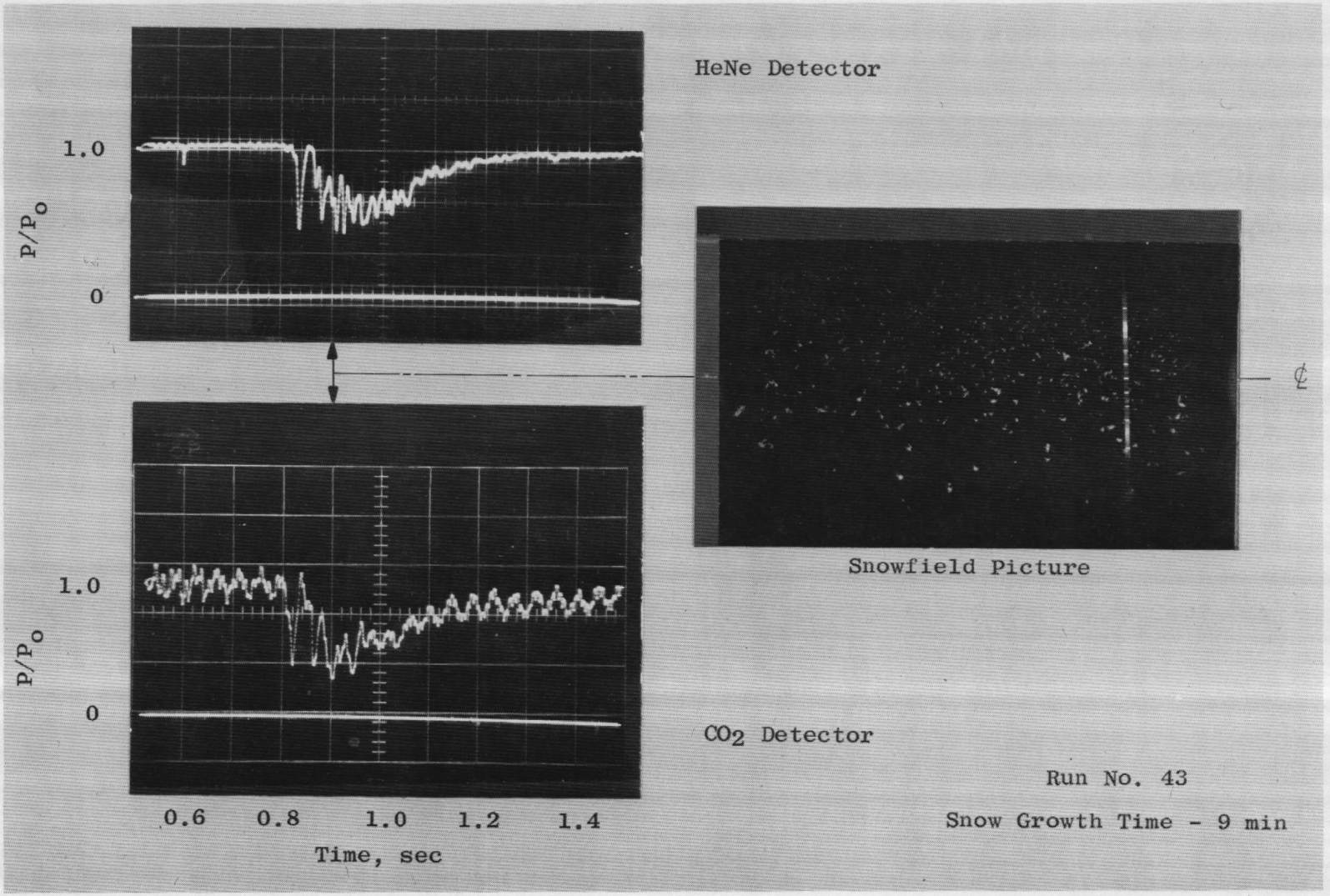
HeNe Detector
1.0
P/P$_o$
0
Snowfield Picture
℄
1.0
P/P$_o$
0
CO_2 Detector
Run No. 43
Snow Growth Time - 9 min
0.6
0.8
1.0
1.2
1.4
Time, sec

APPENDIX B
COMPARISON OF EXPERIMENTAL AND THEORETICAL RESULTS

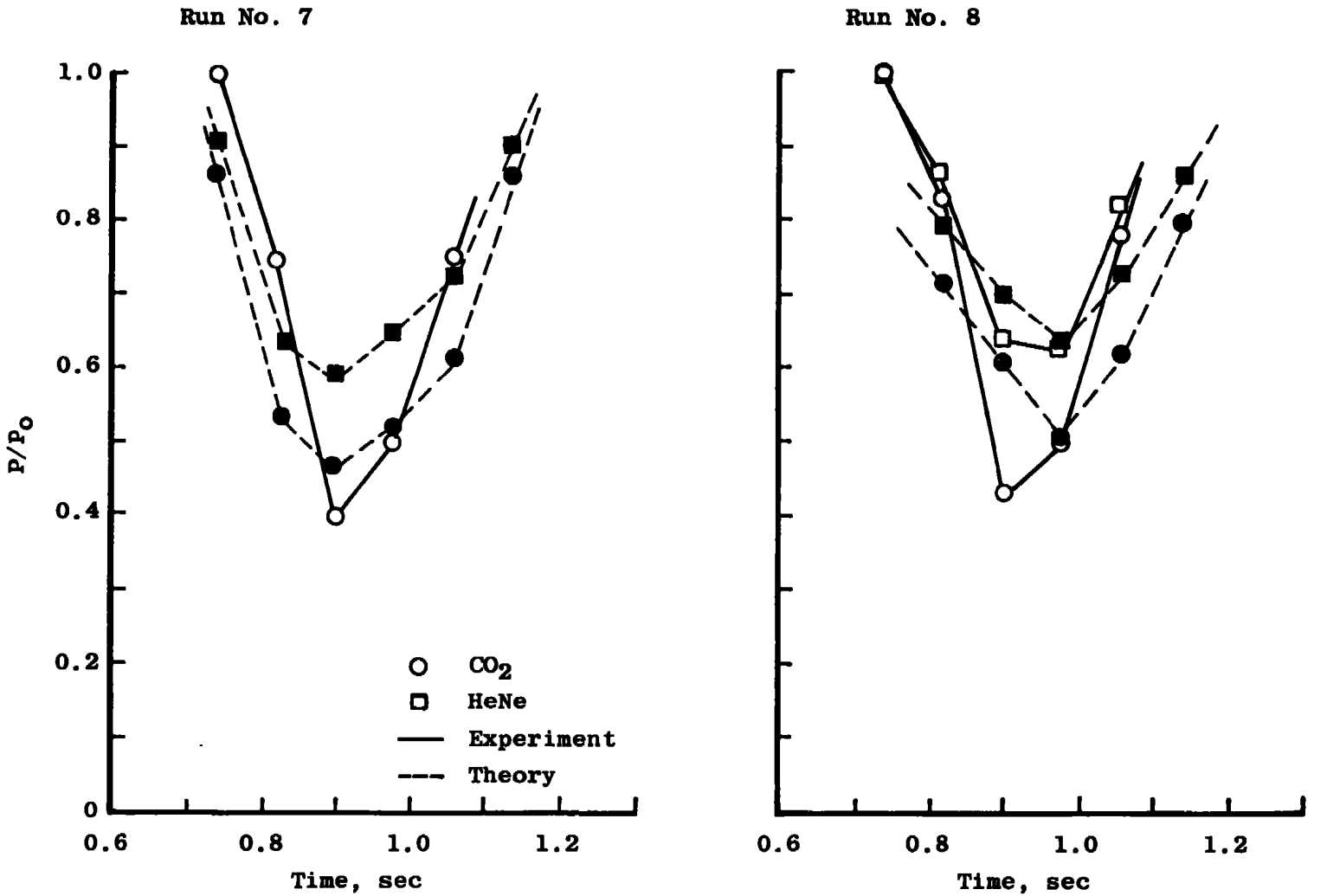
Run No. 7
Run No. 8
1.0
0.8
0.6
0.4
0.2
0
P/P$_o$
0.6
0.8
1.0
1.2
Time, sec
CO$_2$
HeNe
Experiment
Theory

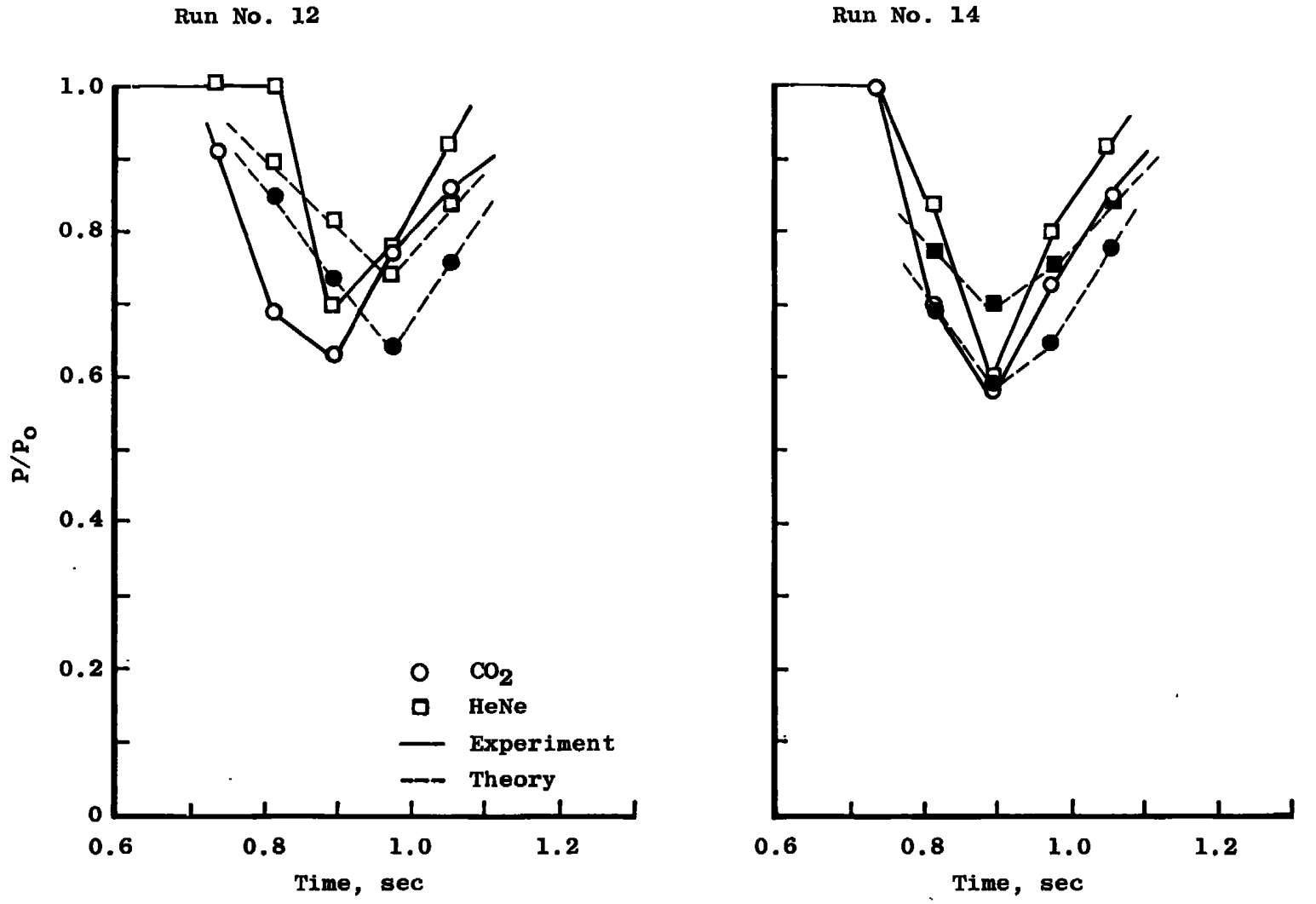
Run No. 12
Run No. 14
1.0
0.8
0.6
0.4
0.2
0
P/P$_o$
0.6
0.8
1.0
1.2
Time, sec
CO$_2$
HeNe
Experiment
Theory

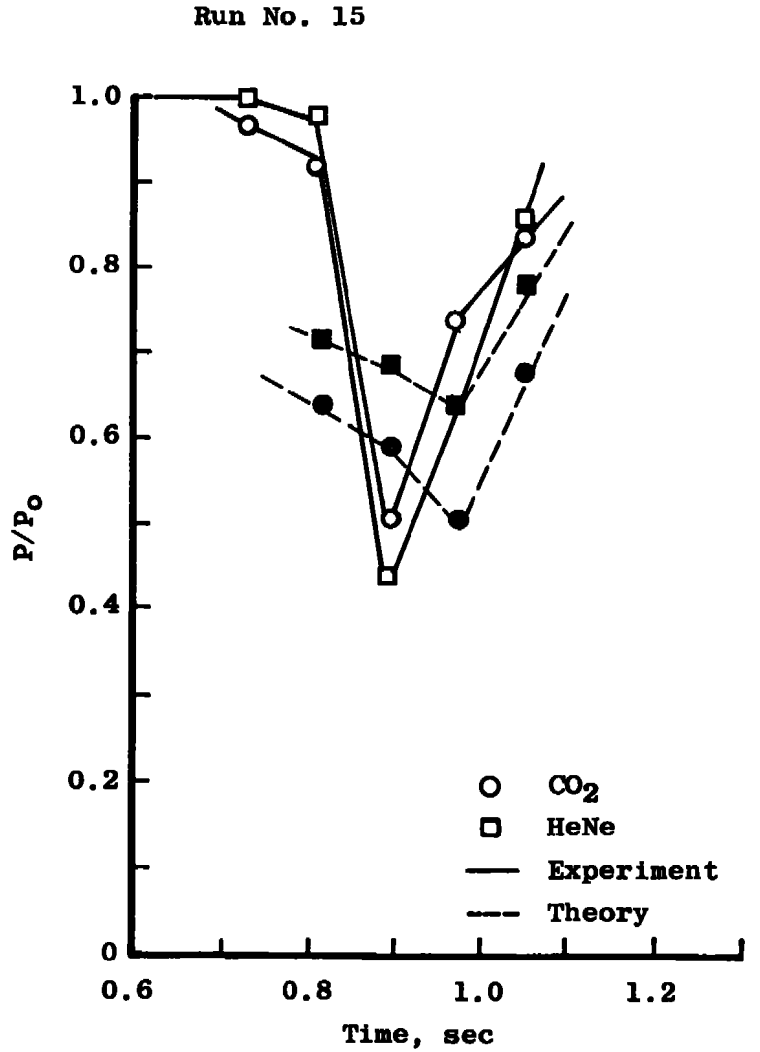
Run No. 15
1.0
0.8
0.6
0.4
0.2
0
P/P$_o$
0.6
0.8
1.0
1.2
Time, sec
CO$_2$
HeNe
Experiment
Theory

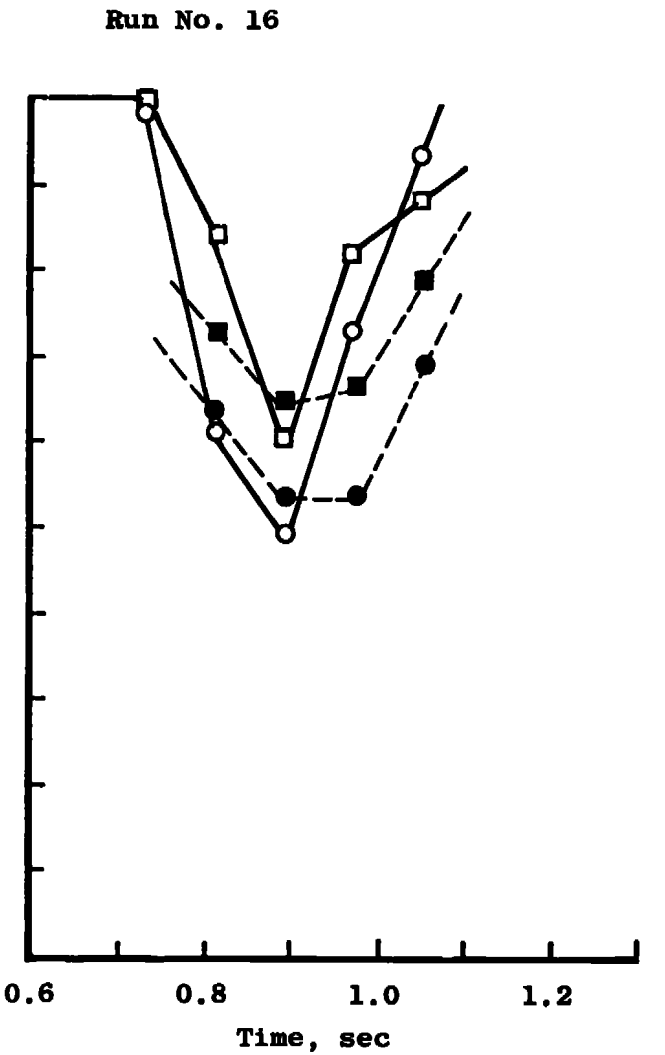
Run No. 16
0.6
0.8
1.0
1.2
Time, sec

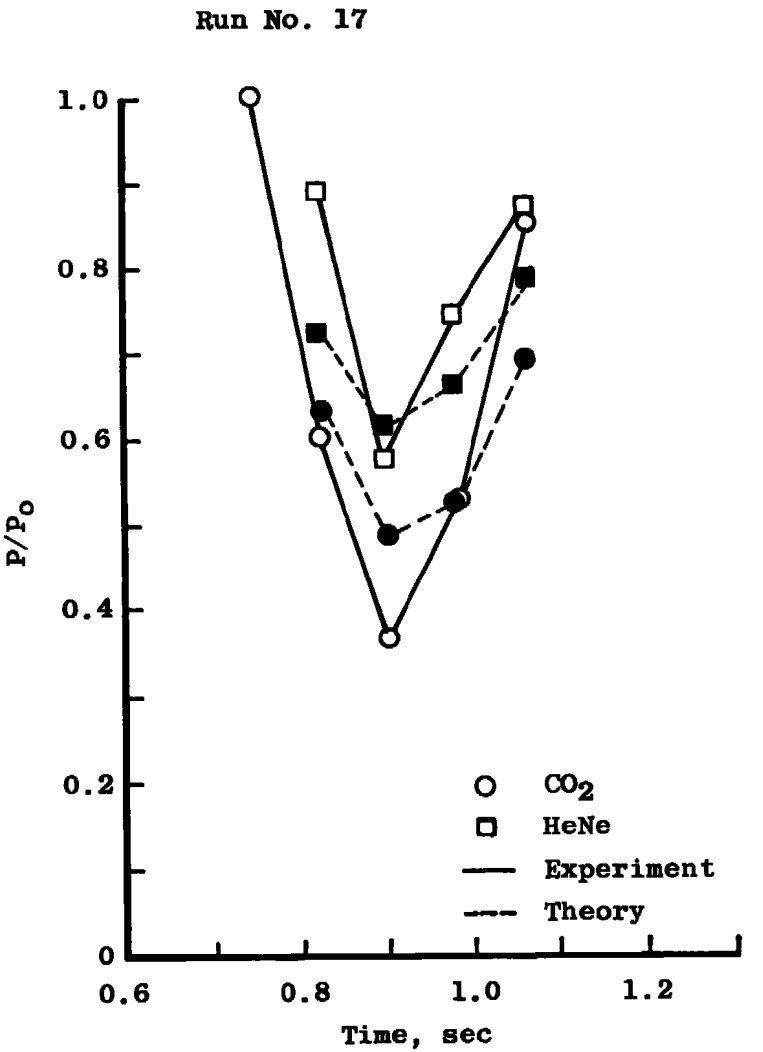
Run No. 17
1.0
0.8
0.6
0.4
0.2
0
P/P$_o$
0.6
0.8
1.0
1.2
Time, sec
CO$_2$
HeNe
Experiment
Theory

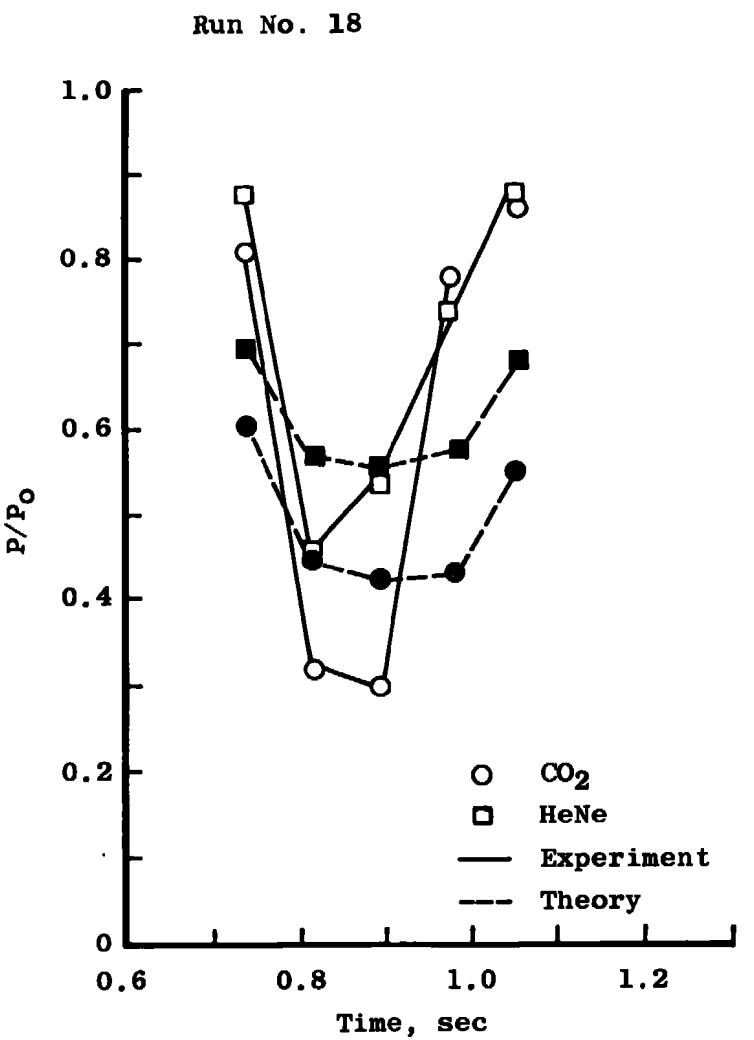
Run No. 18
1.0
0.8
0.6
0.4
0.2
0
P/P$_o$
CO$_2$
HeNe
Experiment
Theory
0.6
0.8
1.0
1.2
Time, sec

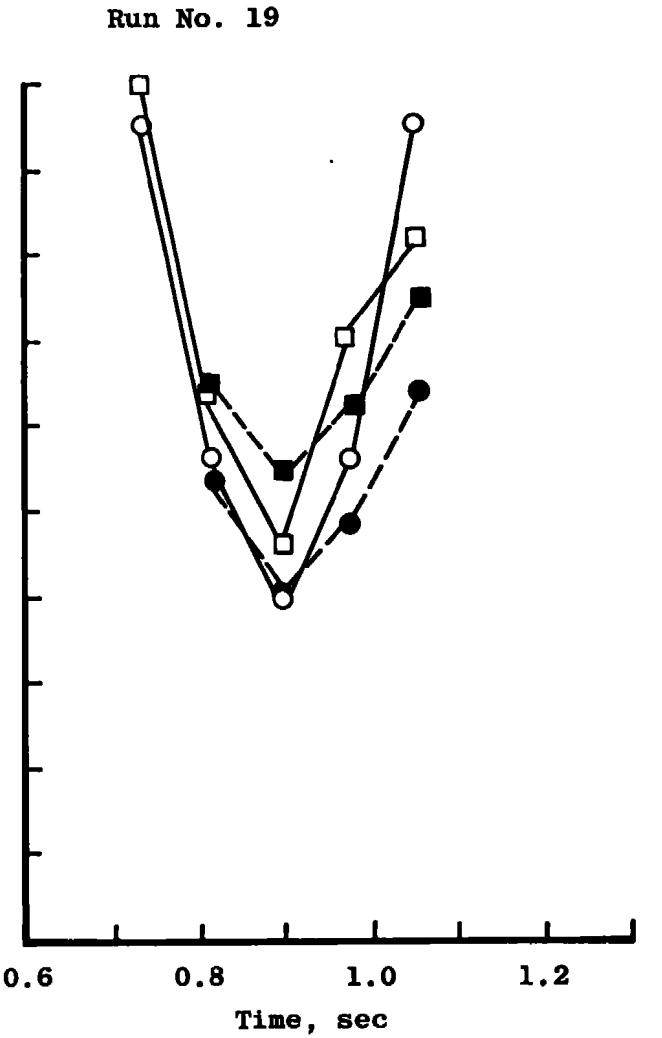
Run No. 19
0.6
0.8
1.0
1.2
Time, sec

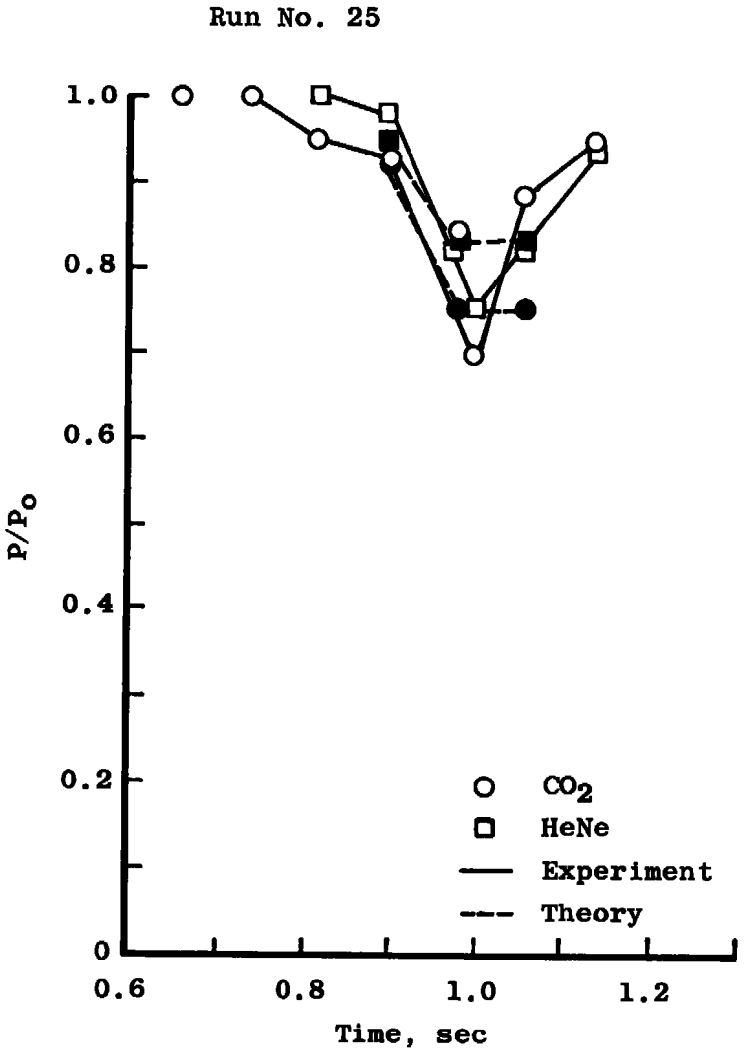
Run No. 25
1.0
0.8
0.6
0.4
0.2
0
P/P$_o$
CO$_2$
HeNe
Experiment
Theory
0.6
0.8
1.0
1.2
Time, sec

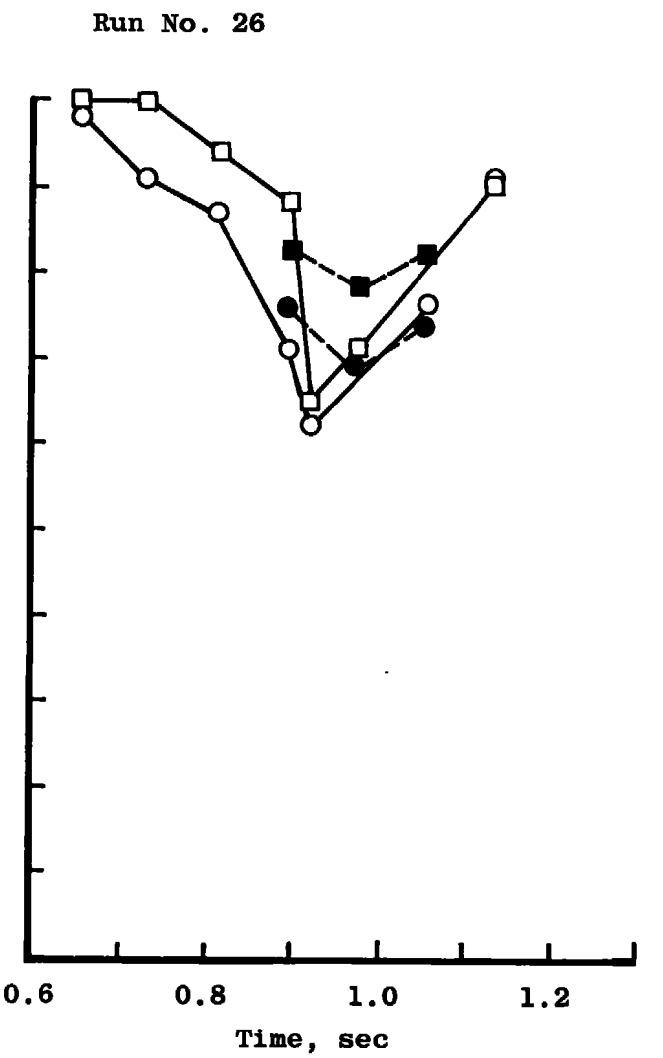
Run No. 26
0.6
0.8
1.0
1.2
Time, sec

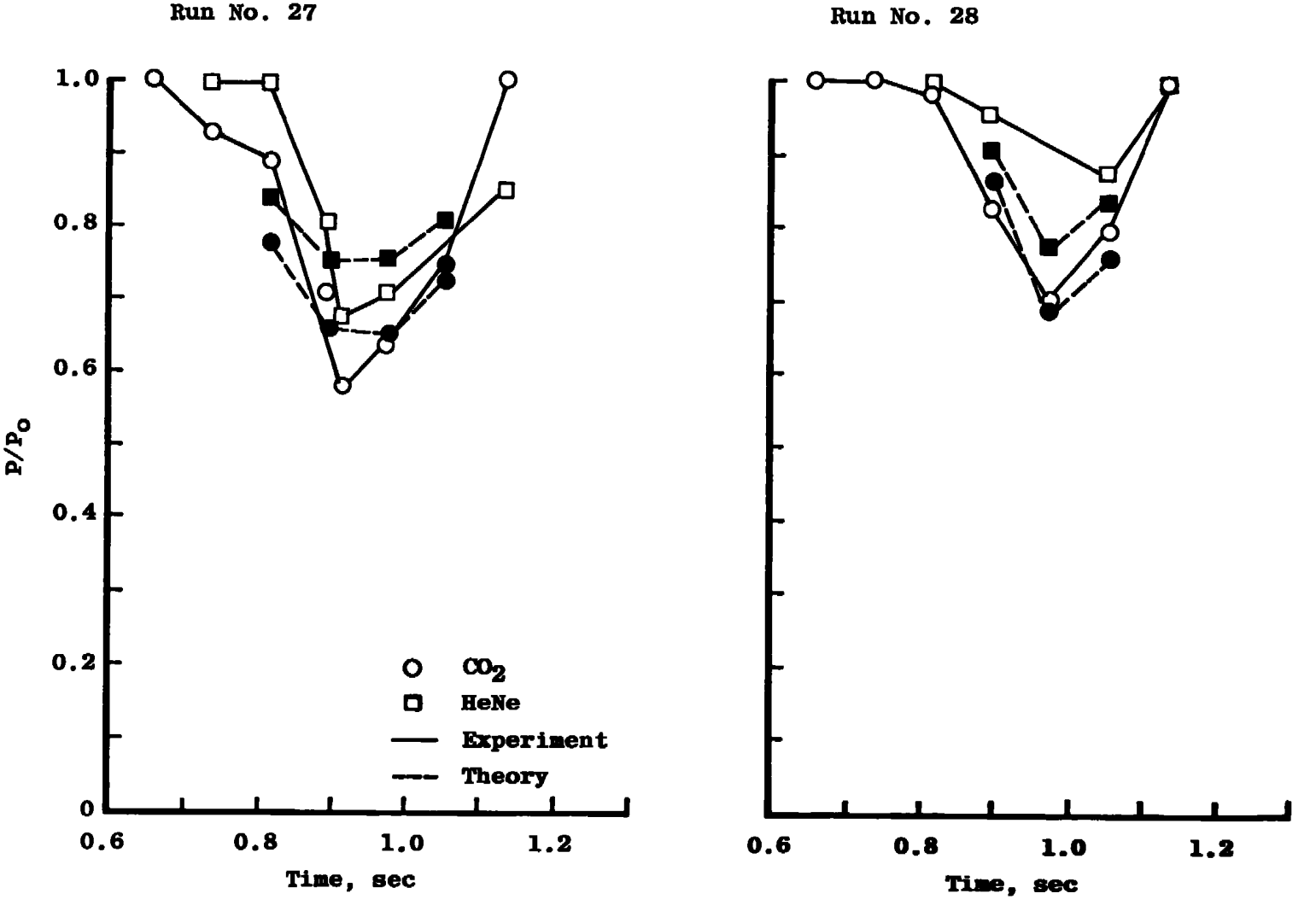
Run No. 27
Run No. 28
1.0
0.8
0.6
0.4
0.2
0
P/P$_o$
0.6
0.8
1.0
1.2
Time, sec
CO$_2$
HeNe
Experiment
Theory

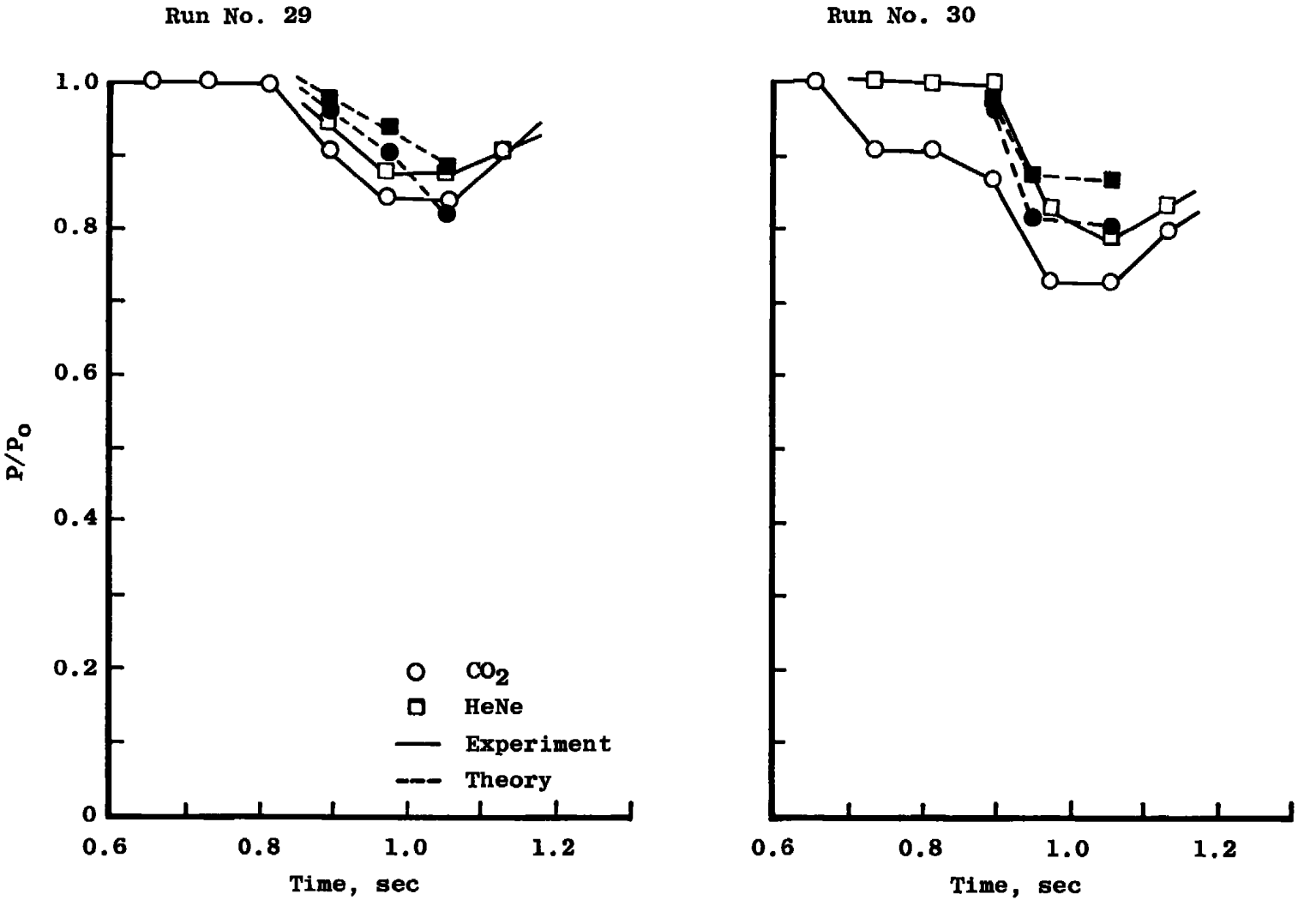
Run No. 29
Run No. 30
1.0
0.8
0.6
0.4
0.2
0
P/P$_o$
0.6
0.8
1.0
1.2
Time, sec
CO$_2$
HeNe
Experiment
Theory

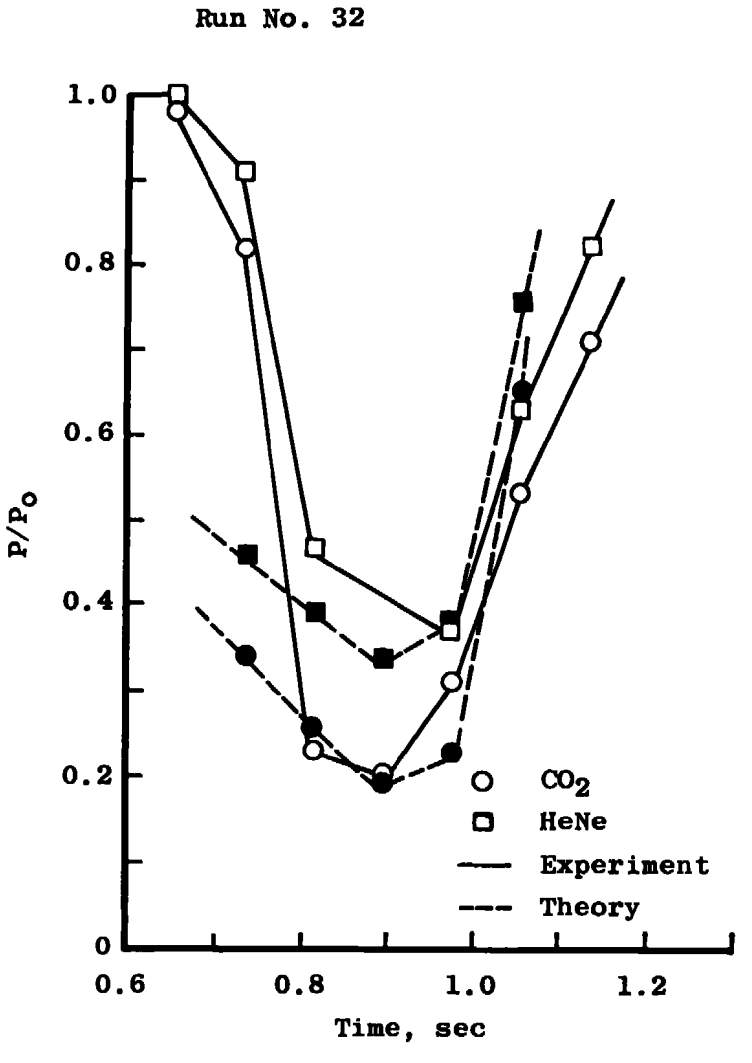
Run No. 32
1.0
0.8
0.6
0.4
0.2
0
P/P$_o$
0.6
0.8
1.0
1.2
Time, sec
CO$_2$
HeNe
Experiment
Theory

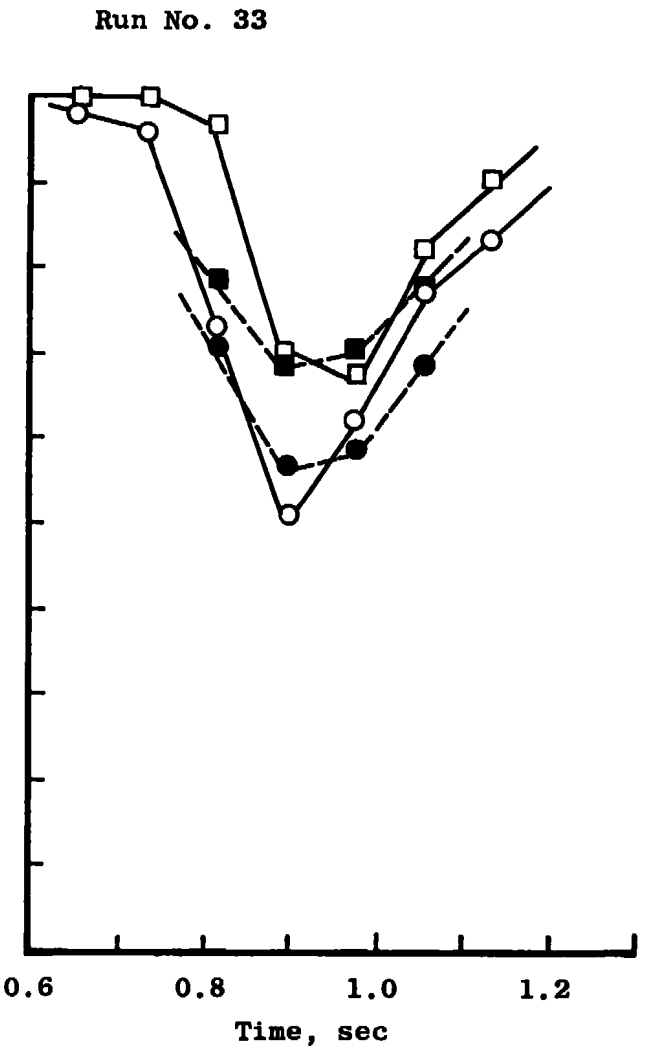
Run No. 33
0.6
0.8
1.0
1.2
Time, sec

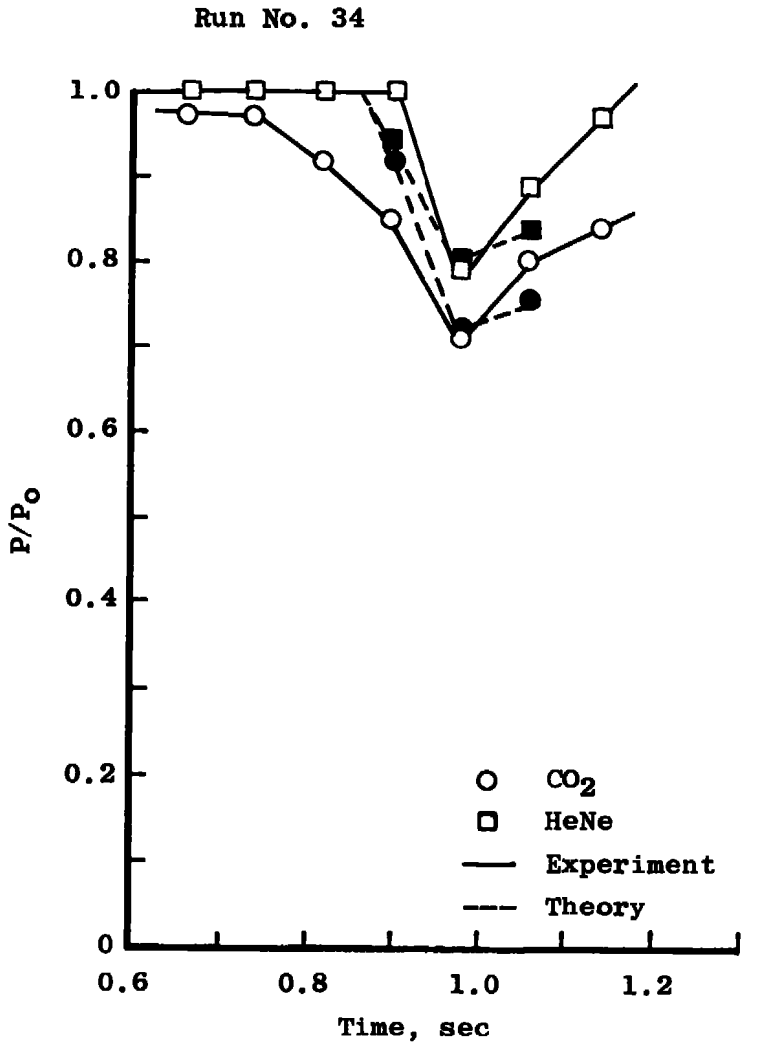
Run No. 34
1.0
0.8
0.6
0.4
0.2
0
P/P$_o$
0.6
0.8
1.0
1.2
Time, sec
CO$_2$
HeNe
Experiment
Theory

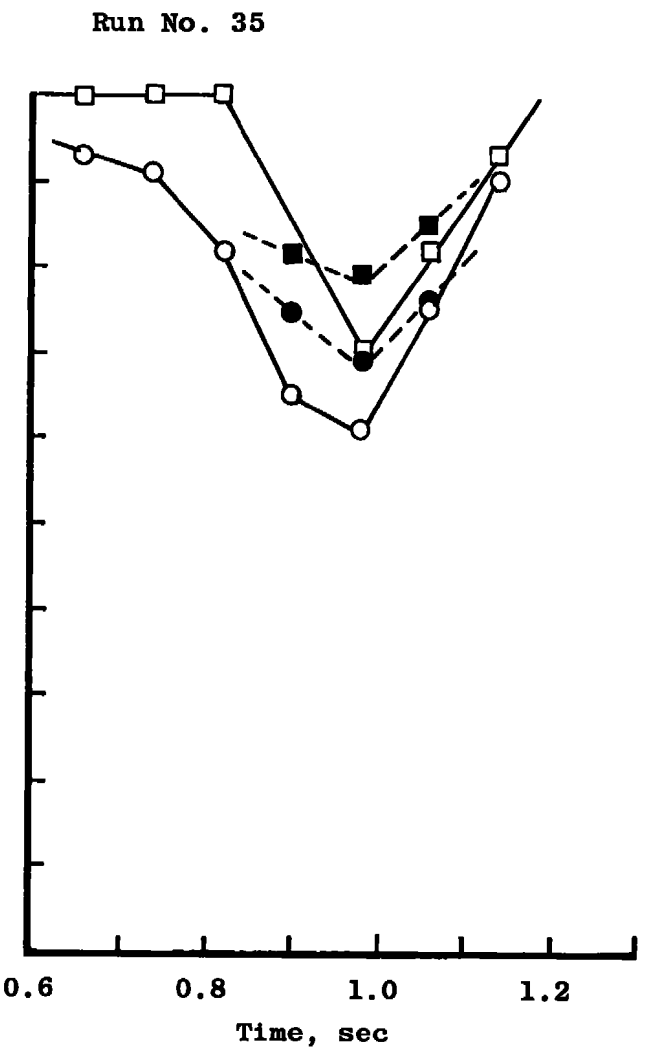
Run No. 35
0.6
0.8
1.0
1.2
Time, sec

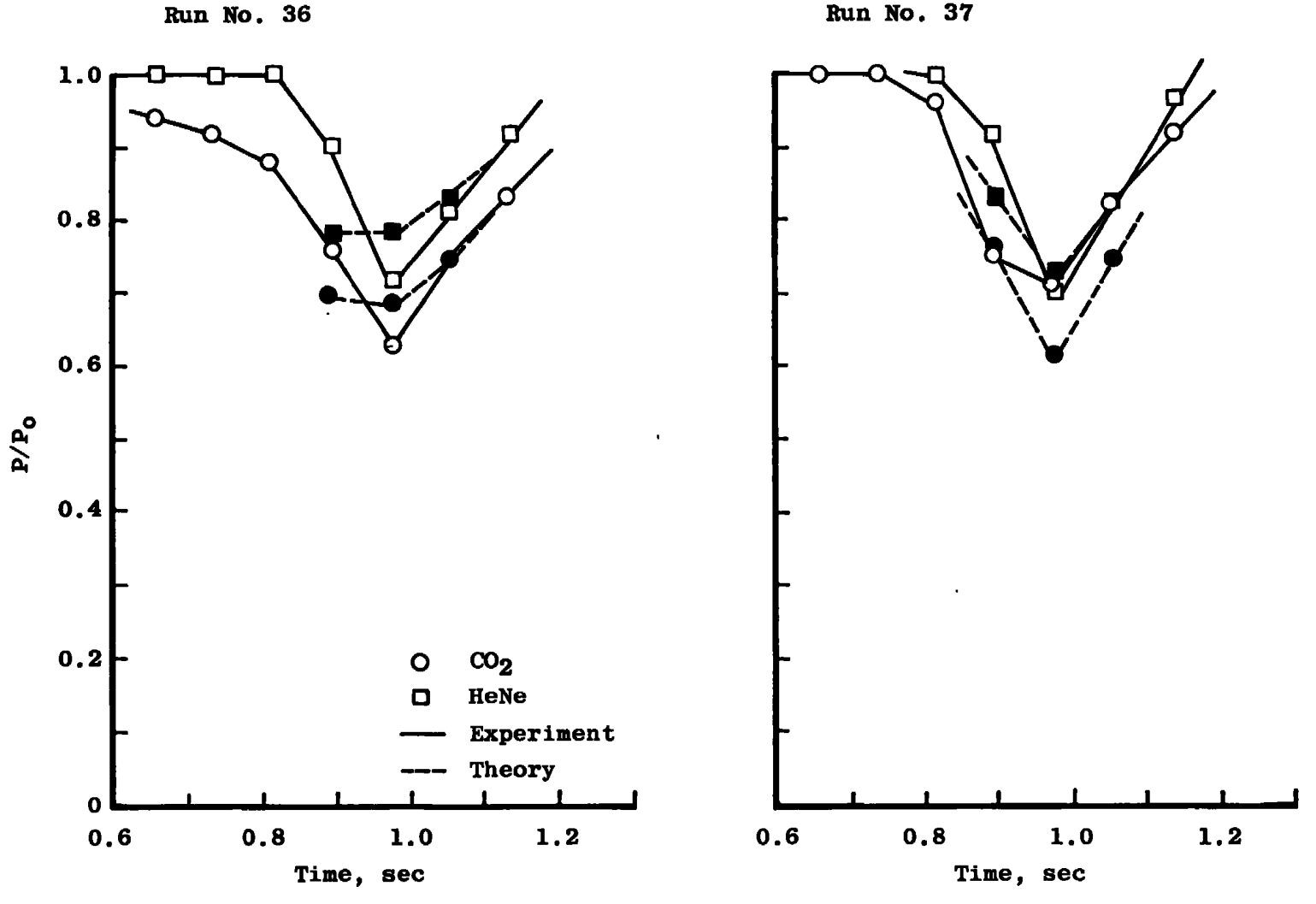
Run No. 36
Run No. 37
1.0
0.8
0.6
0.4
0.2
0
P/P$_o$
0.6
0.8
1.0
1.2
Time, sec
CO$_2$
HeNe
Experiment
Theory

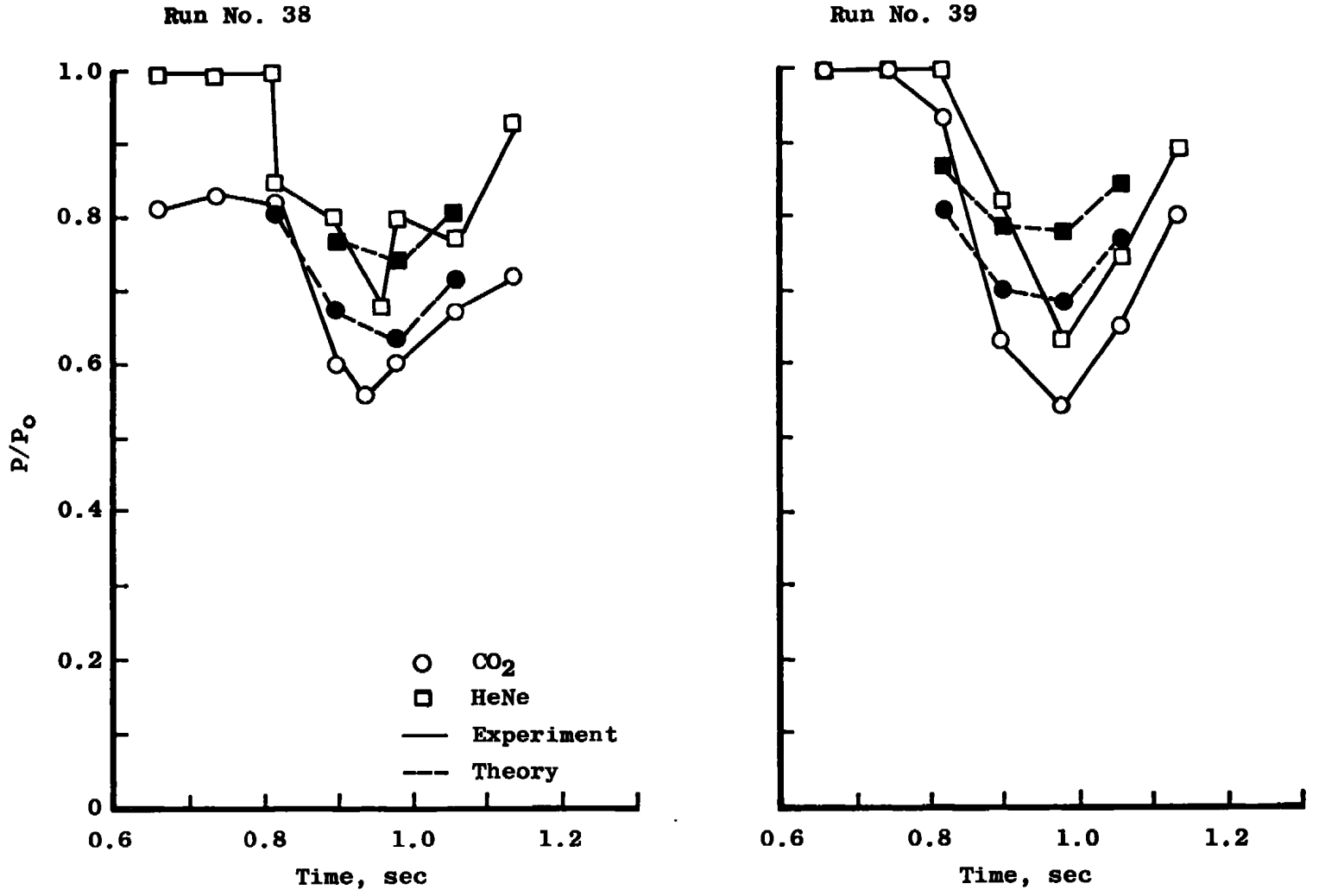
Run No. 38
Run No. 39
1.0
0.8
0.6
0.4
0.2
0
P/P$_o$
0.6
0.8
1.0
1.2
Time, sec
CO$_2$
HeNe
Experiment
Theory

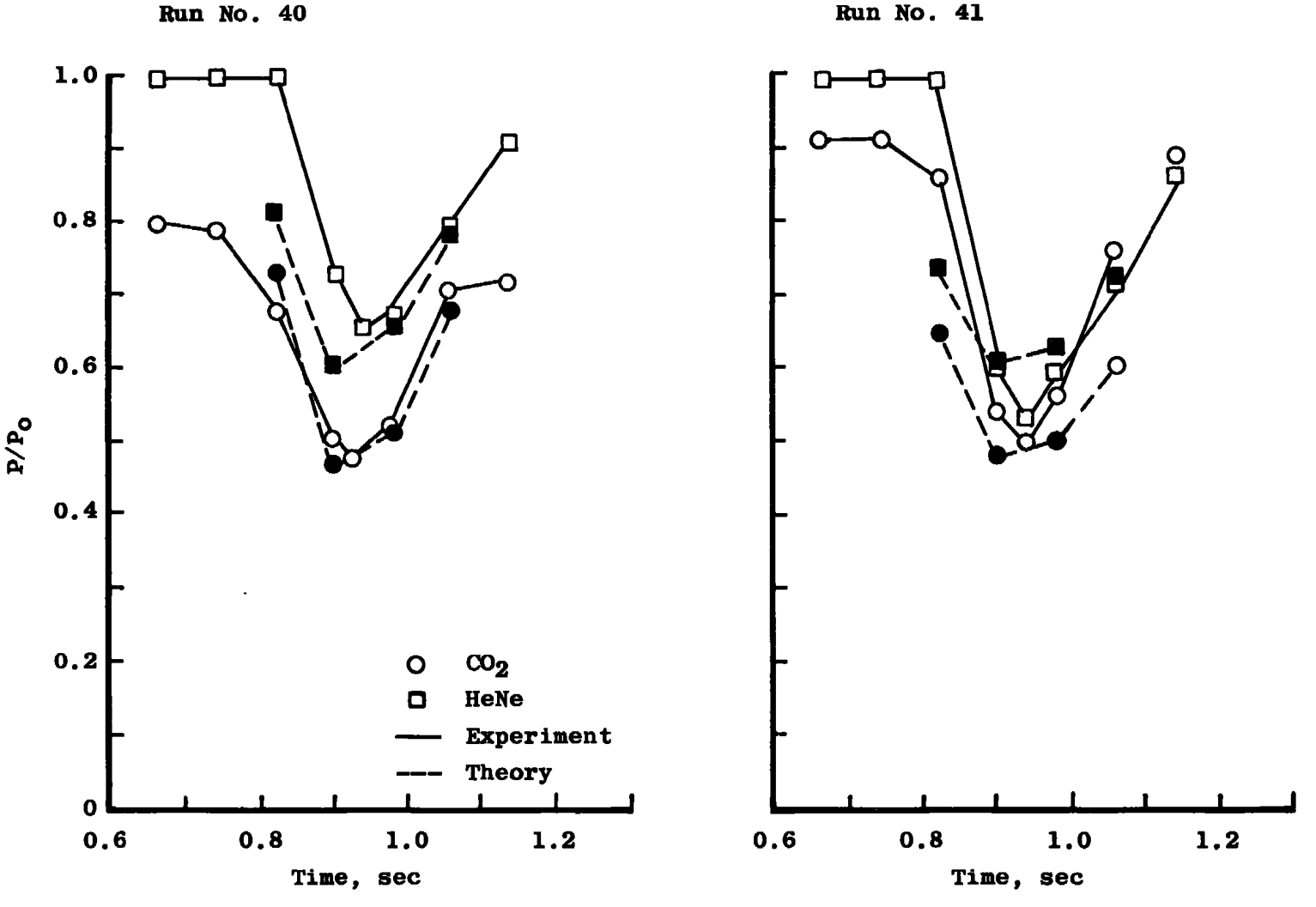
Run No. 40
Run No. 41
1.0
0.8
0.6
0.4
0.2
0
P/P$_o$
0.6
0.8
1.0
1.2
Time, sec
CO$_2$
HeNe
Experiment
Theory

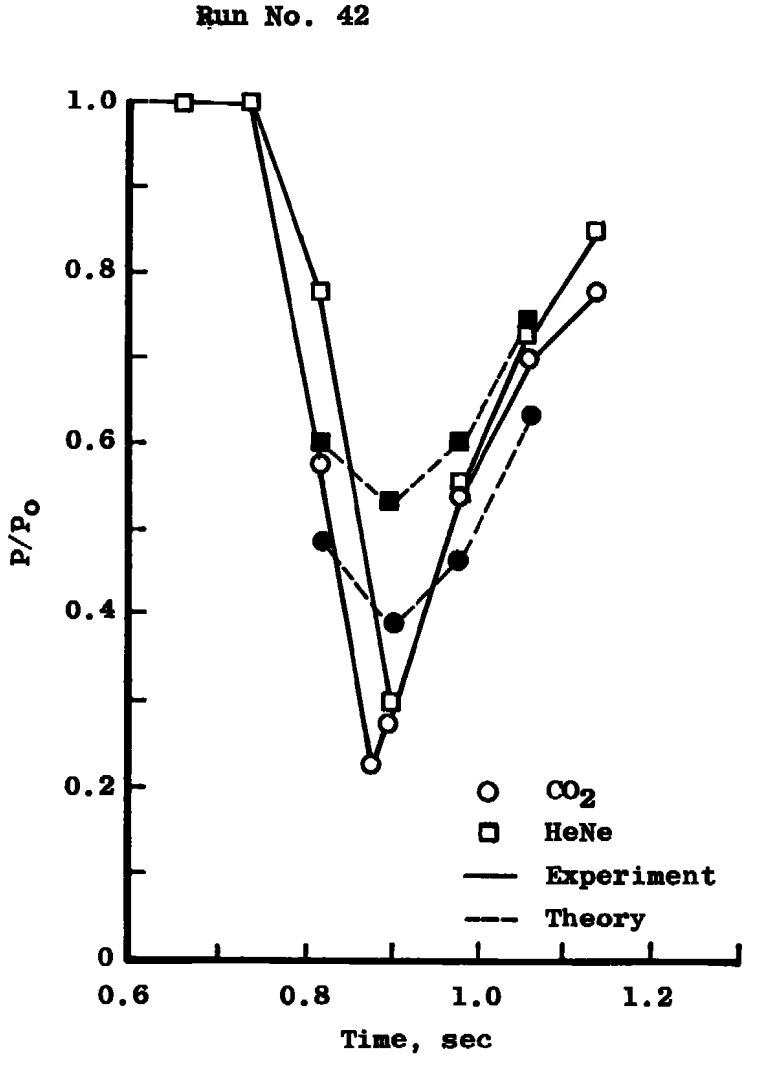
Run No. 42
1.0
0.8
0.6
0.4
0.2
0
P/P$_o$
0.6
0.8
1.0
1.2
Time, sec
CO$_2$
HeNe
Experiment
Theory

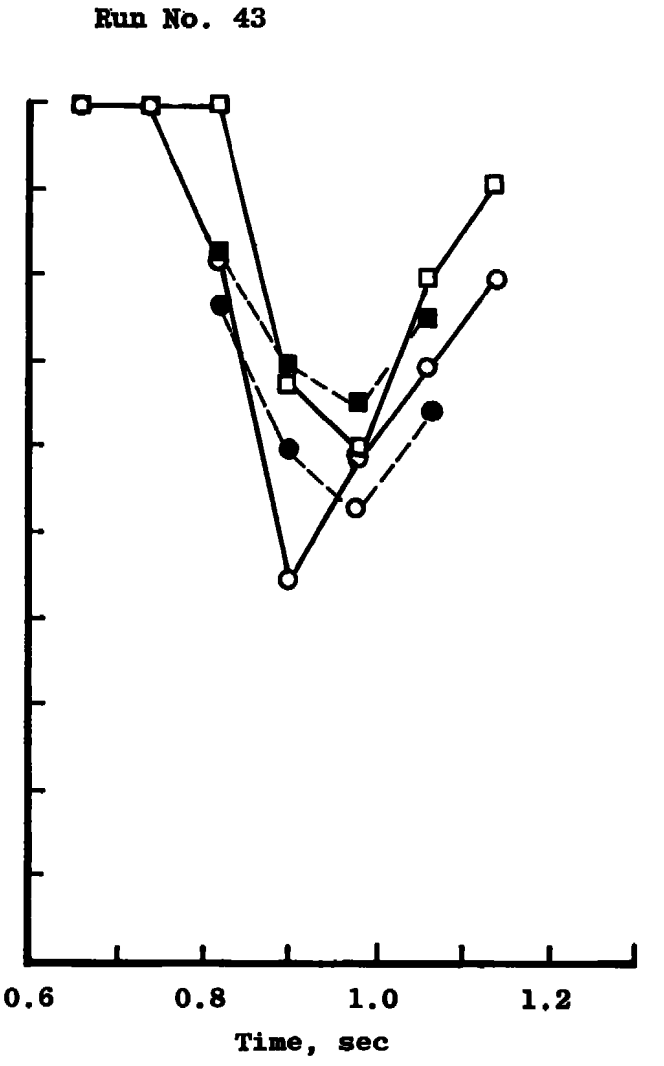
Run No. 43
0.6
0.8
1.0
1.2
Time, sec

NOMENCLATURE

A	Area
A_d	Area of detector
A_e	Effective area of extinction due to particles
$A_{e,i}$	Effective extinction area of a single i^{th} size particle
$A_{I_o,K}$	Area which receives radiation intensity I_o after attenuation by K cells
A_j	Total extinction area of the j^{th} cell
A_L	Cross-sectional area of laser beam
A_s	Effective scattering area of particle
D_d	Detector diameter
D_i	Equivalent melted diameter, mm
D_L	Diameter of laser beam at snowfield
D_o	Equivalent melted value
D_p	Particle diameter
$\Delta D_{p,i}$	Particle size range increment
D_s	Effective scattering diameter = $\sqrt{2 \times D_p}$
I	Intensity of radiation
I_o	Intensity of incident radiation on particle
I_s	Scattered radiation intensity
k	$2\pi\ell/\lambda$
L_c	Dimension of cell in direction along laser beam
L_T	Total extent of snowfield
ℓ	Distance from scattering particle to detector

m	Liquid water content of cloud, g/m^3
N_i	Total number of particles in the i^{th} size range per unit volume per unit size range, $1/m^3$-mm
$N_{L,i}$	Number of particles in the i^{th} size range encountered by laser beam in a particular cell
$N_{SV,i}$	Number of particles in side view of cell in the i^{th} size range
P	Power incident on detector or target
P_o	Initial power in laser beam
r	Radial coordinate of point on detector
S	Distance into cloud, ft
W	Dimension of cell used for snowfield calibration
X	$\pi D_p/\lambda$
a	Constant = 3.67
θ	Scattering angle
θ_{max}	Angular extent of detector
λ	Wavelength
ρ	Density of water (taken to be $1 g/cm^3$)
ϕ	Angular coordinate of point on detector